2017-04-19

Mechanisms to Photoactivate Fluorescence and Strategies for Supramolecular Delivery in Bioimaging Applications

Ek Raj Thapaliya
University of Miami, ekrajthapaliya@gmail.com

UNIVERSITY OF MIAMI

MECHANISMS TO PHOTOACTIVATE FLUORESCENCE AND STRATEGIES FOR SUPRAMOLECULAR DELIVERY IN BIOIMAGING APPLICATIONS

By

Ek Raj Thapaliya

A DISSERTATION

Submitted to the Faculty

of the University of Miami

in partial fulfillment of the requirements for

the degree of Doctor of Philosophy

Coral Gables, Florida

May 2017

UNIVERSITY OF MIAMI

A dissertation submitted in partial fulfillment of
the requirements for the degree of
Doctor of Philosophy

MECHANISMS TO PHOTOACTIVATE FLUORESCENCE AND STRATEGIES FOR SUPRAMOLECULAR DELIVERY IN BIOIMAGING APPLICATIONS

Ek Raj Thapaliya

Approved:

_____ Françisco M. Raymo, Ph.D. Professor of Chemistry	_____ Burjor Captain, Ph.D. Professor of Chemistry
_____ James N. Wilson, Ph.D. Professor of Chemistry	_____ Guillermo Prado, Ph.D. Dean of the Graduate School
_____ Kevin M. Collins, Ph.D. Professor of Biology	

THAPALIYA, EK RAJ (Ph.D., Chemistry)

Mechanisms to Photoactivate Fluorescence and Strategies for Supramolecular Delivery in Bioimaging Applications (May 2017)

Abstract of a dissertation at the University of Miami.

Dissertation supervised by Professor Françisco M. Raymo.

No. of pages in text. (175)

Fluorescence microscopy in combination with photoactivatable fluorophores offers the opportunity to image noninvasively the biological samples in real time with subdiffraction resolution. Photoactivatable fluorophores switch from nonemissive state to emissive state upon irradiation with activation wavelength (λ_{Ac}) and then emit light after excitation of product at suitable excitation wavelength (λ_{Ex}). The concatenation of a photochemical reaction (activation) with a photophysical process (fluorescence) is therefore responsible for the operating principles of these photoresponsive compounds to switch fluorescence on within a defined region of space at a particular interval of time. In turn, such a spatiotemporal control permits the monitoring of dynamic events in real time and the visualization of samples with subdiffraction resolution. The identification of viable operating principles to photoactivate the fluorescence of organic chromophores is, therefore, essential for the further development of these promising imaging techniques. In this context, we designed two mechanisms for the activation of the fluorescence of anthracene derivatives based on photoinduced retro-cycloadditions and photodecarbonylation. Furthermore, mechanism to photoactivate fluorescence by photodecarbonylation was designed to proceed by autocatalytic photochemical pathway where the photoproduct can sensitize its own formation from the reactant, under illumination at a wavelength capable of exciting both species.

The amphiphilic polymer can encapsulate diversity of hydrophobic guest into their hydrophobic core and transport them into the aqueous phase, thus, can be a valuable delivery vehicle for diversity of biomedical applications. These supramolecular nanocarriers along with covalent integration of fluorophores in their molecular backbone can be useful to probe them directly into the intracellular space. In this context, we synthesized amphiphilic polymer by covalent integration of either donor or acceptor in their macromolecular backbone. Their photophysical properties both in organic and aqueous phase along with imaging experiment in Hela cells were performed. We further. optimized the brightness of these polymer by keeping compact dimension, with systematic integration of number of fluorophores in their macromolecular backbone, as a result, these polymers are significant brighter than the model monomers. Such a high brightness level is maintained even after injection of the macromolecular probes in living nematodes, allowing their visualization with a significant improvement in signal-to-noise ratio, relative to the model monomer, and no cytotoxic or behavioral effects. Further, the bioconjugate of this polymer with secondary antibody does not hinder the targeting ability of the former and also can be exploited to stain the tubulin structures of model cells to enable their visualization with optimal signal-to-noise ratios.

We envisaged the protocol to imprint fluorescent pattern on photoresponsive polymer film with mild illumination condition to overcome limitation imposed by conventional photobleaching method. We investigated the photophysical and photochemical properties of this polymer in organic solvent along with fabrication of microscaled fluorescent patterns in polymer film.

To my family and friends

Acknowledgements

First of all, I would like to express my deepest gratitude to my research advisor, Professor Françisco M. Raymo, for his support, guidance and inspiration throughout my graduate studies. His excellent guidance and support inspired me to be a good researcher.

I would like to specially thank Dr. Captain for his enormous work on crystallographic data collection and analysis. My special thanks go to the members of my committee Dr. Burjor Captain, Dr. James N. Wilson and Dr. Kevin M. Collins for their valuable time, efforts and excellent suggestions to my Ph.D. dissertation and defense.

I would like to thank our collaborators Dr. Burjor Captain, Dr. John Callan and Dr. Kevin M. Collins for single crystal X- ray crystallography, fluorescence imaging and live animal imaging respectively.

I would also like to extend my gratitude to my friends and colleagues Dr. Janet Cusido, Dr. Jaume Garcia Amoros, Dr. Subramani Swaminathan, Yang Zhang, Sicheng Tang, Lorenzo Sansalone, Xiaoming Lu, Shuai Fang and Pravat Dhakal for all their help and cooperation. Special appreciation goes to Department of Chemistry for the financial support during my graduate study. Also, I would like to thank all the faculty and staff of the Department of Chemistry for their valuable support.

I would like to thank my lovely wife Janu, beloved brother Tilak and my parents for their support, encouragement and understanding. My life has been bombarded with lot of happiness after the arrival of my two lovely children whose smile bring me a lot of motivation.

TABLE OF CONTENTS

Page

List of Figures

List of Tables

CHAPTER 1

PHOTOACTIVATABLE FLUOROPHORE

1.1. Introduction

Certain organic molecules absorb electromagnetic radiation and thus, undergo electronic excitation from their ground state to their excited state, which can then release energy radiatively. This well-known phenomenon is called photoluminescence. However, the photoluminescence depends on the nature of excited states. If the emission of light occurs from a singlet excited state, in which the excited electrons retains its original spin, the phenomenon is termed fluorescence. While in phosphorescence, the light is emitted from a triplet excited state, in which the excited electron inverts its spin. Generally, fluorescence occurs in the nanosecond timescale and is much faster than phosphorescence, which occurs in the range of microseconds to seconds. These processes can be well illustrated with the so-called Jablonski diagram, developed by Alexander Jablonski

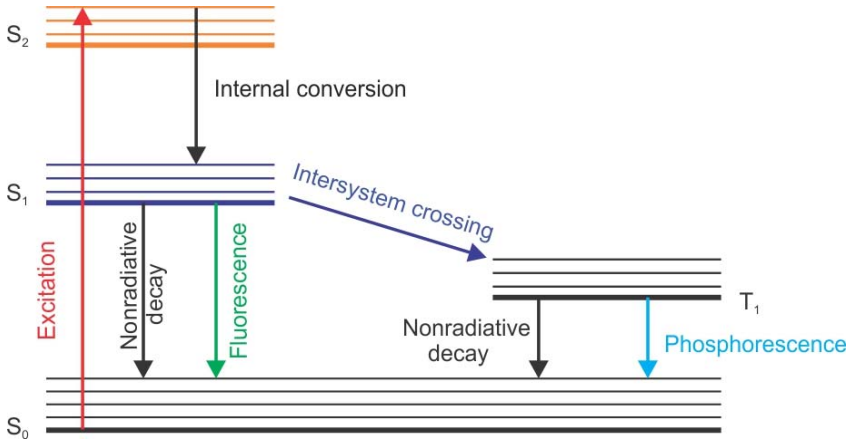

Figure 1.1 Jablonski diagram illustrating excitation of a fluorescent molecule from the ground state (S_0) to the second singlet excited state (S_2) is followed by internal conversion to the first singlet excited state (S_1). The molecule in S_1 can either decay nonradiatively or emit light in the form of fluorescence to regenerate S_0. Alternatively, it can undergo intersystem crossing to populate the first triplet excited state (T_1) and then either decay nonradiatively or emit light in the form of phosphorescence to regenerate S_0.

Fluorescent molecules, after illumination, undergo electronic transitions from their ground state S_0 to a higher order excited singlet state (S_n) from where they relax thermally to lower singlet excited states down to the S_1 state. This process is called internal conversion. Molecules in the S_1 state relax either radiatively, a process called fluorescence, or nonradiatively to the ground state S_0. Energy emitted during fluorescence is always less than that of the absorption process. Consequently, the wavelength of the emission maximum is typically longer than that of the absorption maximum. This difference in wavelength is termed "Stokes' shift", after Sir. G. G. Stokes who discovered this process in 1852. Alternatively, molecules in the S_1 state can also undergo intersystem crossing to populate the first triplet excited state (T_1) and then either decay nonradiatively or emit light in the form of phosphorescence to regenerate S_0. However, molecules in the triplet state exhibit high degree of chemical reactivity because of their longer lifetime compare to singlet, as a result molecules undergo chemical reactions, such as photobleaching and generation of free radicals. Thus, among these relaxation pathways available to deactivate S_1, only one of them is responsible for fluorescence. The quantum efficiency of fluorescence obviously depends on the rate of these competitive pathways. In particular, the fluorescence quantum yield (ϕ_F) is the ratio between the number of photons emitted (N_E) and the number of photons absorbed (N_A) and is related to the rate constants of fluorescence (k_F), nonradiative decay (k_{NR}), intersystem crossing (k_{ISC}) and photochemical conversion (k_{pc}), according to equation (1.1).

$$\phi_F = \frac{N_E}{N_A} = \frac{k_F}{k_F + k_{NR} + k_{ISC} + k_{PC}} \qquad (1.1)$$

Fluorescence measurements[1] became invaluable tools to detect cells in biological fluids and the visualization of tissues in living organisms. Fast response, inherent sensitivity and noninvasive character are the main reasons behind their widespread application in cytometry and imaging. Indeed, labeling strategies to introduce fluorescent probes within biological samples, in combination with microscopic techniques to excite the labels and collect their fluorescence, permit the noninvasive visualization of a diversity of specimens in real time.

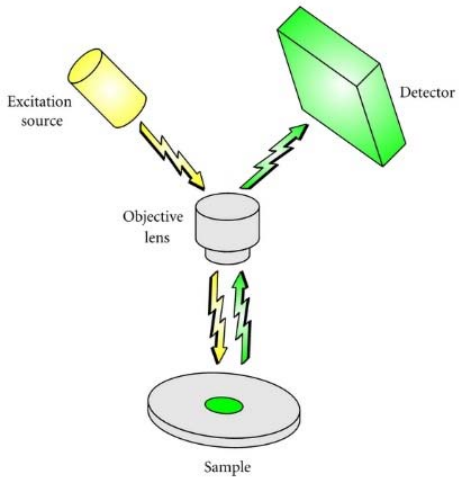

Figure 1.2 The fluorescence microscope records images of samples labelled with fluorescent molecules by exciting the labels and collecting their emissions.

In particular, the basic operating principles of a fluorescence microscope (Figure 1.2) involve the illumination of the labeled specimen with an excitation source through an objective lens.[2] The radiations focused on the sample excite the many fluorescent labels from their ground state (Figure 1.1) to one of their excited singlet states. The excited species relax thermally to the first singlet excited state (S_1) and then radiatively to S_0. The emitted light is collected on the detector, through the very same objective lens, to reconstruct an image of the labeled sample with micrometer resolution on a millisecond

timescale. Under these conditions, the brightness of the fluorophore ultimately dictates the intensity of the detected signal and resolution of images. This particular photophysical parameter is equal to the product of the molar absorption coefficient (ε) of the fluorophore at the excitation wavelength and its fluorescence quantum yield (ϕ). Although, some natural biomolecules like tryptophan, NADH, green fluorescent protein (GFP) are present in biological system as an intrinsic fluorophore, many synthetic fluorophores have been developed which significantly increase the sensitive visualization and wide spread use in diversity of biological media. Out of thousands of fluorophores developed so far, only a few families of them have been used in bioimaging applications such as coumarin, BODIPY, anthracene, rhodamine, fluorescein and cyanine dyes whose basic structures are providing in figure 1.3.[3,4]

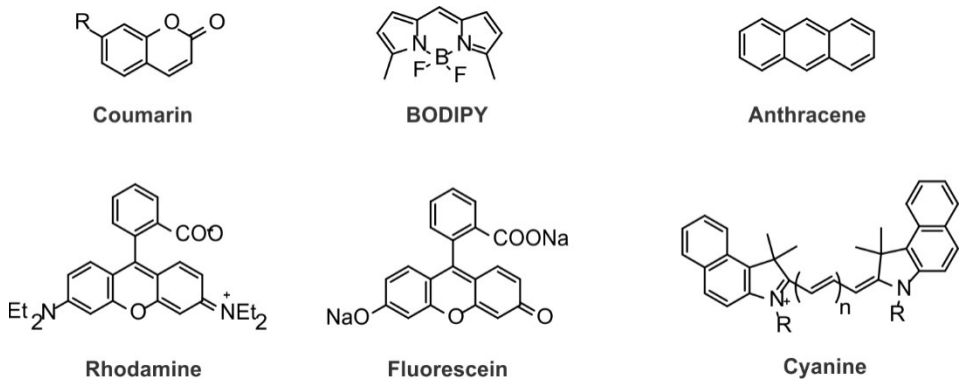

Figure 1.3 Basic structures of some fluorophores for bioimaging applications

However, the fluorescence emitted by a fluorophore is diffracted in the form of an Airy pattern (Figure 1.4) on the focal plane of ther objective lens. Around 84 % of the focused radiation concentrate on the central disk of Airy pattern, whose radius (r) is related to the wavelength (λ) of the emitted light, the refractive index (n) of the medium interposed between lens and its focal plane, as well as the semiaperture angle (θ) of the lens, according

to eq 1.2. This suggests that a fluorescent molecule, emitting visible radiation in air, generates an Airy pattern of hundreds of nanometers in lateral dimensions. As a result, two fluorophores can only be resolved if their distance is greater than the diffraction limit. Thus, the fluorescence microscope cannot acquire images with spatial resolution beyond the diffraction limit relying on conventional fluorophores.

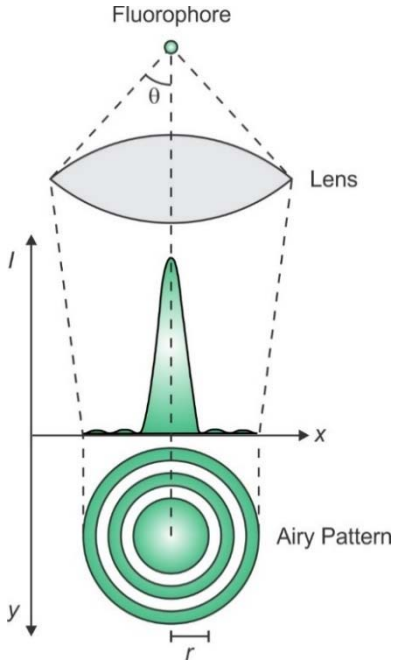

Figure 1.4 The objective lens of a fluorescence microscope projects the light emitted by a fluorophore on the focal plane in the form of an Airy pattern with most of the focused light concentrated in the central disk.

$$r = \frac{0.61\,\lambda}{\mathrm{n}\sin\theta} \qquad (1.2)$$

Fluorophores positioned within the same diffraction volume can be separated temporally if their emissions are designed to turn on at different intervals of time. Organic fluorophore can be designed to switch from a nonemissive state to an emissive one (Figure 1.5) under optical control with the aid of chemical synthesis. Such a photoresponsive system is referred as photoactivatable fluorophore. They are initially in their nonemissive state and, after illumination with activation wavelength, switch to an emissive state, which after

illumination with excitation light produces fluorescence (Figure 1.5) In turn, the interplay of activation and excitation light translates into a spatiotemporal control of fluorescence that is otherwise impossible with conventional fluorophores. Specifically, closely-spaced photoactivatable fluorophores can be resolved in time by activating sequentially their emission. In particular, multiple iterations of illumination steps at λ_{Ac} and λ_{Ex} permit the stochastic activation of distinct subpopulations of probes at different intervals of time and the localization of the activated emitters at the single-molecule level respectively. The spatial coordinates of the probes localized sequentially can then be compiled into a single map to reconstruct an image of the sample with spatial resolution that is no longer controlled by diffraction. In fact, the lateral resolution (Δx) of the resulting image is mostly controlled by the number (N) of emitted photons collected per probe and the background noise (b), according to equation (1.3), together with the pixel size (a) and the standard deviation (s) of the point-spread function.[5] In turn, N is related to the ability of the activated probes to absorb the exciting radiations and emit as a result (brightness), while b is mostly a consequence of the ratio (contrast) between the emission intensity of the emissive state that of the nonemissive one. It follows that probes with large brightness and contrast offer the opportunity to bring Δx down to the nanoscale.

$$\Delta x = \sqrt{\frac{s^2}{N} + \frac{a^2}{12N} + \frac{4\sqrt{\pi\, s^3\, b^2}}{a\, N^2}} \qquad (1.3)$$

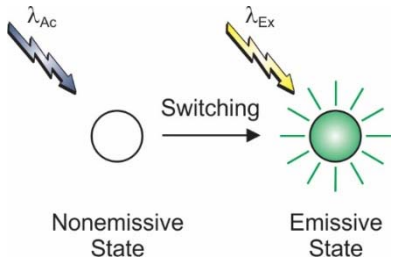

Figure 1.5 Photoactivatable fluorophores switch from a nonemissive to an emissive state upon illumination at an activating wavelength (λ_{Ac}) and then emit light in the form of fluorescence under irradiation at an exciting wavelength (λ_{Ex}).

The imaging strategies possible on the basis of fluorescence photoactivation can be implemented with appropriate fluorescent proteins[6-16] or specific synthetic dyes.[17-21] Both can be engineered to switch either irreversibly or reversibly between distinct states in response to λ_{Ac} and then emit light upon illumination at λ_{Ex}. The physical dimensions of the former probes are significantly larger than those of the latter ones and prevent high labeling densities. Nonetheless, fluorescent proteins can conveniently be introduced into biological samples relying on genetic encoding. Instead, synthetic dyes require labeling protocols based on tedious covalent modifications, often in combination with supramolecular association, but can be introduced in a diversity of materials other than biological preparations. In fact, both families of photoactivatable probes are very much complementary and the choice of one versus the other is generally dictated by the nature of the sample under investigation. A significant advantage of synthetic probes over their biomolecular counterparts, however, lies in the power of chemical synthesis to deliver molecules with engineered properties. Subtle structural manipulations can be invoked to tailor their dimensions, polarity, shapes and spectroscopic response. Thus, synthetic fluorophores with better photochemical and photophysical properties than natural ones can, in principle, be accessed with appropriate synthetic strategies.

1.2. Photoactivation mechanisms

The electronic transition responsible for the fluorescence of most organic chromophores originates from the first singlet excited state (S_1) to produce the corresponding singlet ground state (S_0).[1] This radiative photophysical process can be suppressed either by preventing the population of S_1 altogether or by promoting competitive nonradiative pathways. In fact, the nonemissive state of a photoactivatable fluorophore can be designed around either one of these two strategies. In the first instance, the switching process responsible for activation must be engineered to enable excitation (***a*** in Figure 1.6). Specifically, the molar extinction coefficient at λ_{Ex} must be negligible before switching and become significant only after the photochemical transformation. This requirement is generally satisfied by imposing a decrease on the energy gap between S_1 and S_0 with switching. Under these conditions, the $S_0 \rightarrow S_1$ absorption shifts bathochromically with switching and an appropriate λ_{Ex} can be selected to excite exclusively the photochemical product with concomitant emission. In the second instance, the switching process responsible for activation must be designed to suppress the nonradiative deactivation of S_1 in favor of its radiative decay to S_0 (***b*** in Figure 1.6). In particular, the fluorescence quantum yield must be negligible before switching and become significant only after the photochemical transformation. This requirement is generally satisfied by ensuring the physical separation of a quencher from the emissive chromophore with switching. Under these conditions, the quenching pathway responsible for the nonradiative deactivation of S_1 is prevented with concomitant emission. Thus, both switching mechanisms eventually translate into fluorescence activation. Indeed, they have both been adapted successfully to activate the emission of several members of many families of synthetic dyes, including

borondipyrromethenes,[22,23] coumarins,[24-35] diarylethenes,[36-38] dihydrofurans,[39-42] fluoresceins,[43-50] rhodamines,[51-60] spiropyrans[61,62] and anthracenes.[63-67]

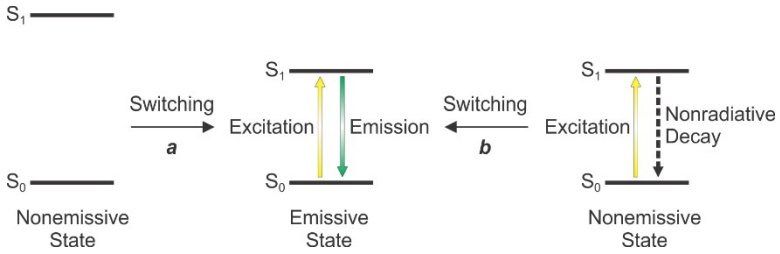

Figure 1.6 The transformation responsible for switching the nonemissive form of a photoactivatable fluorophore into the emissive one can be designed to (a) narrow the energy gap between the first singlet excited state (S_1) and the singlet ground state (S_0) to permit the exclusive excitation of the product or (b) suppress the nonradiative deactivation of S_1 to allow the radiative generation of S_0.

Compounds **1a** and **2a** (Figure 1.7) are representative examples of photoactivatable fluorophores designed around the two activation mechanisms highlighted in Figure 1.6. The absorption spectrum of **1a** shows a band centered at a wavelength ($^{a}\lambda_{Ab}$ in Table 1.1) of 312 nm in methanol.[59] Upon illumination at a λ_{Ac} positioned within this band, **1a** releases molecular nitrogen to form a carbene intermediate. This reactive species either generates a nonfluorescent product or undergo Wolff rearrangement to form a ketene intermediate, which further dissociates into a fluorescent product **1b** in presence of methanol. After activation, uncaging of the diazoketone group switches **1a** into **1b** and shifts the absorption band of the rhodamine chromophore to a wavelength ($^{b}\lambda_{Ab}$ in Table 1.1) of 559 nm. As a result, irradiation at a λ_{Ex} positioned within the shifted absorption band excites selectively **1b** and produces an emission band at a wavelength (λ_{Em} in Table 1.1) of 579 nm in the corresponding spectrum with an emission quantum yield (ϕ_{Em} in Table 1.1) of 0.37. Thus, the photoinduced decrease in the energy gap separating S_1 and S_0 (***a*** in Fig. 1.6) is responsible for fluorescence activation in this switchable system.

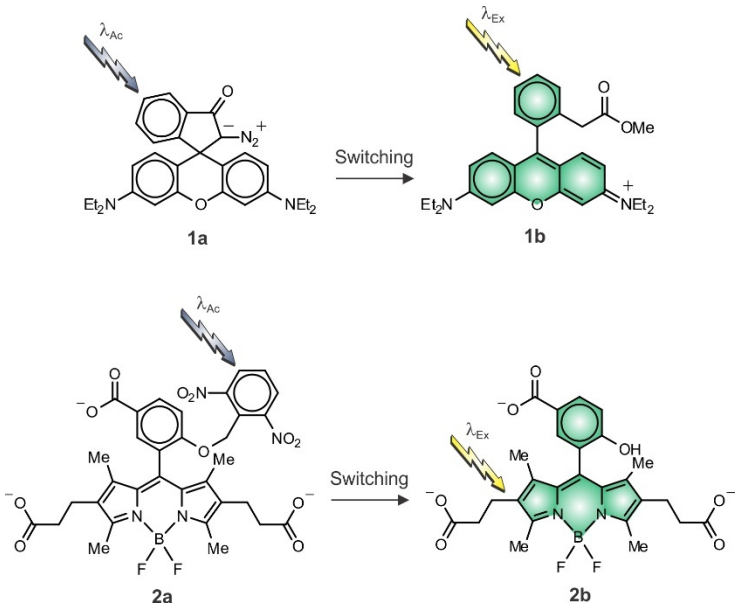

Figure 1.7 The photoinduced transformations of **3a** into **3b** and of **4a** into **4b** shift the corresponding $S_0 \rightarrow S_1$ absorptions bathochromically and permit the selective excitation of the products with concomitant emission. Both switching processes are reversible and the initial nonemissive states are regenerated after photoinduced, in one instance, and thermal, in the other, re-isomerizations.

The three carboxylate groups of **2a** ensure optimal solubility in phosphate buffer saline (PBS).[22] Under these conditions, the absorption spectrum of this compound shows a band at a $^{a}\lambda_{Ab}$ of 526 nm for the borondipyrromethene (BODIPY) chromophore. Excitation at a λ_{Ex} positioned within this band, however, translates into negligible emission. Indeed, the transfer of an electron from the excited BODIPY to the adjacent 2,6-dinitrobenzyl appendage provides an efficient pathway for nonradiative deactivation and suppresses fluorescence effectively. Illumination at a λ_{Ac} of 350 nm cleaves the 2,6-dinitrobenzyl quencher away from the BODIPY chromophore to generate **2b** with a ϕ_{Ac} of 8.9×10^{-3}. This photochemical transformation has negligible influence on the BODIPY absorption, but a dramatic effect on its emissive behavior. Specifically, the absorption band of **2b** is centered at a $^{b}\lambda_{Ab}$ of 522 nm and excitation at a λ_{Ex} positioned within this absorption produces an intense emission band at a λ_{Em} of 539 nm in the corresponding spectrum with

a ϕ_{Em} of *ca.* 0.7. Thus, the photoinduced separation of a quencher from an emissive chromophore prevents the nonradiative deactivation of the latter (***b*** in Figure 1.6) and is responsible for fluorescence activation in this switchable system.

The photochemical reactions responsible for the switching of **1a** to **1b** and of **2a** to **2b** are both irreversible. As a result, the photogenerated states of both systems cannot revert back to the original ones. In fact, the emission of photoactivatable fluorophores, based on irreversible transformations, cannot be switched off, unless the emissive state is permanently bleached. Specifically, prolonged illumination at λ_{Ex} after activation, to promote the degradation of the emissive state, is the only viable mechanism to suppress the fluorescence of these systems. Alternatively, the inherent reversibility of photochromic transformations[68-72] can be exploited to photoactivate fluorescence reversibly. Indeed, one of the two interconvertible states of many photochromic compounds is often fluorescent.[73] Therefore, the photoinduced and reversible conversion of one state into the other translates into fluorescence switching. Nonetheless, the quantum yields of these emissive processes tend to be significantly lower than those associated with the main families of synthetic fluorophores. The diarylethene **3a** (Figure 1.8) is one of the few remarkable exceptions to this general trend.[38] Its absorption spectrum shows a band centered at a $^{a}\lambda_{Ab}$ of 336 nm in 1,4-dioxane. Upon illumination at a λ_{Ac} positioned within this band, **3a** switches to **3b** with a ϕ_{Ac} of 0.42. This structural transformation brings the two halves of the molecule in conjugation and shifts bathochromically the $S_0 \rightarrow S_1$ absorption to a $^{b}\lambda_{Ab}$ of 456 nm. As a result, irradiation at a λ_{Ex} positioned within this band excites **3b** selectively and is accompanied by the appearance of a band a λ_{Em} of 550 nm in the corresponding emission spectrum. Thus, the mechanism responsible for fluorescence activation involves, once

again, a photoinduced decreases in the energy gap between S_1 and S_0 (***a*** in Figure 1.6). Remarkably, ϕ_{Em} approaches a value of 0.9 in this instance and is significantly greater than those of the dihydrofuran **1b** and BODIPY **2b** and (Table 1.1). However, the excitation of **3b** is also accompanied by the photochemical regeneration of **3a** with a quantum efficiency of 4×10^{-4}. Thus, the fluorescence of this particular system can be activated and then deactivated for multiple cycles relying exclusively on optical control.

Photochromic compounds can also be employed in combination with complementary emissive chromophores to photoswitch fluorescence.[74-79] Generally, fluorescent and photochromic components are integrated within the same molecular skeleton or supramolecular construct. The photoinduced and reversible interconversion of the latter can then be employed to control the emission of the former. Specifically, only one of the two interconvertible states of the photochromic component is designed to quench the excited state of the fluorescent component on the basis of electron or energy transfer processes. Under these conditions, the emissive chromophore deactivates nonradiatively, when the switchable component is in the quenching state, and radiatively, in the other instance. These operating principles are reminiscent of the mechanism (***b*** in Figure 1.6) governing the behavior of **2a**, but they are mostly employed to deactivate, rather than activate, fluorescence. Indeed, the initial state of the interconvertible system is generally the emissive one and fluorescence turns off after photoinduced switching.

In alternative to controlling the excitation dynamics of the fluorescent component with the photochromic one, it is also possible to manipulate the absorption properties of the former with the latter. In these systems, the photochromic component is essentially a switchable auxochrome able to regulate reversibly the energy gap between the S_1 and S_0 of the

fluorescent component. For example, compound **4a** (Figure 1.8) joins a coumarin fluorophore to an oxazine photochrome through a vinylene spacer.[30,32] Its absorption spectrum shows a band centered at a $^{a}\lambda_{Ab}$ of 412 nm in acetonitrile for the coumarin component. Irradiation at a $^{a}\lambda_{Ac}$ of 355 nm excites the 4-nitrophenoxy chromophore and results in the opening of the adjacent oxazine ring to form the zwitterionic isomer **4b** with a ϕ_{Ac} of 2×10^{-2}. This structural transformation brings the coumarin appendage in conjugation with the photogenerated 3*H*-indolium cation and shifts its absorption band to a $^{b}\lambda_{Ab}$ of 570 nm. Illumination at a λ_{Ex} positioned within this band excites exclusively the coumarin fluorophore of the photogenerated isomer. In fact, the corresponding emission spectrum shows a band at a λ_{Em} of 650 nm with a ϕ_{Em} of 9×10^{-2}. Thus, the photoinduced control of the $S_0 \rightarrow S_1$ transition (***a*** in Fig 1.6) is, yet again, responsible for activating fluorescence. The photogenerated isomer **4b**, however, reverts spontaneously back to the original species **4a**. This thermal process occurs with first-order kinetics on a microsecond timescale and the lifetime of **4b** is only 0.2 μs. As a result, the fluorescence of this system can be modulated for multiple cycles, on a relatively short timescale, simply by turning on and off a light source operating at λ_{Ac}, while illuminating the sample with another source centered at λ_{Ex}.

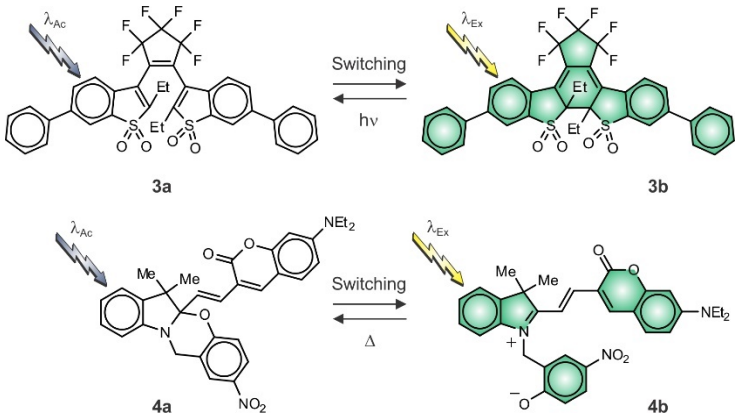

Figure 1.8 The photoinduced transformations of **3a** into **3b** and of **4a** into **4b** shift the corresponding $S_0 \rightarrow S_1$ absorptions bathochromically and permit the selective excitation of the products with concomitant emission. Both switching processes are reversible and the initial nonemissive states are regenerated after photoinduced, in one instance, and thermal, in the other, re-isomerizations.

Table 1.1 Photochemical and photophysical parameters [a] associated with representative examples of photoactivatable fluorophores.

	$^{a}\lambda_{Ab}$ (nm)	$^{a}\varepsilon$ (mM^{-1} cm^{-1})	λ_{Ac} (nm)	ϕ_{Ac} (10^{-3})	$^{b}\lambda_{Ab}$ (nm)	$^{b}\varepsilon$ (mM^{-1} cm^{-1})	λ_{Ex} (nm)	λ_{Em} (nm)	ϕ_{Em} (10^{-2})
1	312	—	360	—	559	66	500	579	39
2	526	—	350	8.9	522	—	—	539	66
3	336	17	313	420	456	46	456	550	87
4	412	36	355	20	570	83	532	650	9

[a] The absorption wavelength ($^{a}\lambda_{Ab}$), molar extinction coefficient ($^{a}\varepsilon$) and activation quantum yield (ϕ_{Ac}) of the nonemissive state as well as the absorption wavelength ($^{b}\lambda_{Ab}$), molar extinction coefficient ($^{b}\varepsilon$), emission wavelength (λ_{Em}) and emission quantum yield (ϕ_{Em}) of the emissive state were measured in MeOH for **1**, PBS for **2**, 1,4-dioxane for **3** and MeCN for **4**.

1.3. Supramolecular amphiphilic nanocarriers

Amphiphilic polymers are valuable macromolecular synthons for the construction of supramolecular hosts capable of capturing a diversity of molecular guests in their interior.[80-89] Their covalent skeleton incorporates hydrophilic and hydrophobic segments that guide the assembly of multiple polymer chains into single particles of nanoscaled dimensions in aqueous environments. Solvophobic interactions bring the hydrophobic fragments of distinct polymer components in contact to minimize their direct exposure to

water. Concomitant solvation of the hydrophilic fragments ensures optimal aqueous solubility and prevents further association of the nanoparticles into micro- and macro-scaled aggregates. The overall result is the spontaneous assembly of nanostructured constructs with hydrophilic surface and hydrophobic interior, where multiple hydrophobic guests can be encapsulated. In fact, such supramolecular hosts can transfer, otherwise insoluble, molecules into aqueous phases and carry them across hydrophilic media. Indeed, self-assembling nanoparticles of amphiphilic polymers are promising supramolecular vehicles for the transport of drugs, photoactivatable fluorophore, fluorescent dyes into specific intracellular targets.[23,90-114] Some of the fundamental aspects of these amphiphilic nanocarrier will be discussed briefly in the following sections.

1.3.1. Synthetic strategies

Free-radical polymerizations are routinely employed to assemble amphiphilic polymers.[115,116] In these processes, a macromolecular backbone forms after the sequential connection of radical building blocks. Such reactive components can be generated through a number of different mechanisms, usually involving the assistance of appropriate initiators. As an illustrative example (Figure 1.9), azobis(*i*-butyronitrile) (AIBN) can be combined with a mixture of hydrophilic **5** and hydrophobic **6** methacrylate monomers.[117] Upon warming the mixture up, AIBN cleaves homolytically to generate a pair of radicals. The resulting species add to the [C=C] bond of either monomer to produce further radicals. The latter add to pristine monomers to initiate the polymer growth until pairs of radicals eventually recombine to terminate the process. The final result is the random assembly of hydrophilic and hydrophobic side chains along a common poly(methacrylate) backbone in the shape of **7**.

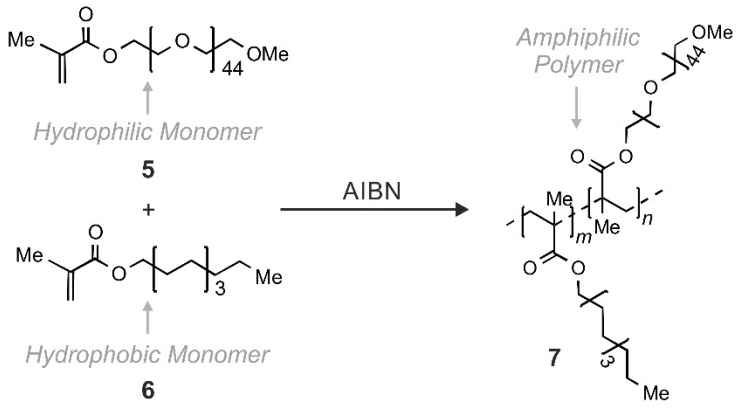

Figure 1.9 Free-radical co-polymerization of monomers **5** and **6**, under the assistance of AIBN, produces amphiphilic polymer **7** with a random distribution of hydrophilic and hydrophobic chains.

1.3.2. Critical micellar concentration

When mixed with water at relatively low concentrations, most amphiphiles migrate to the air/water interface (***a*** in Figure 1.10) to avoid direct exposure of their hydrophobic components to the aqueous environment.[118-120] In the resulting arrangement, the hydrophilic segment of the molecule remains within the aqueous phase, while the hydrophobic counterpart protrudes above the aqueous surface. If the amphiphile concentration is gradually increased, then the air/water interface becomes increasingly crowded until additional molecules are forced to reside within the aqueous phase (***b*** in Figure 1.10). Above a certain concentration threshold, denoted critical micellar concentration (CMC), the amphiphiles in the aqueous phase self-assemble into micellar aggregates (***c*** in Figure 1.10) to prevent the direct exposure of their hydrophobic parts to water. In fact, the hydrophobic portions of the many molecules in each supramolecular assembly point toward the interior of the construct, while the hydrophilic parts are on the surface to be directly exposed to the aqueous solvent. Such an arrangement ensures the most appropriate environment around the hydrophobic and hydrophilic fragments of each molecular component of the self-assembling supramolecular constructs. Any further

addition of amphiphiles slightly beyond the CMC then translates into an increase of the number of micelles dissolved in the aqueous phase. Under these conditions, the many supramolecular assemblies remain isolated from each other with no spatial correlation. At concentrations significantly greater than the CMC, however, liquid-crystalline phases with long-range orientational and positional order may appear.[121-124]

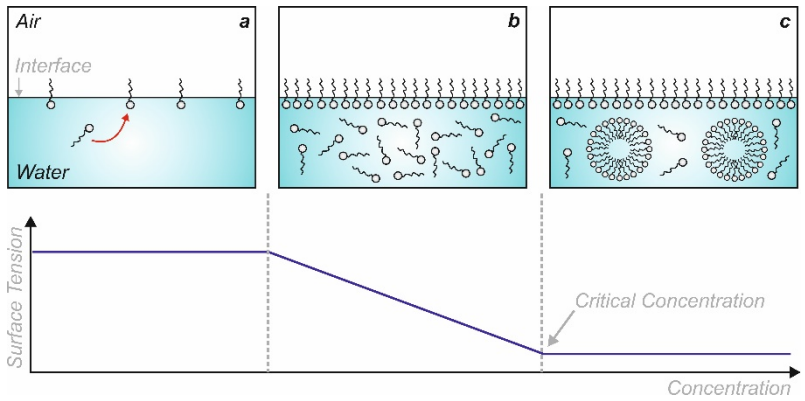

Figure 1.10 The addition of increasing amounts of amphiphilic compounds to water encourages the formation of a layer of molecules at the air/water interface (***a*** and ***b***) and, eventually, results in the self-assembly of micellar aggregates above a critical concentration (***c***).

The morphology of micellar aggregates of amphiphilic components is related to the structural composition and concentration of the individual building blocks and it can vary with the ionic strength and temperature of the solution.[125-129] Generally, these supramolecular assemblies are spherical (Figure 1.11) and, only occasionally, adopt globular or rod-like shapes. In all three instances, the interior of the aggregate is hydrophobic and the surface hydrophilic. However, certain amphiphiles tend to form bilayer assemblies capable of curling into spherical vesicles and encircling solvent molecules within their inner hydrophilic face.

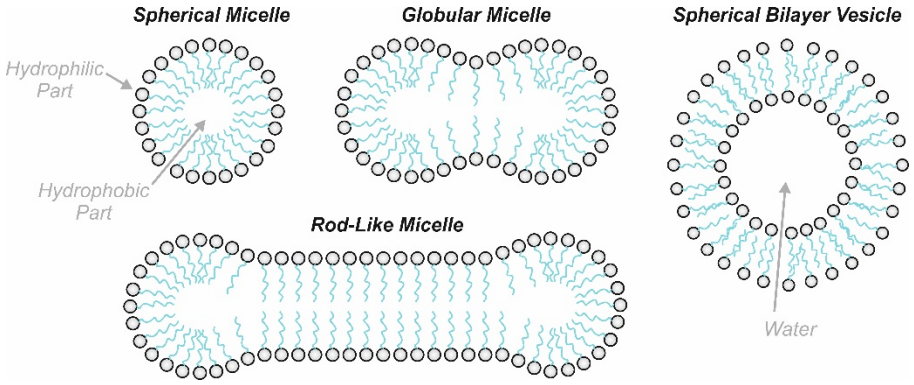

Figure 1.11 Common morphologies of supramolecular assemblies of multiple amphiphilic components.

The value of CMC varies with the structural composition of the self-assembling building blocks and its determination for any amphiphile is essential to identify a range of optimal concentrations to induce the spontaneous formation of micellar aggregates. This crucial parameter can be measured with a diversity experimental procedures based on its influence on certain physical variables, including chemical shift, absorbance, fluorescence intensity, ionic conductivity, osmotic pressure and surface tension.[130-138] Out of these many methods, those relying on fluorescence and surface tension measurements are relatively simple and, as a result, appear to be the most common protocols for CMC determination in literature reports.

Fluorescence methods for CMC determination rely on the ability of the micellar aggregates to encapsulate emissive and hydrophobic probes in their nonpolar interior.[139-142] These molecular guests must be selected to lack any significant solubility in aqueous environments on their own, but readily transfer into an aqueous phase after entrapment within their supramolecular hosts. Under these conditions, their fluorescence can be detected in water only if a given amphiphile is present at a concentration greater than the corresponding CMC. For example, 9,10-bis(diphenylethynyl)anthracene (**8** in Figure 1.12) is essentially insoluble in phosphate buffer saline (PBS), but readily dissolves in the

presence of significant amounts of an amphiphilic polymer (**7**).[111] As a result, the treatment of a fixed amount of **8** with identical volumes of PBS solutions containing increasing concentrations of **7** can be exploited to identify the CC value of the polymer. Indeed, no emission can be detected at low polymer concentrations (Figure 1.12). Once CMC is reached, however, the amphiphiles assemble into micellar aggregates. The resulting supramolecular constructs capture the fluorescent species, transfer them into the aqueous phase and allow the detection of their fluorescence. Consistently, a sudden increase in emission intensity is observed above this particular concentration threshold (Figure 1.12).

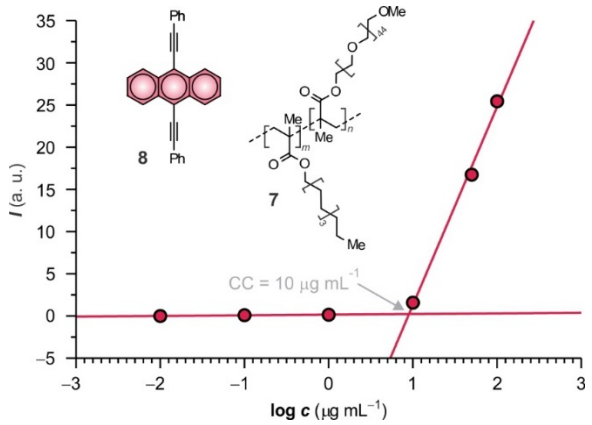

Figure 1.12 Plot of the emission intensity of **8** (1 μg mL^{-1}, λ_{Ex} = 440 nm, λ_{Em} = 476 nm) against the concentration of **7** in PBS at 25 °C.

1.3.3. Hydrodynamic diameter

Dynamic light scattering measurements can provide a quantitative assessment of the size distribution of spherical nanoparticles dispersed in a solvent from the analysis of their random thermal motion (Brownian motion).[143-146] Indeed, the translational diffusion coefficient (D_t) of the moving nanoparticles is inversely related to their hydrodynamic diameter (D_h) according to equation (1.4), where k_B, T and η are Boltzmann's constant, temperature and viscosity respectively. As a result of this correlation, the displacement of

small diffusing nanoparticles over time (***a*** in Figure 1.13) is more pronounced than that of large counterparts (***b*** in Figure 1.13). In fact, the sequential tracking of the nanoparticle positions with very short probing intervals (< 100 μs) permits the determination of their physical dimensions, even when the moving objects are micellar aggregates of amphiphilic building blocks.

$$D_{\mathrm{h}} = \frac{k_{\mathrm{B}}T}{3\pi\eta D_{\mathrm{t}}} \tag{1.4}$$

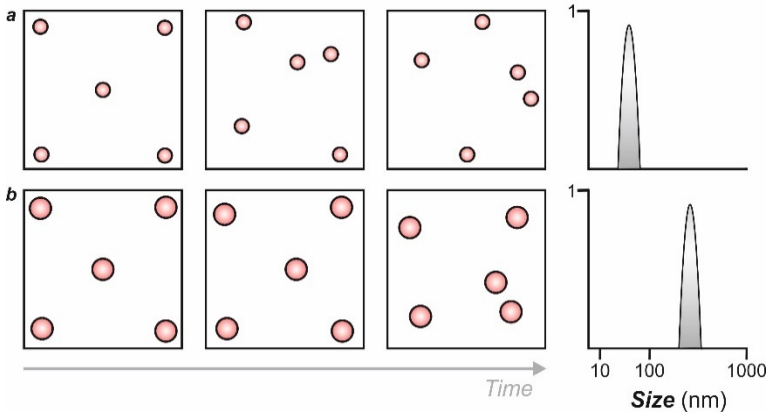

Figure 1.13 Illustration of the relationship between the speed of particle movement and the size.

Experimentally, this particular technique determines the aggregate size by measuring the random changes in the intensity of light scattered from the corresponding solution. Generally, a laser source illuminates the sample maintained in a transparent cell and the scattered light (Figure 1.14) is collected on a photomultiplier tube. As the diffusing aggregates are constantly in motion, the obtained optical signal shows random changes because of the constructive and destructive phase addition of the scattered light with time. Their size can then be extracted from this signal after an appropriate mathematical treatment. Specifically, the detected signal can be interpreted in terms of an autocorrelation

function [$G(\tau)$] of the delay time (τ), *i.e.* the time that elapses between two consecutive data collections. If all the particles are identical in size, [$G(\tau)$] decays monoexponentially with τ, according to equation (1.5), and fitting of the experimental data provides an estimate of the decay constant (Γ). In turn, this parameter is directly related to D_t, according to equation (1.6), where the scattering vector (q) is a function of the refractive index (n) of the liquid, the wavelength (λ) of the laser and the scattering angle (θ), according to equation (1.7). Thus, a measurement of [$G(\tau)$] against τ ultimately provides a value of D_t and, in combination with equation (1.4), also of D_h.

$$G(\tau) = \exp\left(-2\Gamma\tau\right) \tag{1.5}$$

$$\Gamma = D_t q^2 \tag{1.6}$$

$$q = (4\pi n/\lambda)\sin(\theta/2) \tag{1.7}$$

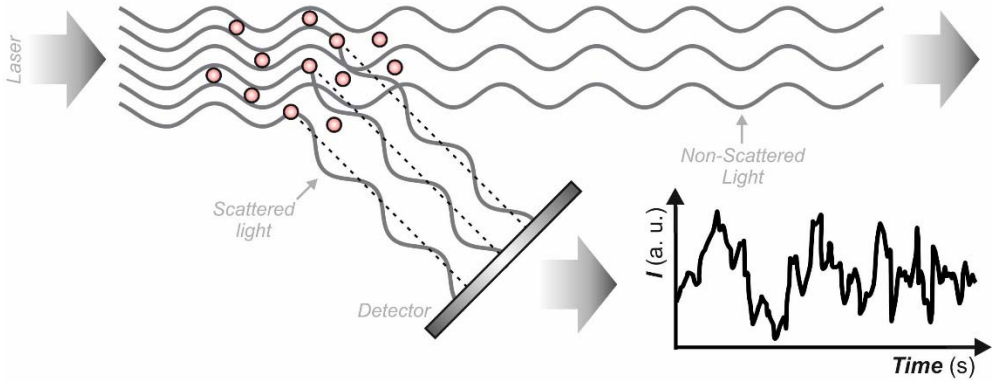

Figure 1.14 Schematic representation of the optical setup used for dynamic light scattering measurements of nanoparticle sizing [adapted from ref.[147]].

Nonetheless, most samples have a distribution of nanoparticle sizes and, therefore, the correlation of [$G(\tau)$] and τ becomes a power series, according to equation (1.8). Once again, a decay constant ($\overline{\Gamma}$), which is the sum of all the individual exponential decays

contained in the correlation function and is proportional to D_t, is extracted to obtain a weighted average of D_h, termed *z*-average size.

$$G(\tau) = \exp\left(-2\bar{\Gamma}\tau + \mu_2 \tau^2 - \cdots\right) \quad (1.8)$$

Besides fitting a single exponential decay to the correlation function (eq. 1.8) to obtain the *z*-average size, a multiexponential function can be used instead to obtain the distribution of particle sizes. After applying such a mathematical algorithm, one gets the size distribution as a plot of the relative intensity of light scattered by the particles in various size classes. As an example (Figure 1.15), shows the intensity distributions for amphiphilic polymers **7** and **9**. Specifically, hydrodynamic diameters of *ca.* 10 and 130 nm are registered for these two particular amphiphilic macromolecules respectively.

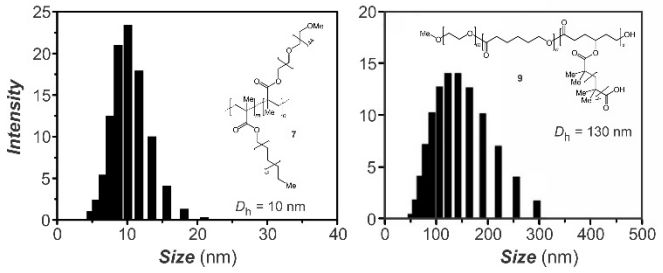

Figure 1.15 Chemical structure and hydrodynamic diameters, D_h, for amphiphilic polymers **7** and **9** [Reprinted with permission from *Polym. Chem.* © 2013, Royal Society of Chemistry].

1.3.4. Intracellular förster resonance energy transfer with assistance of supramolecular nanocarrier

Self-assembling nanoparticles of amphiphilic building blocks are promising vehicles for the delivery fluorescent dyes into the intracellular space for bioimaging applications.[23,111,112,148] The nonpolar environment in their interior can promote the encapsulation of hydrophobic molecules, while the polar groups on their surface ensure

optimal solvation and permit the transport of the entrapped cargo across hydrophilic media. Particularly, the amphiphilic polymer **7** can self-assemble in water to form micelles with hydrodynamic diameter (D_h) of 15 nm that can capture hydrophobic guest and transfer them into aqueous medium. Two complementary chromophore **9** (energy donor) and **10** (energy acceptor) can be encapsulated in a polymer micelle of **7** to solubilize them in aqueous phase, otherwise insoluble, to allow their energy transfer from former to later after excitation of donor. The characteristic emission of the borondipyrromethene (BODIPY) chromophore of **9** extends from 450 nm to 600 nm. The absorption bands associated with the $S_0 \rightarrow S_1$ transitions of the anthracene chromophore of **10** are positioned between 450 and 550 nm. The pronounced spectral overlap corresponds to a J of 9.1×10^{-14} M^{-1} cm^3 and a R_0 of 47 Å. These values ensure the efficient transfer of energy from **9** to **10**, when both species are co-encapsulated within the interior of nanoparticles of **7**. Consistently, the emission spectrum shows predominantly the fluorescence of the acceptor between 540 and 640 nm and its comparison to those of the separate components indicates that energy is transferred with an E of 0.95.

In these FRET experiments, donor, acceptor and amphiphilic polymer are mixed in chloroform and, after the evaporation of the organic solvent, the residue is dispersed in aqueous medium.[111] Under these conditions, the two complementary chromophoric guests are captured within the same supramolecular host and the transfer of energy from one to the other occurs efficiently upon excitation. The very same result, however, is obtained if an aqueous solution of nanoparticles containing exclusively the donors is combined with an aqueous solution of nanocarriers entrapping only the acceptors. Upon mixing, the two sets of supramolecular assemblies exchange their components with relatively fast kinetics

to co-localize donors and acceptors within the same containers. Indeed, the emission spectrum (***a*** in Figure 1.16), recorded immediately after mixing the two solutions, shows predominantly the acceptor fluorescence and scales linearly with a tenfold dilution of the sample with PBS (***b*** in Figure 1.16). These observations demonstrate that FRET occurs after mixing and that the efficiency of the process does not change with dilution. In turn, the latter result indicates that the increase in physical separation between the nanoparticles, occurring with dilution, has no depressive effect on FRET and, therefore, confirms that donors and acceptors are co-entrapped within the same containers. By contrast, a tenfold dilution of the sample with THF disrupts the hydrophobic interactions responsible for the integrity of the nanoparticles to separate donors from acceptors and prevent FRET. As a result, the corresponding emission spectrum (***c*** in Figure 1.16) shows predominantly the donor fluorescence.

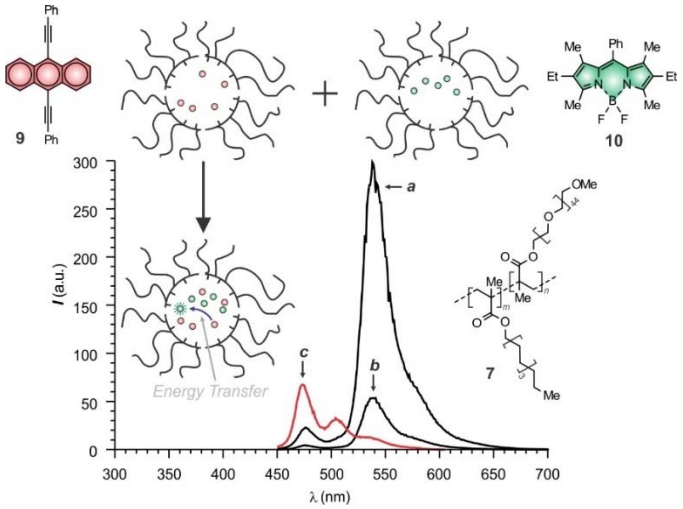

Figure 1.16 Emission spectra (λ_{Ex} = 430 nm) recorded after mixing identical volumes of two PBS dispersions of nanoparticles of **7** (500 μg mL^{-1}), loaded with **9** (5 μg mL^{-1}) or **10** (5 μg mL^{-1}), respectively, before (**a**) and after 10-fold dilution with either PBS (**b**) or THF (**c**).

The intriguing behavior of these dynamic supramolecular systems can be exploited to transport molecules into the intracellular space and, only there, allow their mutual

interaction.[111] Indeed, nanoparticles of **7** can cross the membrane of cervical cancer (HeLa) cells and carry either **9** or **10** along in the process. Fluorescence measurements performed before (***a*** in Figure 1.16) and after (***b*** and ***d*** in Figure 1.17) incubation, however, reveal only negligible intracellular emission. In these experiments, the sample is illuminated at the excitation wavelength of the donor and fluorescence is detected at the emission wavelength the acceptor. Therefore, the presence of only the donor or only the acceptor cannot produce any significant fluorescence, under these excitation and detection conditions. If the cells are incubated sequentially with the two sets of nanoparticles, then intense emission is instead detected under the very same conditions (***c*** in Figure 1.17). These observations demonstrate that the internalized nanoparticles exchange their components with fast kinetics within the intracellular environment to co-localize donors and acceptors in close proximity and enable FRET. Consistently, fluorescence images (***e*** and ***f*** in Figure 1.17) recorded after sequential incubation with nanoparticles containing the donor and then nanocarriers containing the acceptor, or *vice versa*, show clearly intracellular fluorescence.

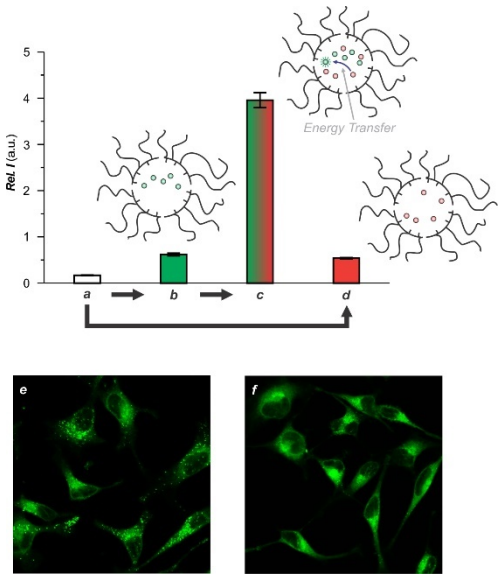

Figure 1.17 Emission intensities (λ_{Ex} = 430 nm, λ_{Em} = 540 nm), reported relative to that of an indocyanine green standard (50 μM, λ_{Ex} = 730 nm, λ_{Em} = 780 nm) added 30 min prior to termination of incubation, recorded with a plate reader before (*a*) and after incubation of HeLa cells with a PBS dispersion of nanoparticles of 7 (125 μg mL^{-1}), containing 10 (1.25 μg mL^{-1}), for 3 h and washing (*b*) and subsequent incubation with a PBS dispersion of nanocarriers of 3 (125 μg mL^{-1}), containing 9 (1.25 μg mL^{-1}), for a further 3 h and washing (*c*) or after incubation with the same dispersion of nanoparticles, containing 1, for 3 h and washing (*d*). Fluorescence images (λ_{Ex} = 458 nm, λ_{Em} = 540−640 nm) of HeLa cells recorded after incubation with a PBS dispersion of nanoparticles of 3 (125 μg mL^{-1}), containing 10 (1.25 μg mL^{-1}), for 3h, washing and subsequent incubation with a PBS dispersion of nanocarriers of 7 (125 μg mL^{-1}), containing 9 (1.25 μg mL^{-1}), and washing (*e*) or after the same treatment but inverting the order of addition of the two components (*f*).

1.4. Conclusions

Photoactivatable fluorophores can be designed to switch from their non-emissive state to an emissive state mostly on two basic mechanisms. In one instances, a photochemical transformation is designed to control the ability of a chromophore to absorb exciting radiations. In the other, the photochemical event facilitates the radiative decay of the excited chromophore. Both result in fluorescence activation after illumination at activating and exciting wavelengths. Such concatenation of activation and excitation events can be exploited to switch probe from off to on in a defined region of space at a given interval of time. Such a spatiotemporal control of fluorescence translates into the opportunity to reconstruct the images of biological samples with subdiffraction resolution. Further,

amphiphilic polymers incorporate hydrophilic and hydrophobic side chain in their macromolecular backbone and spontaneously self-assembled into nanostructured constructs with hydrophobic core and hydrophilic surface in aqueous environment at a concentration greater than CMC. Furthermore, hydrophobic probes can be encapsulated within these nanocarriers to transport them into the intracellular space with preserving the photochemical and photophysical properties of these hydrophobic probes. Thus, these supramolecular nanocarriers in combination with photoactivatable probes becomes invaluable tool for bioimaging applications.

1.5. Scope of thesis

Extensive research has been done to develop a mechanism to photoactivate the fluorescence for bioimaging applications. However, the application of these probe in biological samples may not be ideal because of their limited photophysical and photochemical properties engineered to photoactivate them in vivo. Additionally, most of them are hydrophobic in nature, whose transport into the intracellular space can be accompanying with use of supramolecular amphiphilic nanocarriers. These nanocarrier can not only transport the hydrophobic guest, but also be useful to track them into the intracellular space, especially by covalent integration of fluorophore into the molecular backbone of amphiphilic polymer.

During the course of my graduate studies, I have developed mechanisms to photoactivate the fluorescence of anthracene fluorophores and the strategies to deliver them into the intracellular space with the help of supramolecular fluorescent amphiphilic nanocarriers. In **chapter 2**, I have synthesized photoactivatable anthracene by Diles Alder reaction of anthracene chromophores with maleimide dienophile.[66] The photophysical and

photochemical properties of all adducts were studied in organic solvent. In **chapter 3**, a mechanism was developed to activate fluorescence by autocatalytic photochemical pathway, where product can sensitize its own formation.[67,149] Herein, two adducts were synthesized by introducing diketone group in 9,10 positions of anthracene chromphore, which delocalize the electronic communication between two *ortho* phenylene ring of anthracenes, as result, suppress the fluorescence of these fluorophores. The photophysical and photochemical properties of these probes were investigated both in organic and polymer matrix. In **chapter 4**, supramolecular nanocarriers were designed by covalent integration of either anthracene or BODIPY chromophores in their molecular backbone to probe them intracellularly.[112] The photophysical properties of the synthesized polymers were investigated in both organic and aqueous phase. Furthermore, these nanocarriers were successfully transported into the intracellular space of HeLa cells. In **chapter 5**, these fluorescent amphiphilic polymers were optimized by increasing their brightness with keeping the compact dimensions, which are obviously the important parameters for bioimaging applications. The high brightness of such polymer demonstrated significant improvement in signal to noise ratio, relative to the model monomer, after injecting them into the live nematode. Further, these polymers in conjugation with secondary antibody can be useful to visualize the tubulin structure with optimal signal to noise ratio. In **chapter 6,** photoresponsive polymer was synthesized by covalent integration of oxazine photochrome in the molecular backbone of norbornyl system.[150] These photoresponsive polymer along with fluorescent dyes demonstrated to imprint the fluorescent pattern under mild illumination conditions that are impossible to replicate with methods solely based on bleaching.

CHAPTER 2

PHOTOACTIVATABLE ANTHRACENES

2.1. Background

The photochemical conversion of a nonemissive reactant into an emissive product offers the opportunity to activate fluorescence under the influence of optical stimulations.[17-19,21,151,152] Specifically, a pair of independent irradiation sources, operating at distinct wavelengths, can excite reactant and product respectively to induce the photochemical transformation of the former and the emission of the latter. Under these conditions, the spatial overlap of the two illuminating beams and their temporal interplay permits the activation of fluorescence exclusively within a defined region of space at a given interval of time. In turn, the sequential acquisition of fluorescence images, after a single activation event, enables the monitoring of the translocation of the activated emitters in real time.[20,153-157] Alternatively, the sequential localization of emitters, activated at distinct intervals of time, with single-molecule precision allows the reconstruction of images with spatial resolution at the nanometer level.[158-163] These ingenious imaging schemes provide the possibility to track dynamic events and visualize nanoscaled features respectively in a diversity of specimens and, therefore, are becoming particularly valuable in biological and materials sciences. Nonetheless, their practical implementation is simply impossible with conventional fluorophores and, instead, strictly demands the unique combination of photochemical and photophysical properties associated with their photoactivatable counterparts. Thus, the identification of viable structural designs to photoactivate fluorescence is essential to foster the further development of such promising analytical techniques.

The anthracene skeleton is a convenient building block for the construction of photoactivatable fluorophores. In fact, early examples of fluorescence photoactivation were designed around the structural and spectroscopic properties of this particular chromophore.[164-166] These seminal studies were aimed at the development of photosensitive materials for photographic applications and relied on the introduction of a photocleavable anhydride bridge across positions 9 and 10 of the anthracene platform. This particular bridging unit was designed to isolate electronically the two peripheral phenylene rings of the oligoacene skeleton and suppress its characteristic fluorescence. Upon ultraviolet illumination, the anhydride bridge cleaves into a molecule of carbon dioxide and one of carbon monoxide to restore the aromatic character of the central benzene ring together with the emission of the regenerated anthracene fluorophore. Similarly, two carbon atoms within one of the multiple rings on an oligoacene chromophore can also be connected through an α-diketone bridge to interrupt electronic delocalization across the aromatic platform.[63,64,167-182] This particular functional group cleaves into two molecules of carbon monoxide upon excitation to restore the parent oligoacene and its spectroscopic signature. In fact, these operating principles have also been exploited to activate the fluorescence of a few anthracene derivatives.[63-65]

In alternative to the introduction of photocleavable carbonyl groups, the cycloaddition of appropriate dienophiles to the central ring of anthracene derivatives can also isolate electronically the peripheral phenylene rings with photoresponsive bridges.[183-187] Specifically, a handful of alkenes and a few acylnitroso compounds form photolabile cycloadducts capable of undergoing retro-cycloadditions under illumination to restore the aromatic character of the oligoacene platform. The synthetic accessibility of these

particular cycloadducts, together with the opportunity to regulate the spectroscopic signature of the anthracene chromophore with the manipulation of its substituents, can translate into the realization of versatile photoactivatable fluorophores. Nonetheless, the potential of these photochemical transformations to activate fluorescence remains essentially unexplored. These considerations suggest the possibility of assembling a series of anthracene cycloadducts differing in their substituents with the ultimate goal of identifying an optimal structural design for fluorescence photoactivation. Indeed, this article reports the synthesis of a family of *N*-arylmaleimide cycloadducts, their structural characterization as well as the investigation of their photochemical and photophysical properties.

2.2. Results and discussion

2.2.1. Synthesis and structural characterization

The cycloaddition of maleic anhydride on the central ring of anthracene introduces a bridge between positions 9 and 10 of the oligoacene platform in the shape of cycloadduct **1** (Figure 2.1).[188] This compound is a valuable precursor for the generation of an entire family of anthracene cycloadducts, differing in the nature of the bridging unit. Specifically, treatment of **1** with primary amines **2**–**11**, in the presence of potassium carbonate, produces imides **12**–**21** in yields ranging from 32 to 63%.[187,189]

In addition to varying the group on the maleimide bridge, substituents can be introduced on either the two *ortho*-phenylene rings or positions 9 and 10 of these anthracene cycloadducts. Specifically, the cycloaddition of maleimide **22** (Figure 2.1) on the central ring of substituted anthracenes **23**–**25** generates adducts **26**–**28** in yields ranging from 36 to 55%. Alternatively, reaction of maleic anhydride (**29** in Figure 2.1) with substituted

anthracenes **30** and **31** produces anhydrides **32** and **33** respectively.[187,189] Treatment of these compounds with **6**, in the presence of potassium carbonate, produces **34** and **35** in yields of 55 and 45% respectively.

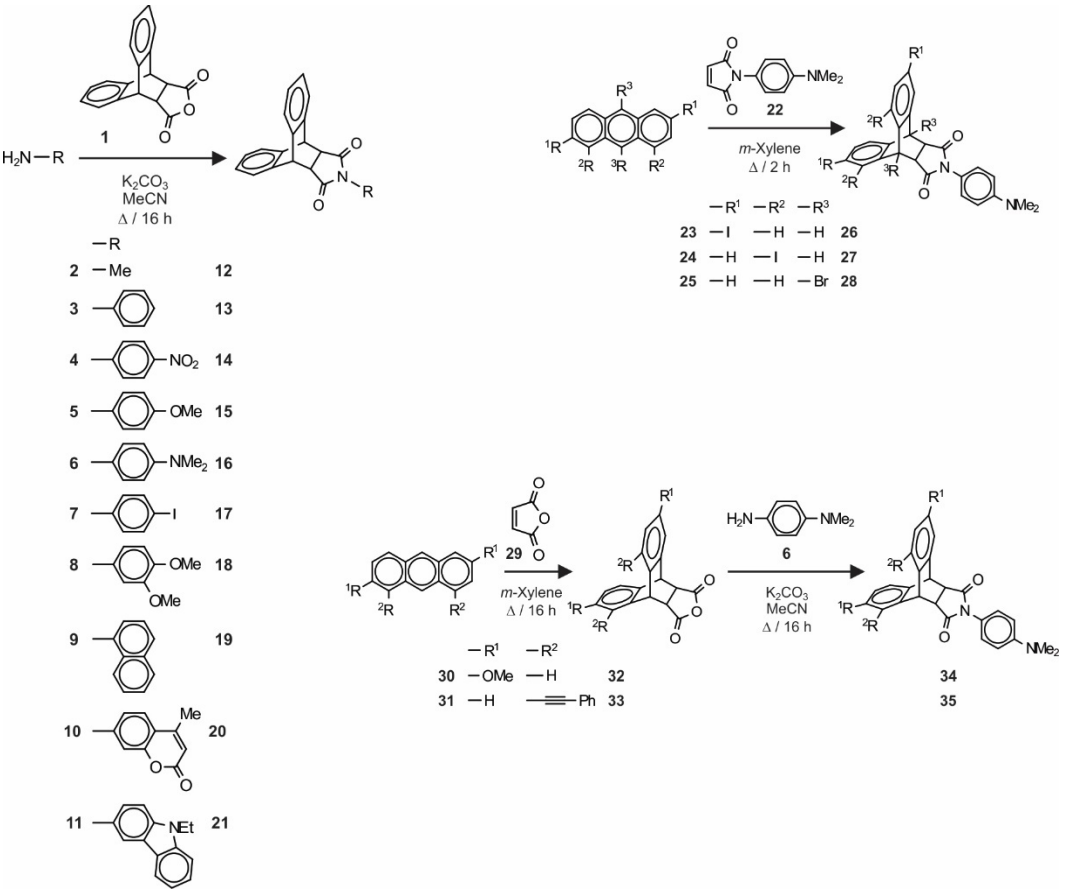

Figure 2.1 Synthesis of **12**–**29**, **26**–**28** and **34** –**35**.

The structural identity of all compounds was confirmed by electrospray ionization mass spectrometry as well as ^{1}H and ^{13}C nuclear magnetic resonance (NMR) spectroscopies. In addition, single crystals suitable for X-ray diffraction analysis were obtained for **15**, **16**, **18**–**21**, **28**, **34** and **35**. The resulting structures (Figure 2.2 and Tables 2.1-2.3) clearly reveal the maleimide bridge across positions 9 and 10 of the anthracene platform in all instances. The sp^3 hybridization of the two bridgehead carbon atoms forces the peripheral

ortho-phenylene rings out of planarity and interrupts electronic delocalization, in agreement with the rationale behind the design of these compounds.

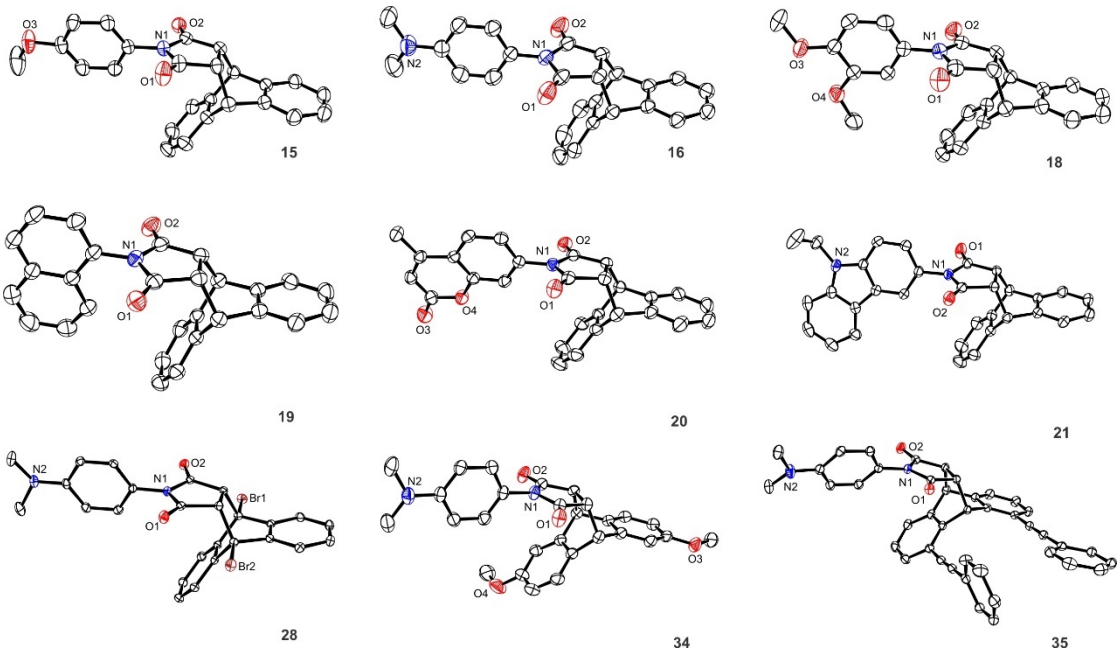

Figure 2.2 ORTEP representations of the geometries adopted by **15**, **16**, **18**–**21**, **28**, **34** and **35** in single crystals, showing 30% (**15**, **34)**, 40% (**19**, **20**, **21)** and 50% (**16**, **18**, **28**, **35**) thermal ellipsoid probability.

2.2.2. Photochemical and photophysical properties

The absorption spectrum of anthracene (**36** in Figure 2.3) in acetonitrile shows the characteristic vibronic structure of this oligoacene chromophore between 300 and 390 nm (***a*** in Figure 2.3). Excitation within this range of wavelengths results in intense fluorescence (***b*** in Figure 2.3). The introduction of a maleimide bridge across positions 9 and 10 isolates electronically the two peripheral phenylene rings, alters drastically the absorption spectrum and suppresses fluorescence. For example, the absorption and emission spectra of adduct **12** do not reveal any bands at wavelengths longer than 300 nm, under otherwise identical experimental conditions.

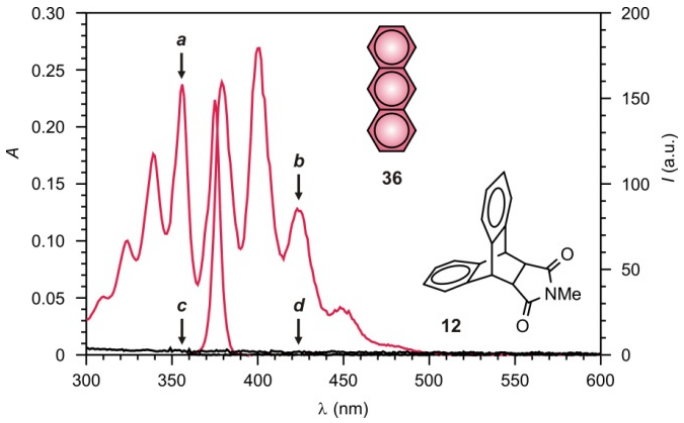

Figure 2.3 Absorption and emission spectra (MeCN, 25 °C, λ_{Ex} = 350 nm) of **36** (30 μM, ***a*** and ***b***) and **12** (0.1 mM, ***c*** and ***d***).

Ultraviolet illumination (254 nm, 0.4 mW cm^{-2}) of adducts **12**–**21** in acetonitrile results in noticeable absorption and emission changes only for **16** and **17**. Specifically, comparison of the absorption and emission spectra recorded before (***a*** and ***b*** in Figure 2.4) to those measured after (***c*** and ***d*** in Figure 2.4) irradiation of **16** reveals the appearance of the characteristic anthracene bands. Indeed, retro-cycloaddition of **16** occurs upon excitation to form **22** and **36**. A plot of the absorbance evolution at 355 nm during photolysis indicates the quantum yield (ϕ_P in Table 2.1) for this photochemical transformation to be 0.001.[i] In contrast to the behavior of **16**, illumination of **17** does not result in the formation of **36**. Instead of the anthracene bands, an absorption centered at 359 nm together with a weak and broad emission appear in the spectra recorded after relatively short irradiation times (***a***–***d*** in Figure 2.5).

[i] The absorption and emission spectra of an acetonitrile solution of **16** do not reveal any change even after heating under reflux for 6 hours in the dark. Thus, this particular cycloadduct is thermally stable and dissociates into its constituent components only under ultraviolet illumination.

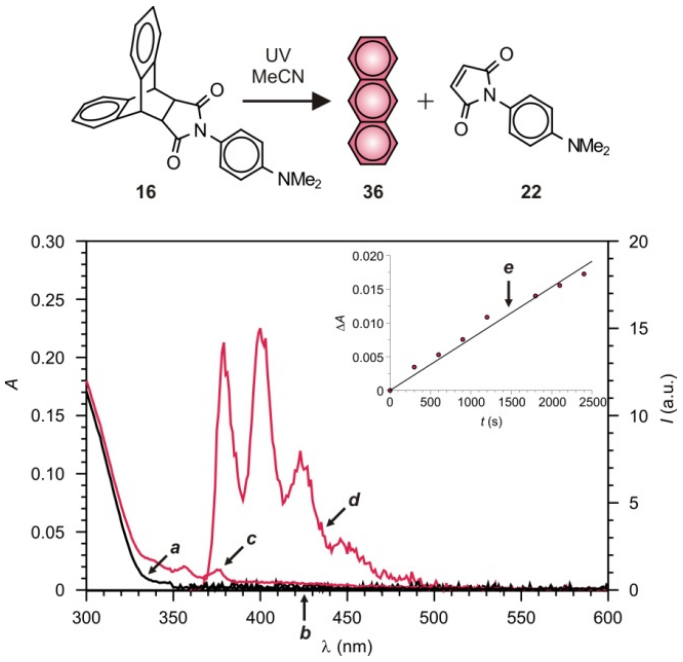

Figure 2.4 Absorption and emission spectra of **16** (20 μM, MeCN, 25 °C, λ_{Ex} = 350 nm) before (**a** and **b**) and after (**c** and **d**) ultraviolet (UV) irradiation (254 nm, 0.4 mW cm^{-2}, 40 min) and the corresponding absorbance evolution at 355 nm during photolysis.

The absorption spectrum (***a*** in Figure 2.6) of **12** indicates the molar extinction coefficient (ε) to be less than 1 mM^{-1} cm^{-1} between 240 and 300 nm. The introduction of a 4-dimethylaminophenyl chromophore on the maleimide bridge, in the shape of **16**, translates into the appearance of an intense band within this range of wavelengths with a ε of 21 mM^{-1} cm^{-1} at 264 nm (***b*** in Figure 2.6). These observations indicate that this particular chromophoric fragment is mainly responsible for absorbing the exciting photons and initiating the photochemical transformation of **16** into **22** and **36**.

Table 2.1 Quantum yield (ϕ_P) for the photochemical retro-cycloadditions and fluorescence quantum yield (ϕ_F) of the resulting anthracenes [a].

	ϕ_P	ϕ_F
16 → 36	0.001	0.27
28 → 25	0.01	0.07
34 → 30	0.001	0.43
35 → 31	0.002	0.85

[a] All measurements were performed in aerated MeCN at 25 °C. Samples were illuminated at 254 nm. The irradiation power per unit area (0.4 mW cm^{-2}) was measured with a potassium ferrioxalate actinometer and this value was used to determine ϕ_P from the corresponding absorbance evolution during photolysis, according to an established procedure (ref. [190]). The values of ϕ_F listed for **25**, **30** and **36** are literature data (ref.[191]) that of **31** was determined against an EtOH solution of 9,10-diphenylanthracene. The value of ϕ_F for this standard is 0.95 (ref.[192]).

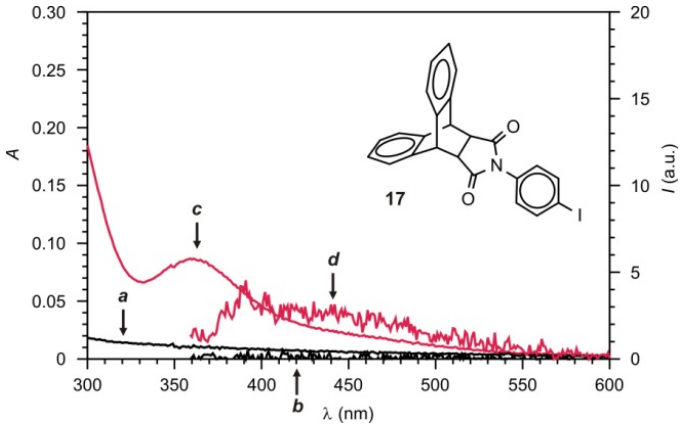

Figure 2.5 Absorption and emission spectra of **17** (40 μM, MeCN, 25 °C, λ_{Ex} = 350 nm) before (**a** and **b**) and after (**c** and **d**) ultraviolet irradiation (254 nm, 0.4 mW cm^{-2}, 5 min).

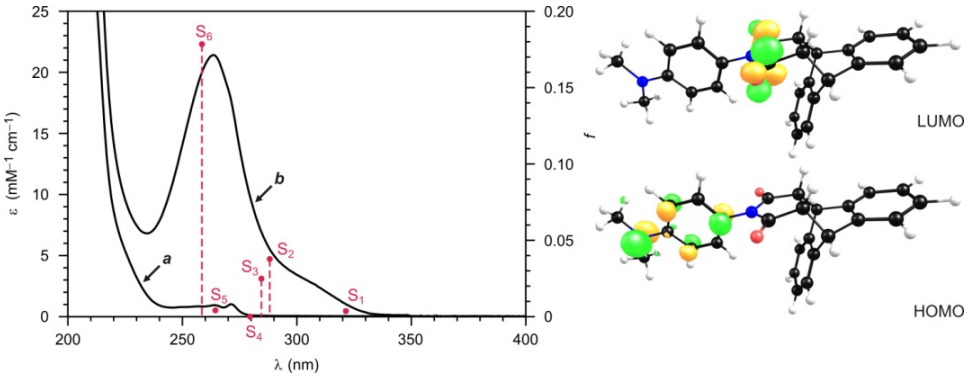

Figure 2.6 Experimental absorption spectra (MeCN, 25 °C) of **12** (***a***) and **16** (***b***) together with calculated [B3LYP/6-311+G(d,p), IEFPCM for MeCN] singlet excited states of **16** and isosurfaces for the main orbital pair associated with the $S_0 \rightarrow S_1$ transition.

Density functional theory (DFT) calculations assign the main band of **16** to a $S_0 \rightarrow S_6$ transition (Figure 2.6) with estimated wavelength (λ_{Cal}) and oscillator strength (f_{Cal}) of 259 nm and 0.179 respectively (Table 2.4 in experimental section). Instead, λ_{Cal} for the $S_0 \rightarrow S_1$ transition is 321 nm with a f_{Cal} of only 0.004, in agreement with the presence of a relatively weak band in the experimental spectrum (***b*** in Figure 2.6) at this wavelength. Visualization of the main orbital pair responsible for this electronic transition reveals that the highest-occupied molecular orbital (HOMO in Figure 2.6) is mostly localized on the 4-dimethylaminophenyl ring, while the lowest unoccupied molecular orbital (LUMO in Figure 2.6) is predominantly on the imide group. In fact, the orthogonal arrangement of one relative to the other, evident also in the crystal structure (Figure 2.2), isolates electronically the two groups in the ground state. Thus, the population of S_1 results essentially in the formal transfer of one electron from the 4-dimethylaminophenyl ring to the imide group.

The dissociation of adduct **16** into diene **36** and dienophile **22** can be simulated by elongating stepwise one of the two [C–C] bonds joining the anthracene and maleimide fragments. The energies for S_0, S_1 and T_1 of the optimized geometries at each step can then be plotted against the bond length to build the reaction profiles illustrated in Figure 2.7. In S_0, the energy increases monotonically and dramatically with bond length in full agreement with experiments, which did not reveal any thermal dissociation of the cycloadduct into its constituent components even after heating for prolonged time.[i] In fact, frequency calculations indicate the free energy of the transition state, found along this reaction path, to be 33.94 kcal mol^{-1} greater than that of **16** (Figure 2.8). Instead, the free energy of the two separate products is only 3.67 kcal mol^{-1} higher than that of the cycloadduct.

In contrast to the reaction profile in S_0 (Figure 2.7), the energy remains almost constant in S_1 ($\Delta E < 0.2$ eV) and, after a modest initial increase ($\Delta E = 0.6$ eV), decreases significantly in T_1. Thus, the retro-cycloaddition of **16** into **22** and **36** can, indeed, proceed photochemically and it can evolve along the potential energy surface of either one of these two excited states. Presumably, ultraviolet illumination of **16** results predominantly in the population of S_6 (Figure 2.6). Then, **16** can decay to S_1, after internal conversion, and either dissociate along the relatively flat potential energy surface of this state or undergo intersystem crossing and dissociate in T_1.

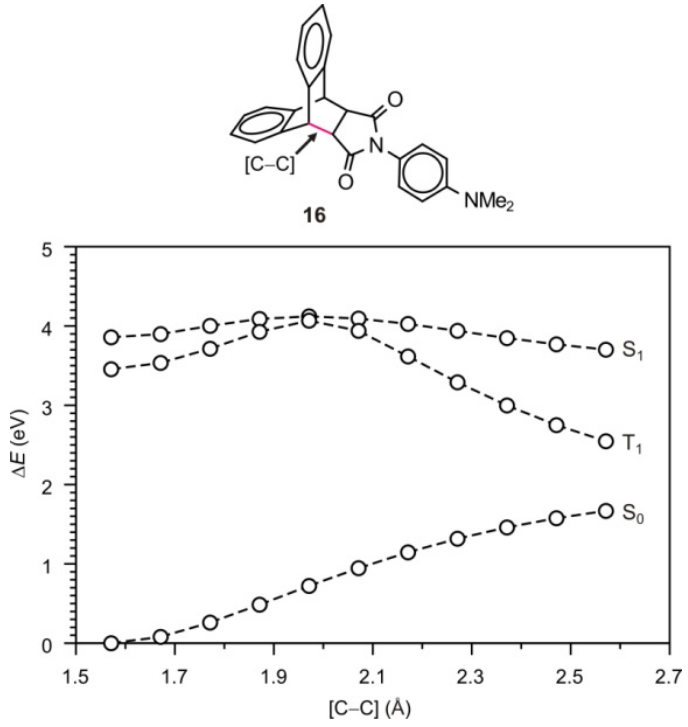

Figure 2.7 Relative energies [B3LYP/6-311+G(d,p), IEFPCM for MeCN] of **16** in S_0, S_1 and T_1 against the length of one of the two [C–C] bonds joining the anthracene and maleimide fragments.

Adducts **12**–**21** differ exclusively in the nature of their maleimide bridge. Their spectroscopic analysis, together with the DFT calculations on **16**, indicate that a 4-dimethylaminophenyl group is essential on the bridging unit for the photochemical

dissociation of these adducts to occur. Adducts **26**–**28**, **34** and **35** all have this particular group on their maleimide bridge and differ instead in the substituents on the anthracene fragment. In all instances, ultraviolet illumination results in significant changes in absorption and emission. The spectra (Figures 2.9 and 2.10) of **26** and **27**, however, do not reveal the characteristic band of the corresponding anthracene derivates after irradiation. Instead, an absorption at *ca.* 355 nm together with a broad and weak emission appear for both compounds. These bands resemble the ones detected for **17** (Figure 2.5).

All three cycloadducts have iodide substituents and such heavy atoms are known to encourage intersystem crossing.[191] Presumably, a photochemical pathway in competition with the expected retro-cycloaddition is promoted for all three compounds via the efficient population on the corresponding triplet states.

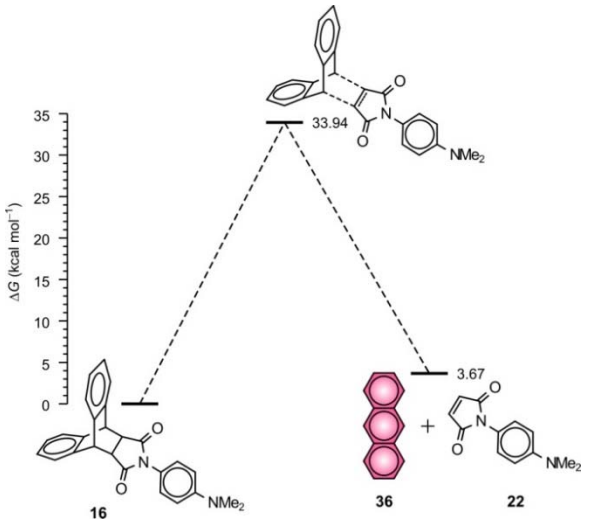

Figure 2.8 Relative free energies [B3LYP/6-311+G(d,p), IEFPCM for MeCN] of adduct **16**, products **22** and **36** and the corresponding transition state.

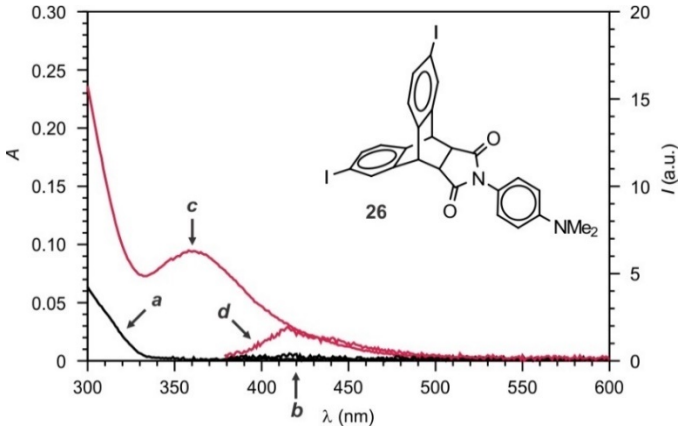

Figure 2.9 Absorption and emission spectra of **26** (40 μM, MeCN, 25 °C, λ_{Ex} = 373 nm) before (***a*** and ***b***) and after (***c*** and ***d***) ultraviolet irradiation (254 nm, 0.4 mW cm^{-2}, 5 min).

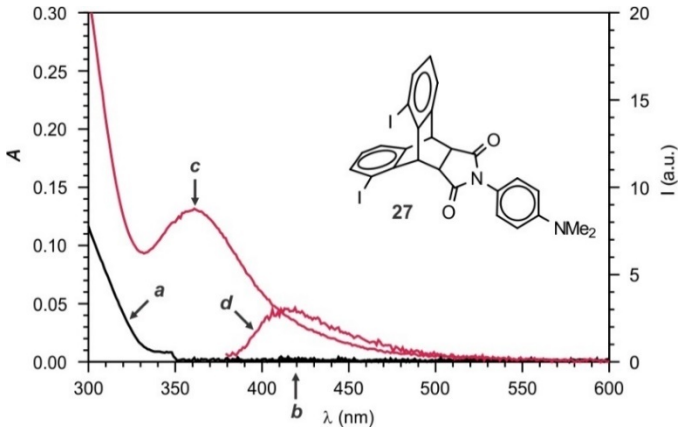

Figure 2.10 Absorption and emission spectra of **27** (20 μM, MeCN, 25 °C, λ_{Ex} = 370 nm) before (**a** and **b**) and after (**c** and **d**) ultraviolet irradiation (254 nm, 0.4 mW cm^{-2}, 5 min).

In contrast to the behavior of **26** and **27**, cycloadducts **28**, **34** and **35** undergo photoinduced retro-cycloaddition. In all instances, the characteristic absorption and emission bands (Figures 2.11-2.13) of the corresponding anthracene derivatives develop under illumination. Plots of the absorbance evolution during photolysis indicates ϕ_P to range from 0.001 up to 0.01 (Table 2.1). Interestingly, ϕ_P of **28** is one order of magnitude greater than those of **16**, **34** and **35**.

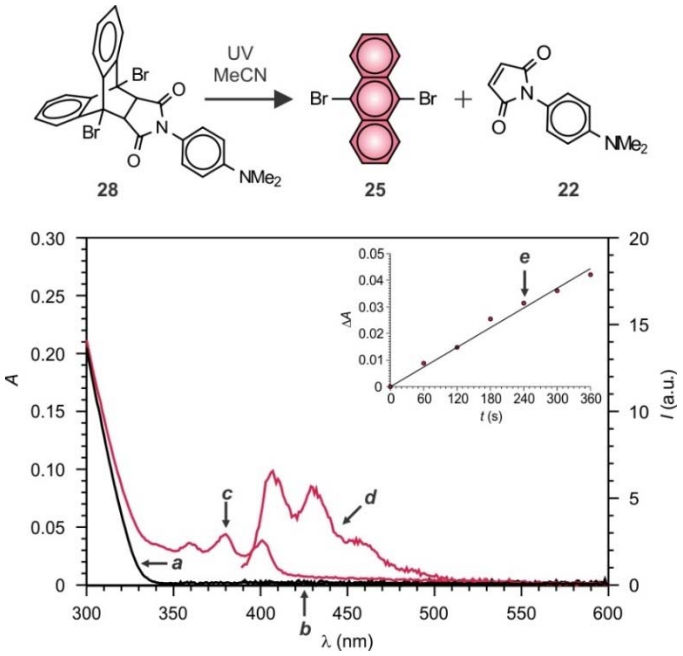

Figure 2.11 Absorption and emission spectra of **28** (40 μM, MeCN, 25 °C, λ_{Ex} = 370 nm) before (***a*** and ***b***) and after (***c*** and ***d***) ultraviolet (UV) irradiation (254 nm, 0.4 mW cm^{-2}, 6 min) and the corresponding absorbance evolution at 380 nm during photolysis.

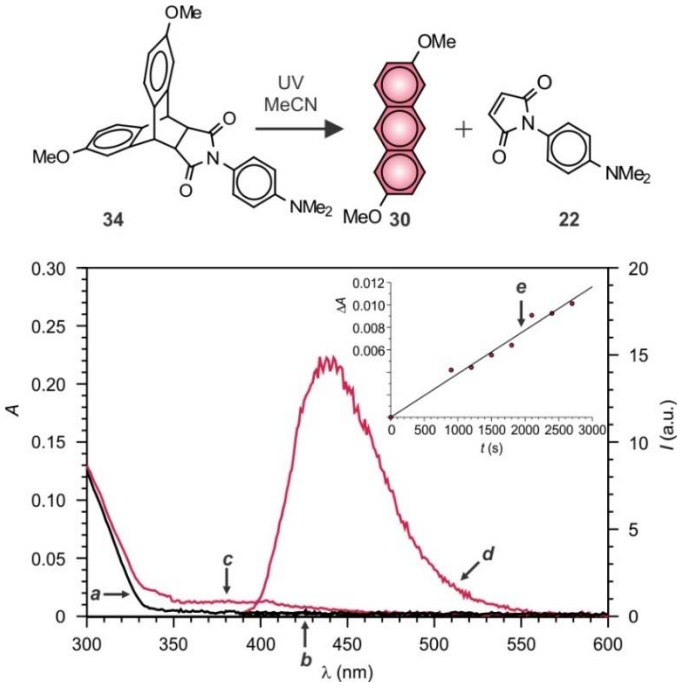

Figure 2.12 Absorption and emission spectra of **34** (30 μM, MeCN, 25 °C, λ_{Ex} = 350 nm) before (***a*** and ***b***) and after (***c*** and ***d***) ultraviolet (UV) irradiation (254 nm, 0.4 mW cm^{-2}, 50 min) and the corresponding absorbance evolution at 401 nm during photolysis.

Presumably, the steric hindrance associated with the two bromine substituents on the bridgehead carbon atoms of **28** facilitates the dissociation of this particular adduct into the corresponding diene and dienophile.By contrast, the introduction of a pair of methoxy or phenylethynyl substituents on the two *ortho*-phenylene rings, in the shape of **34** or **35** respectively, has negligible influence on ϕ_P, which remains almost identical to that of **16**.

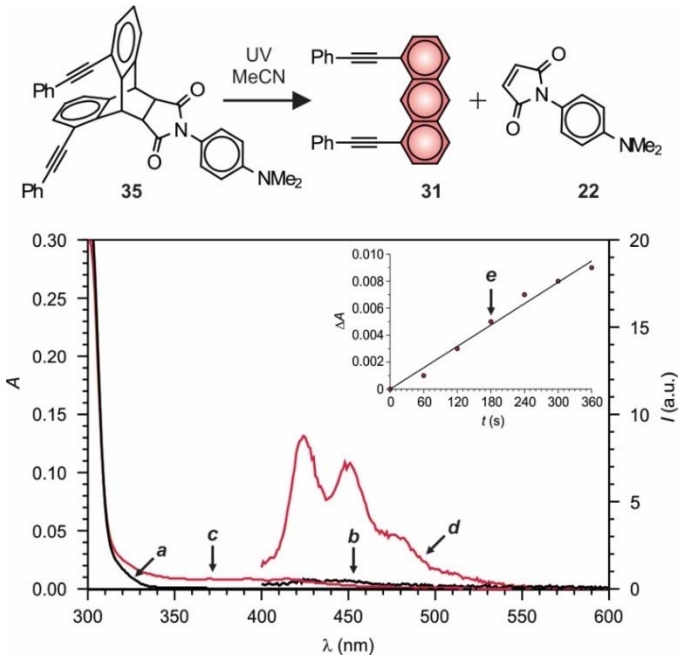

Figure 2.13 Absorption and emission spectra of **35** (10 μM, MeCN, 25 °C, λ_{Ex} = 390 nm) before (***a*** and ***b***) and after (***c*** and ***d***) ultraviolet (UV) irradiation (254 nm, 0.4 mW cm^{-2}, 6 min) and the corresponding absorbance evolution at 392 nm during photolysis.

Nonetheless, the two phenylethynyl groups have a pronounced influence on the fluorescence quantum yield (ϕ_F in Table 2.1) of the photochemical product. Indeed, **31** has the greatest ϕ_F out of the four photoactivatable anthracenes investigated and, therefore, is the best candidate for possible imaging applications based on this family of photoactivatable fluorophores.[193-195]

2.3. Conclusions

The reaction of the maleic anhydride cycloadduct of anthracene with substituted anilines offers convenient synthetic access to the corresponding maleimide cycloadducts in good yields. In the resulting compounds, the maleimide bridge, across position 9 and 10 of the oligoacene platform, isolates the peripheral *ortho*-phenylene rings and suppresses the characteristic absorption and emission bands of the anthracene chromophore. When a 4-dimethylamino group is attached to the nitrogen atom of the maleimide bridge, ultraviolet illumination results in retro-cycloaddition with a quantum yield of 0.001 to regenerate anthracene and of its spectroscopic signature. The 4-dimethylamino appendage collects the exciting photons effectively and encourages the population of the excited state responsible for the photochemical regeneration of anthracene. The introduction of substituents, in the form of a pair of bromine atoms, on the bridgehead carbon atoms of the *N*-4-dimethylemminomaleimide cycloadduct facilitates the photochemical transformation and brings the corresponding quantum yield up to 0.01. Instead, the presence of substituents on the peripheral *ortho*-phenylene rings of the cycloadduct has negligible influence on the quantum efficiency of the photochemical process. These groups, however, can be exploited to regulate the photophysical properties of the photochemical product. When a pair of phenylethynyl groups are attached to positions 2 and 8 of the anthracene chromophore the fluorescence quantum yields raises up to 0.85. Thus, these particular operating principles provide the possibility to convert photochemically a nonfluorescent reactant into a fluorescent product and, hence to activate fluorescence efficiently under the influence of optical stimulations. As a result, this structural design can evolve into the

realization of valuable molecular probes for imaging applications designed around fluorescence photoactivation.

2.4. Experimental section

2.4.1. Materials and methods

Chemicals were purchased from commercial sources and used as received with the exception of MeCN, which was distilled over CaH_2. Compounds **1**, **12**–**15**, **22** and **30**–**32** were prepared according to literature procedures.[187-189,196-198] Electrospray ionization mass spectra (ESIMS) were recorded with a TOF-Q spectrometer. NMR spectra were recorded with 300 and 400 MHz spectrometers. Absorption spectra were recorded in quartz cells with a path length of 1.0 cm. Emission spectra were recorded in aerated solutions. The value of ϕ_F for **31** was determined with a 9,10-diphenylanthracene standard, following a literature protocol.[1] Solutions were irradiated either at 254 nm (0.4 mW cm^{-2}) or at 350 nm (2.5 mW cm^{-2}). The values of ϕ_P were determined with a potassium ferrioxalate actinometer, according to an established procedure.[190]

2.4.2. General procedure for the synthesis of 16–21

An equimolar solution of **1** (138 mg, 0.5 mmol) and the corresponding amine (**2**–**11**) in MeCN (5 mL) was heated under reflux for 16 hours over K_2CO_3 (112 mg, 0.8 mmol). After cooling down to ambient temperature, the mixture was diluted with CH_2Cl_2 (30 mL) and washed with H_2O (20 mL). The combined organic layers were dried over Na_2SO_4, the solvent as distilled off under reduced pressure and the residue was purified by column chromatography (SiO_2).

16: AcOEt/hexanes (1.5:3.5, v/v). White solid (120 mg, 60%). ESIMS: *m*/*z* = 395.1758 $[M + H]^+$ (*m/z* calcd. for $C_{26}H_{23}N_2O_2$ = 395.1761); ^1H NMR (CD_3CN): δ = 2.88 (6H, s),

3.23 (2H, s), 4.82 (2H, s), 6.23 (2H, d, 9 Hz), 6.59 (2H, d, 9 Hz), 7.18–7.26 (4H, m), 7.28–7.33 (2H, m), 7.44–7.51 (2H, m); ^{13}C NMR ($CDCl_3$): δ = 40.8, 46.3, 47.3, 112.8, 120.1, 124.7, 125.6, 127.2, 127.4, 127.5, 139.2, 141.8, 150.9, 177.2.

17: AcOEt/hexanes (1:4, v/v). Yellow solid (80 mg, 32%). ESIMS: *m*/*z* = 478.0296 [M + H]$^+$ (*m/z* calcd. for $C_{24}H_{17}INO_2$ = 478.0305); ^{1}H NMR ($CDCl_3$): δ = 3.38 (2H, s), 4.89 (2H, s), 6.29 (2H, d, 8 Hz), 7.19–7.24 (4H, m), 7.32–7.36 (2H, m), 7.41–7.45 (2H, m), 7.64 (2H, d, 8 Hz); ^{13}C NMR ($CDCl_3$): δ = 46.3, 47.5, 80.0, 94.8, 117.7, 124.8, 125.5, 127.3, 127.6, 128.5, 131.4, 138.3, 138.7, 139.1, 141.5, 146.5, 176.2.

18: AcOEt/hexanes (3:2, v/v). White solid (130 mg, 63%). ESIMS: *m*/*z* = 434.1375 [M + Na]$^+$ (*m/z* calcd. for $C_{26}H_{21}NO_4Na$ = 434.1368); ^{1}H NMR ($CDCl_3$): δ = 3.38 (2H, s), 3.72 (3H, s), 3.82 (3H, s), 4.90 (2H, s), 5.73 (1H, s), 6.14 (1H, d, 9 Hz), 6.76 (1H, d, 9 Hz), 7.19–7.24 (4H, m), 7.33–7.39 (2H, m), 7.40–7.46 (2H, m); ^{13}C NMR ($CDCl_3$): δ = 46.3, 47.4, 56.4, 110.1, 111.4, 119.5, 124.4, 124.8, 125.6, 127.3, 127.4, 139.4, 141.6, 149.6, 149.7, 176.9.

19: AcOEt/hexanes (1:4, v/v). White solid (92 mg, 46%). ESIMS: *m*/*z* = 424.1302 [M + Na]$^+$ (*m/z* calcd. for $C_{28}H_{19}NO_2Na$ = 424.1313); ^{1}H NMR (CD_3CN): δ = 3.56 (2H, s), 4.95 (2H, s), 5.32 (1H, d, 8Hz), 7.16–7.31 (4H, m), 7.40–7.56 (8H, m), 7.88–7.90 (1H, m), 7.94 (1H, d, 8 Hz); ^{13}C NMR ($CDCl_3$): δ = 45.9, 46.4, 47.8, 47.9, 122.3, 124.7, 124.8, 125.6, 125.7, 126.2, 126.3, 126.8, 127.3, 127.4, 127.7, 127.9, 128.5, 128.9, 129.5, 130.2, 130.4, 134.5, 139.4, 139.9, 141.7, 142.2, 176.7, 176.8.

20: AcOEt/CH_2Cl_2 (1:4, v/v). White solid (82 mg, 38%). ESIMS: *m*/*z* = 434.1376 [M + H]$^+$ (*m/z* calcd. for $C_{28}H_{20}NO_4$ = 434.1394); ^{1}H NMR ($CDCl_3$): δ = 2.40 (3H, s), 3.43 (2H, s), 4.91 (2H, s), 6.29 (1H, s), 6.58 (1H, s), 7.21–7.26 (4H, m), 7.33–7.39 (2H, m), 7.42–

7.47 (2H, m), 7.54 (2H, d, 8 Hz); ^{13}C NMR ($CDCl_3$): δ = 19.0, 30.1, 46.3, 47.5, 115.6, 116.1, 120.4, 122.5, 124.8, 125.5, 127.4, 127.8, 134.5, 139.0, 141.4, 151.9, 153.8, 160.5, 175.9.

21: AcOEt/hexanes (2:3, v/v). White solid (85 mg, 36%). ESIMS: *m*/*z* = 491.1724 [M + Na]$^+$ (*m/z* calcd. for $C_{32}H_{24}N_2O_2Na$ = 491.1735); ^{1}H NMR (CD_3CN): δ = 1.34 (3H, t, 6 Hz), 3.43 (2H, s), 4.38 (2H, q, 6 Hz), 4.89 (2H, s), 6.48 (1H, d, 9 Hz), 7.03 (1H, s), 7.20–7.27 (3H, m), 7.31–7.45 (5H, m), 7.47–7.56 (4H, m), 8.00 (1H, d, 9 Hz); ^{13}C NMR ($CDCl_3$): δ = 13.8, 37.6, 46.0, 47.1, 50.9, 108.7, 108.9, 119.0, 119.2, 120.6, 122.4, 123.3, 123.7, 124.4, 125.3,126.2, 126.9, 127.2, 139.0, 139.6, 140.3, 141.4, 177.1.

2.4.3. General procedure for synthesis of 26–28

An equimolar solution of **22** (108 mg, 0.5 mmol) and the corresponding anthracene derivative (**23**–**25**) in *m*-xylene (5 mL) was heated under reflux for 16 hours. After cooling down to ambient temperature, the solvent was distilled off under reduced pressure and the residue was purified by column chromatography (SiO_2).

26: AcOEt/hexanes (1:4 v/v). Yellow solid (116 mg, 36%). ESIMS: *m*/*z* = 646.9717 [M + H]$^+$ (*m/z* calcd. for $C_{26}H_{21}I_2N_2O_2$ = 646.9694); ^{1}H NMR (CD_3CN): δ = 2.92 (6H, s), 3.35 (2H, s), 4.79 (2H, s), 6.29 (2H, d, 8 Hz), 6.65 (2H, d, 8 Hz), 7.11 (1H, d, 8 Hz), 7.27 (1H, d, 8 Hz), 7.61 (2H, t, 8 Hz), 7.70 (1H, s), 7.86 (1H, s); ^{13}C NMR ($CDCl_3$): δ= 40.9, 45.3, 45.4, 46.6, 46.9, 92.4, 92.7, 112.9, 126.6, 127.3, 127.4, 133.8, 134.3, 136.4, 136.7, 138.3, 140.8, 141.1, 143.6, 151.0, 151.2, 176.4.

27: AcOEt/hexanes (2:3 v/v). Yellow solid (178 mg, 55%). ESIMS: *m*/*z* = 646.9692 [M + H]$^+$ (*m/z* calcd. for $C_{26}H_{21}I_2N_2O_2$ = 646.9694); ^{1}H NMR (CD_3CN): δ = 2.90 (6H, s), 3.36 (2H, s), 4.86 (1H, s), 5.48 (1H, s), 6.30 (2H, d, 6 Hz), 6.63 (2H, d, 6 Hz), 6.99 (2H, t, 6

Hz), 7.33 (1H, d, 6 Hz), 7.48 (1H, d, 9 Hz), 7.68–7.77 (2H, m); ^{13}C NMR (CDCl3): δ =40.8, 46.1, 46.6, 47.9, 53.6, 95.3, 96.3, 112.8, 120.0, 124.6, 125.6, 127.3, 129.2, 129.3, 137.5, 137.8, 143.0, 143.5, 144.9, 150.9, 175.4, 176.6.

28: AcOEt/hexanes (2:3 v/v). Yellow solid (105 mg, 38%). ESIMS: *m/z* = 552.9945 [M + H]$^+$ (*m/z* calcd. for $C_{26}H_{21}Br_2N_2O_2$ = 552.9949); ^{1}H NMR (CD_3CN): δ = 2.91 (6H, s), 3.64 (2H, s), 6.40 (2H, d, 8 Hz), 6.57 (2H, d, 8 Hz), 7.35–7.43 (4H, m), 7.79–7.83 (2H, m), 7.98–8.03 (2H, m); ^{13}C NMR ($CDCl_3$): δ= 40.8, 55.4, 64.3, 112.5, 119.9, 125.9, 125.9, 127.2, 128.7, 129.0, 137.2, 140.1, 150.9, 171.8.

2.4.4. Synthesis of 33

A solution of **29** (40 mg, 0.4 mmol) and **31** (150 mg, 0.4 mmol) in *m*-xylene (5 mL) was heated under reflux for 16 hours. After cooling down to ambient temperature, the mixture was cooled further with an ice bath and the resulting precipitate was filtered off. The solid residue was washed with hexane and then crystallized with *m*-xylene to give **33** (80 mg, 42%) as a white solid. ESIMS: *m/z* = 499.1293 [M + Na]$^+$ (*m/z* calcd. for $C_{34}H_{20}O_3Na$ = 499.1310); ^{1}H NMR (CD_3CN): δ = 3.68–3.74 (1H, m), 3.77–3.83 (1H, m), 5.00 (1H, s), 5.96 (1H, s), 7.19–7.32 (6H, m), 7.34–7.54 (10H, m); ^{13}C NMR ($CDCl_3$): δ = 41.5, 46.1, 47.5, 48.1, 86.0, 86.1, 94.2, 94.3, 120.4, 121.3, 122.9, 123.3, 124.6, 125.5, 127.4, 127.9, 128.7, 128.8, 128.9, 131.0, 131.5, 132.2, 132.3, 138.9, 139.5, 141.4, 141.9, 144.7, 169.8, 170.8.

2.4.5. General procedure for the synthesis of 34 and 35

An equimolar solution of **6** (0.2 mmol) and the corresponding anthracene derivative (**32** or **33**) in MeCN (5 mL) was heated under reflux for 16 hours over K_2CO_3 (42 mg, 0.3 mmol). After cooling down to ambient temperature, the mixture was diluted with CH_2Cl_2 (30 mL)

and washed with H_2O (20 mL). The combined organic layers were dried over Na_2SO_4, the solvent as distilled off under reduced pressure and the residue was purified by column chromatography [SiO_2, AcOEt/hexanes (2:3, v/v)] to give the product.

34: White solid (50 mg, 55%). ESIMS: *m/z* = 455.1975 $[M + H]^+$ (*m/z* calcd. for $C_{28}H_{27}N_2O_4$ = 455.1973); ^{1}H NMR (CD_3CN): δ = 2.90 (6H, s), 3.29 (2H, s), 3.76 (3H, s), 3.78 (3H, s), 4.71 (2H, s), 6.30 (2H, d, 8 Hz), 6.63 (2H, d, 8 Hz), 6.74 (2H, t, 8 Hz), 6.89 (1H, s), 7.07 (1H, s), 7.19 (1H, d, 8 Hz), 7.35 (1H, d, 8 Hz); ^{13}C NMR ($CDCl_3$): δ = 40.8, 45.8, 47.4, 47.6, 55.9, 56.0, 111.2, 111.4, 112.6, 112.8, 120.2, 120.3, 125.4, 126.3, 127.4, 131.1, 133.8, 141.1, 143.8, 150.9, 158.9, 159.3, 177.1, 177.3.

35: White solid (40 mg, 45%). ESIMS: *m/z* = 595.2409 $[M + H]^+$ (*m/z* calcd. for $C_{42}H_{31}N_2O_2$ = 595.2387); ^{1}H NMR [$(CD_3)_2CO$]: 2.90 (6H, s), 3.47–3.51 (1H, m), 3.53–3.57 (1H, m), 5.01 (1H, s), 6.03 (1H, s), 6.42 (2H, d, 8 Hz), 6.60 (2H, d, 8 Hz), 7.16–7.20 (2H, m), 7.26–7.35 (5H, m), 7.37–7.48 (6H, m), 7.55–7.63 (3H, m); ^{13}C NMR ($CDCl_3$): δ = 29.7, 40.4, 41.6, 46.0, 46.2, 46.6, 86.1, 86.3, 112.5, 119.9, 120.7, 122.7, 123.2, 124.2, 125.1, 126.6, 126.8, 127.0, 128.2, 128.3, 130.3, 130.4, 131.8, 132.0, 139.2, 140.0, 141.8, 142.3, 150.5, 175.5, 176.5.

2.4.6. Crystallographic analysis

Single crystals of **15**, **18** and **21** were obtained after diffusion of Et_2O vapors into a CH_2Cl_2 solution of the corresponding compound. Single crystals of **16** were obtained after diffusion of hexane vapors into a $CHCl_3$ solution of the compound. Single crystals of **19** and **28** were obtained after diffusion of Et_2O vapors into a $CHCl_3$ solution of the corresponding compound. Single crystals of **20** were obtained after diffusion of hexane/Et_2O (2:1, v/v) vapors into a $CHCl_3$ solution of the compound. Single crystals of

34 were obtained after diffusion of Et_2O vapors into an EtOAc solution of the compound. Single crystals of **35** were obtained after diffusion of hexane vapors into a MeCN solution of the compound. The data crystal of **15**, **16**, **18**–**21** and **34** was glued onto the end of a thin glass fiber. The data crystals of **28** and **35** were mounted onto the end of a thin glass fiber using Paratone-N for data collection at 100 K under flow of N_2. X-ray intensity data were measured with a CCD-based diffractometer, using Mo Kα radiation (λ = 0.71073 Å).[ii] The raw data frames were integrated with a narrow-frame integration algorithm. Corrections for Lorentz and polarization effects were applied. An empirical absorption correction based on the multiple measurement of equivalent reflections was applied. The structures were solved by a combination of direct methods and difference Fourier syntheses and refined by full-matrix least-squares on F^2.[iii] All non-hydrogen atoms were refined with anisotropic displacement parameters. Hydrogen atoms were placed in geometrically-idealized positions and included as standard riding atoms during the least-squares refinements. Crystal data, data collection parameters and results of the analyses are listed in Tables 2.2-2.3.

Compounds **15**, **16**, **20**, **21**, **34** and **35** crystallized in the triclinic crystal system. The space group $P\bar{1}$ was assumed and confirmed by the successful refinement and solution of the structures. For compound **15**, two molecules are present in the asymmetric crystal unit. One molecule of MeCN co-crystallized with **35**. The solvent molecule was included in the

---

[ii] Apex2 Version 2.2-0 and SAINT+ Version 7.46A; Bruker Analytical X-ray System, Inc.Madison, Wisconsin, USA, 2007.

[iii] (a) Sheldrick, G. M. SHELXTL Version 6.1; Bruker Analytical X-ray Systems, Inc., Madison, Wisconsin, USA, 2000. (b) Sheldrick, G. M. *Acta Cryst.* **2008**, *A64*, 112–122.

analysis and refined with anisotropic thermal parameters. Compound **18** crystallized in the orthorhombic crystal system. The systematic absences in the intensity data identified the unique space group $P2_12_12_1$. Compounds **19** and **28** crystallized in the monoclinic crystal system. The systematic absences in the intensity data identified the unique space group $P2_1/n$.

2.4.7. Computational methods

Density-functional theory[199] (DFT) calculations were performed with the 6-311+G(d,p) basis set and the restricted B3LYP[200,201] functional implemented in Gaussian 09.[202] Geometry optimizations, frequencies, molecular orbitals and excited states were computed with the polarizable continuum model (PCM) for acetonitrile, using the integral equation formalism (IEF) variant.[203]

The geometry adopted by **16** in single crystals (Figure 2.2) was optimized. No imaginary frequencies were found for the optimized structure. Molecular orbitals and the first ten singlet excited states were computed for this geometry (HOMO, LUMO and S_1–S_6 in Figure 2.6). The [C–C] bond between one of the two bridgehead carbon atoms and the corresponding maleimide carbon atom was elongated in 20 consecutive steps of 0.1 Å each. The remaining coordinates were optimized at each step and the first 5 singlet and 5 triplet excited states of each optimized geometry were computed.[iv, v] The energies of S_0, S_1 and

---

[iv] For comparison, the energies of the excited states for the first geometry were also computed with the unrestricted functional. However, no significant differences were observed between restricted and unrestricted triplet energies, in agreement with literature precedents (Cronstrand, P.; Rinkevicius, Z.; Luo, Y; Ågren, H. *J. Chem. Phys.* **2005**, *122*, 224104-1–10). As a result, the excited states for all geometries were computed with the restricted functional.

[v] The energy profiles for the two excited states were constructed on the basis of single-point calculations on ground-state geometries. Although this general protocol does not take into account the relaxation of each geometry in the corresponding excited state, it is known to provide a good qualitative estimate of the course

T_1 of each optimized geometry were plotted against the corresponding [C–C] distances (Figure 2.7). The geometry with highest S_0 energy (step 12) was optimized to a transition state with no distance constraint. The last geometry of the distance scan (step 20) shows the two separate products (**22** and **36**) was optimized further with no distance constraint. No imaginary frequencies were found. The free energies of transition state and products were computed relative to that of the very first geometry of the distance scan (Figure 2.7).

---

of a photochemical reaction and is computationally convenient. For examples, see: (a) Salassa, L.; Garino, C.; Salassa, G.; Gobetto, R.; Nervi, C. *J. Am. Chem. Soc.* **2008**, *130*, 9590–9597. (b) Iwamura, M.; Watanabe, H.; Ishii, K.; Takeuchi, S.; Tahara, T. *J. Am. Chem. Soc.* **2011**, 133, 7728–7736. (c) Raymo, F. M. *J. Phys. Chem. A* **2012**, *116*, 11888–11895.

Table 2.2 Crystallographic data for **15**, **16**, **18** and **19**

	15	**16**	**18**	**19**
Empirical Formula	$C_{25}H_{19}NO_3$	$C_{26}H_{22}N_2O_4$	$C_{26}H_{21}NO_4$	$C_{28}H_{19}NO_2$
Formula Weight	381.41	394.46	411.44	401.44
Crystal System	Triclinic	Triclinic	Orthorhombic	Monoclinic
Lattice Parameters:				
a (Å)	10.0356(4)	8.7939(4)	8.6359(3)	10.8929(6)
b (Å)	12.8316(5)	9.6279(4)	12.0457(5)	8.6496(5)
c (Å)	16.3402(7)	12.5660(6)	19.5543(8)	21.3698(13)
α (°)	80.535(1)	76.008(1)	90	90
β (°)	80.757(1)	78.669(1)	90	95.896(1)
γ (°)	74.556(1)	85.631(1)	90	90
V (Å^3)	1985.42(14)	1011.77(8)	2034.15(14)	2002.8
Space Group	$P\bar{1}$ (# 2)	$P\bar{1}$ (# 2)	$P2_12_12_1$ (# 19)	$P2_1/n$ (# 14)
Z Value	4	2	4	4
ρ_{calc} (g cm^{-3})	1.276	1.295	1.343	1.331
μ (Mo Kα) (mm^{-1})	0.084	0.082	0.091	0.084
T (K)	296	296	296	296
$2\Theta_{max}$ (°)	51.0	54.0	60.0	52.0
No. Obs. ($I > 2\sigma(I)$)	5765	3760	5379	2958
No. Parameters	525	274	282	280
Goodness of Fit	1.018	1.040	1.036	1.029
Max. Shift in Cycle	0.00	0.00	0.001	0.00
*Residuals**: R1; wR2	0.0398; 0.0985	0.0394; 0.1020	0.0381; 0.0992	0.0394; 0.0947
Absorption Correction, Max/min	Multi-scan 0.9900/0.9688	Multi-scan 0.7465/0.6896	Multi-scan 0.7465/0.6987	Multi-scan 0.9967/0.9689
Largest Peak in Final Diff. Map (e$^-$ Å^{-3})	0.161	0.188	0.225	0.173

* $R = \Sigma_{hkl}(||F_{obs}| - |F_{calc}||)/\Sigma_{hkl}|F_{obs}|$; $R_w = [\Sigma_{hkl}w(|F_{obs}| - |F_{calc}|)^2/\Sigma_{hkl}wF_{obs}^2]^{1/2}$, $w = 1/\sigma^2(F_{obs})$; $GOF = [\Sigma_{hkl}w(|F_{obs}| - |F_{calc}|)^2/(n_{data} - n_{vari})]^{1/2}$

Table 2.3 Crystallographic data for **20**, **21**, **28** and **34**.

	20	**21**	**28**	**34**
Empirical Formula	$C_{28}H_{19}NO_4$	$C_{32}H_{24}N_2O_2$	$C_{26}H_{20}N_2O_2Br_2$	$C_{28}H_{26}N_2O_4$
Formula Weight	433.44	468.53	552.26	454.51
Crystal System	Triclinic	Triclinic	Monoclinic	Triclinic
Lattice Parameters:				
a (Å)	8.1852(4)	9.7650(4)	9.3468(4)	9.8381(8)
b (Å)	8.4437(4)	11.9476(5)	14.5715(6)	10.4824(9)
c (Å)	16.9210(9)	12.3011(5)	16.6456(6)	12.5322(11)
α (°)	97.887(1)	113.172(1)	90	74.656(1)
β (°)	93.333(1)	101.293(1)	105.260(1)	74.429(1)
γ (°)	111.291(1)	106.109(1)	90	71.299(1)
V (Å^3)	1071.93(9)	1189.59(8)	2187.15(15)	1156.45(17)
Space Group	$P\bar{1}$ (# 2)	$P\bar{1}$ (# 2)	$P2_1/n$ (# 14)	$P\bar{1}$ (# 2)
Z Value	2	2	4	2
ρ_{calc} (g cm^{-3})	1.343	1.308	1.677	1.305
μ (Mo Kα) (mm^{-1})	0.090	0.082	3.734	0.088
T (K)	296	296	100	296
$2\Theta_{max}$ (°)	54.0	55.0	58.0	55.0
No. Obs. ($I > 2\sigma(I)$)	3770	4623	5135	3115
No. Parameters	299	326	291	311
Goodness of Fit	1.020	1.030	1.019	1.027
Max. Shift in Cycle	0.00	0.001	0.003	0.00
*Residuals**: R1; wR2	0.0375; 0.0929	0.0396; 0.1018	0.0236; 0.0561	0.0455; 0.0994
Absorption Correction, Max/min	Multi-scan 0.9946/0.9631	Multi-scan 0.9919/0.9743	Multi-scan 0.7065/0.3311	Multi-scan 0.9930/0.9691
Largest Peak in Final Diff. Map (e$^-$ Å^{-3})	0.185	0.232	0.693	0.125

* $R = \Sigma_{hkl}(\,|\,|F_{obs}|-|F_{calc}|\,|)/\Sigma_{hkl}|F_{obs}|$; $R_w = [\Sigma_{hkl}w(|F_{obs}|-|F_{calc}|)^2/\Sigma_{hkl}wF_{obs}^2]^{1/2}$, $w = 1/\sigma^2(F_{obs})$; $GOF = [\Sigma_{hkl}w(|F_{obs}|-|F_{calc}|)^2/(n_{data}-n_{vari})]^{1/2}$

Table 2.4 Excitation energy (ΔE), wavelength (λ_{Cal}), oscillator strength (f_{Cal}) and main orbital pair with its contribution for electronic transitions from the ground state of **16** to the first ten singlet excited states.

	ΔE_{Cal} (eV)	λ_{Cal} (nm)	f_{Cal}	*Main Orbital Pair*	*Contribution* (%)
S_1	3.86	321	0.0037	[HOMO] → [LUMO]	97
S_2	4.30	288	0.0378	[HOMO] → [LUMO + 3]	95
S_3	4.36	285	0.0249	[HOMO] → [LUMO + 1]	97
S_4	4.44	280	0.0000	[HOMO] → [LUMO + 2]	98
S_5	4.69	264	0.0042	[HOMO] → [LUMO + 4]	90
S_6	4.80	259	0.1785	[HOMO] → [LUMO + 5]	43
S_7	4.87	254	0.0004	[HOMO – 1] → [LUMO]	96
S_8	4.93	251	0.0206	[HOMO – 6] → [LUMO]	62
S_9	4.95	250	0.3083	[HOMO] → [LUMO + 5]	50
S_{10}	5.02	247	0.0455	[HOMO – 1] → [LUMO + 2]	31

CHAPTER 3

AUTOCATALYTIC FLUORESCENCE PHOTOACTIVATION

3.1. Background

Replicating molecules catalyze their own formation from appropriate precursors.[204] In most instances, supramolecular contacts between product and reactants template the assembly of an identical copy of the former from the latter species. Under these conditions, the reaction rate increases, during the course of the chemical transformation, to impose a sigmoidal temporal dependence on the concentration of the replicating product.[205] Such a kinetic amplification is responsible for a diversity of biochemical processes and is believed to have played a fundamental role in the origin of life.[206] In fact, a number of artificial counterparts to replicating biomolecules have been developed already with the ultimate goal of elucidating the basic factors responsible for autocatalysis.[204] Photochemical analogues of supramolecular replicators remain, instead, limited to a few remarkable examples, mostly aimed at signaling molecular recognition with changes in fluorescence intensity.[207-216] Indeed, the unique kinetic profile of autocatalytic reactions can be exploited to impose the amplification on fluorescence signaling that is particularly convenient for chemical sensing.[217]

Photoactivatable fluorophores switch from a nonemissive to an emissive state under irradiation at an appropriate activation wavelength (λ_{Ac}).[152] Illumination of the resulting product at a given excitation wavelength (λ_{Ex}) then produces significant fluorescence. The concatenation of a photochemical reaction (activation) with a photophysical process (fluorescence) is therefore responsible for the operating principles of these photoresponsive compounds. Their unique behavior, in combination with the interplay of beams

illuminating at λ_{Ac} and λ_{Ex}, can be exploited to switch fluorescence on within a defined region of space at a particular interval of time. In turn, such a spatiotemporal control permits the monitoring of dynamic events in real time[20] and the visualization of samples with subdiffraction resolution.[163] Indeed, photoactivatable fluorophores are becoming invaluable probes for the investigation of the dynamic and structural properties of a diversity of specimens.

In the wake of our research efforts directed at the identification of viable structural designs to photoactivate fluorescence,[20,152,163] we realized that the photochemical and photophysical events responsible for switching emission on can be manipulated to engineer an autocatalytic transformation. Specifically, the structures of the nonemissive reactant and fluorescent product can be selected to permit excitation of both at the same wavelength ($\lambda_{Ac} = \lambda_{Ex}$) as well as to ensure a significant overlap between the absorption spectrum of the former and the emission spectrum of the latter. Under these conditions, irradiation would excite the reactant to generate the product first and then excite the product to sensitize the excitation of another reactant, establishing an autocatalytic loop. Indeed, either the resonant transfer of the excitation energy of the product to a proximal reactant or the reabsorption of its fluorescence by a distal reactant would translate into sensitization. These operating principles are reminiscent of the energy cascades governing quantum amplification in certain photochemical processes.[218-239] In such chain reactions, the excitation of the reactant eventually generates the product in an excited state. The resulting species can then transfer energy to another reactant molecule, ensuring the propagation of the chain reaction, and decay to the ground state. The overall result is that the absorption of a single photon by the reactant can produce multiple copies of the product, leading to

quantum amplification. In these processes, however, the product sensitizes its own formation prior to populating its ground state and, therefore, the concentration of its ground state has no influence on the rate of the overall transformation. According to our design logic, instead, the product is formed in the ground state first and then it is excited directly to sensitize its own formation. Thus, while the absorption of multiple photons is still required to form multiple copies of the product, the increasing concentration of the latter in the ground state, during the course of the reaction, can accelerate the photochemical conversion and lead to autocatalysis. Furthermore, such a mechanism for the realization of a photochemical replicator could be accelerated even further with the aid of plasmonic effects.[240] In fact, the enhancement of the electromagnetic field in close proximity to the surface of illuminated metallic nanostructures can increase the efficiencies of photochemical reactions[241] and photophysical processes.[242] Therefore, the conversion of reactant into product and the emission of the latter could both be promoted with metallic nanostructures to boost the overall autocatalytic process.

The introduction of an α-diketone bridge across positions 9 and 10 of anthracene isolates electronically the two peripheral phenylene rings of the oligoacene platform.[243] The absorption spectrum of the resulting adduct shows a broad and weak band in the visible region for a $n \rightarrow \pi^*$ transition of the α-diketone chromophore.[169] Illumination at wavelengths within this band results in the cleavage of the α-diketone bridge with the release of two molecules of carbon monoxide and the regeneration of anthracene.[171] In fact, the photoinduced cleavage of similar α-diketone adducts has been employed already to prepare photochemically several oligoacenes[244] and, in a few instances, to activate fluorescence.[63-65] Furthermore, these photochemical reactions can be performed efficiently

within rigid matrices to avoid the dimerization and oxidation of the resulting oligoacenes that often accompany these transformations in solution and, hence, permit the isolation of otherwise elusive polycyclic aromatic hydrocarbons.[170,172,175,245] These literature precedents suggest that an anthracene derivative, capable of emitting in the same spectral region where the α-diketone bridge absorbs, should sensitize its own formation from the corresponding adduct upon excitation. On the basis of such considerations, we designed an α-diketone adduct able to satisfy these stringent spectral requirements as well as identified a control system with minimal spectral overlap instead. In this article, we report the synthesis of the former compound, the structural characterization of both adducts together with the investigation of their photochemical and photophysical properties and the influence of silver nanoparticles on the behavior of the former species.

3.2. Results and discussion

3.2.1. Design, synthesis and structural characterization

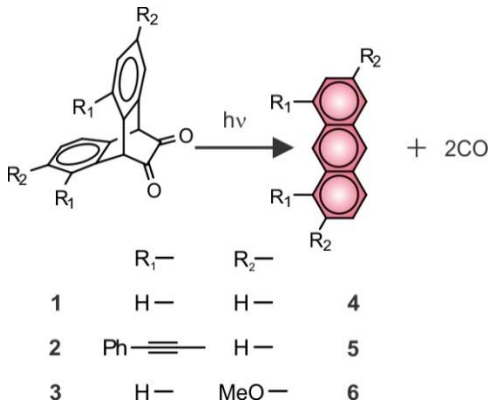

Figure 3.1 Photoinduced decarbonylation of **1**, **2** and **3** to produce **4**, **5** and **6** respectively.

Adducts **1, 2** and **3** differ in the nature of R group (R_1 and R_2 in Figure 3.1) on their two *ortho*-phenylene rings and, upon illumination, are supposed to generate **4**, **5** and **6** respectively. These particular groups are expected to have a negligible influence on the $n \rightarrow \pi^*$ absorption of the α-diketone bridge of **1, 2** and **3**, but a pronounced effect on the

emission of **4, 5** and **6**, hence, on the spectral overlap between reactant and product of the two photochemical reactions.

Adduct **1** can be prepared from **4** in three synthetic steps, following a literature protocol.[246] The very same protocol can be adapted to convert **5** and **6** into **2** and **3** respectively (Figure 3.2). Specifically, Diels Alder reaction of **5** with vinylene carbonate results in the bridging of positions 9 and 10 of the anthracene core with the formation of adduct **7** which after hydrolysis in presence of potassium hydroxide result in formation of **9**. Further, oxidation of diol **9** with trifluoroacetic anhdydride and di-iso-propylethylamine in a mixture of dimethyl sulfoxide (DMSO) and dichloromethane afforded **2.** The overall yield for the three consecutive synthetic steps is 26%. Moreover, using similar oxidation method as mentioned above, known precursor **10** can also be converted into a photocleavable α-diketone in the shape of **3** in a yield of 30%.[198]

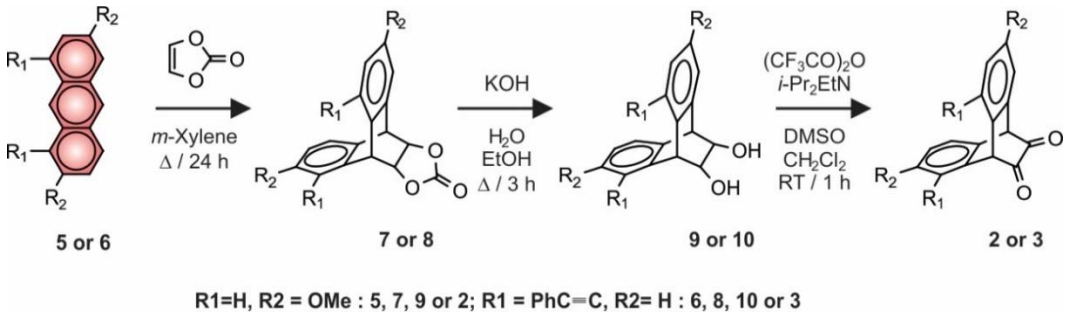

Figure 3.2 Three-step synthesis of **2** and **3** from **5** and **6** respectively.

The structural identities of **2**, **3**, **8** and **10** were confirmed by electrospray ionization mass spectrometry (ESIMS) together with ^{1}H and ^{13}C nuclear magnetic resonance (NMR) spectroscopies. In addition, single crystals of **1**, **2** and **3** suitable for X-ray diffraction analysis (Table 3.2 in experimental section) were obtained after diffusion of hexane vapors into benzene solutions of the compounds. The resulting structures (Figure 3.3) clearly

reveal that the α-diketone bridge, between positions 9 and 10, forces the three fused rings out of planarity and interrupts electronic conjugation across them.

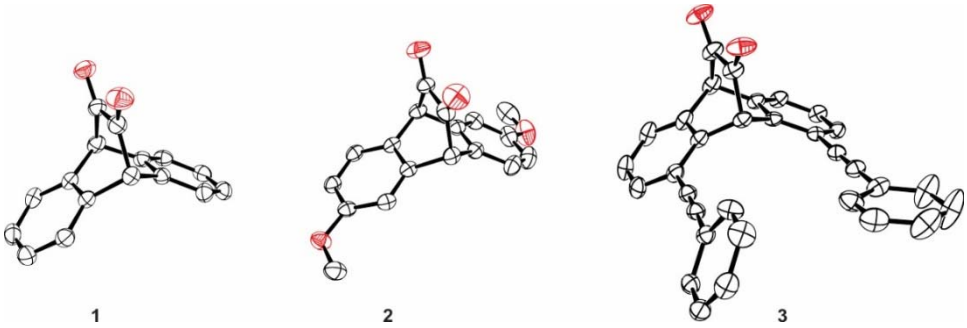

Figure 3.3 ORTEP representations of the crystal structures of **1**, **2** and **3** (30, 30 and 50% thermal ellipsoid probability respectively).

3.2.2. Photochemical and photophysical properties

The absorption spectra of **1, 2** and **3** (***a***, ***b*** and ***c*** in Figure 3.4) reveal a broad and weak band centered at 462 nm (λ_{Ab} in Table 3.1) for a $n \rightarrow \pi^*$ transition of the α-diketone bridge. Upon visible illumination, the characteristic vibronic structure of the corresponding anthracene chromophores appear between 300 and 450 nm (***d***, ***e*** and ***f*** in Figure 3.4). These absorptions are identical to those observed in the spectra of **4**, **5** and **6** (***m***, ***n*** and ***o*** respectively in Figure 3.5) and demonstrate that the α-diketone bridge of **1**, **2** and **3** cleaves under irradiation to restore the anthracene chromophore, in agreement with literature precedents.[63-65,169-172,174,175,243-245] Similar changes are also evident in the corresponding emission spectra (***g*** $\rightarrow$ ***j***, ***h*** $\rightarrow$ ***k*** and ***i*** $\rightarrow$ ***l*** in Figure 3.4). Intense bands appear between 350 and 600 nm (λ_{Em} in Table 3.1) only after visible illumination of the sample. Once again, the photogenerated bands are identical to those observed in the conversion of nonemissive reactants **1, 2** and **3** into emissive products **4, 5** and **6** respectively translates into efficient fluorescence activation.

The photoinduced conversion of **1, 2** and **3** into **4, 5** and **6** respectively occurs in poly(butyl methacrylate) (PBMA) matrix as well as in acetonitrile solution with essentially identical spectral changes (Figures 3.4 and 3.6). The polymer matrix, however, is relatively rigid and prevents the diffusion of the entrapped species. Fluorescence images (***a*** and ***b*** in Figure 3.7) of a polymer film doped with **2** reveal significant emission only after visible illumination. Specifically, the irradiation of a circular area at the center of the imaging field with a laser operating at 458 nm switches **2** to **5** exclusively in the illuminated area with the concomitant appearance of intense fluorescence. The very same fluorescent spot is also evident in an image (***c*** in Figure 3.7) recorded after as many as 10 min, confirming the lack of any significant diffusion.

Table 3.1 Photochemical and photophysical parameters

	λ_{Ab} [a] (nm)	λ_{Em} [a] (nm)	ϕ_A [b]	ϕ_F [c]	J [d] (10^{-16} M^{-1} cm^3)	R_0 [d] (Å)	E [e] (%)
1 → **4**	462	381, 403, 421, 445	0.20	0.27	8.3	18	0.3
2 → **5**	462	430, 454, 479	0.51	0.85	22.4	26	25.8
3 → **6**	461	456	0.12	0.43	34.7	25	10.0

[a] Wavelengths at the absorption (λ_{Ab}) and emission (λ_{Em}) maxima of reactant and product respectively in PBMA at 25 °C. [b] The activation quantum yield (ϕ_A) is the quantum yield for the photochemical conversion of reactant into product. This parameter was determined by illuminating aerated MeCN solutions of the reactant within the chamber of a photoreactor (420 nm) and monitoring periodically the formation of the product by absorption spectroscopy. The irradiation power per unit area (2.3 mW cm^{-2}) was measured with a potassium ferrioxalate actinometer and this value was used to estimate ϕ_A from the corresponding absorbance evolution during photolysis, according to an established procedure (ref.[190]). The error in the determination of ϕ_A is *ca.* 15 %. [c] Literature values for the fluorescence quantum yield (ϕ_F) of the product in aerated MeCN at 25 °C (ref. [66]). [d] Overlap integral (J) and Förster distance (R_0) estimated from the spectra recorded in aerated MeCN at 25 °C. [e] Efficiency (E) of energy transfer from product to reactant estimated from the value of R_0 and the average distance between molecules in PBMA at a concentration of 8% w/w relative to the polymer.

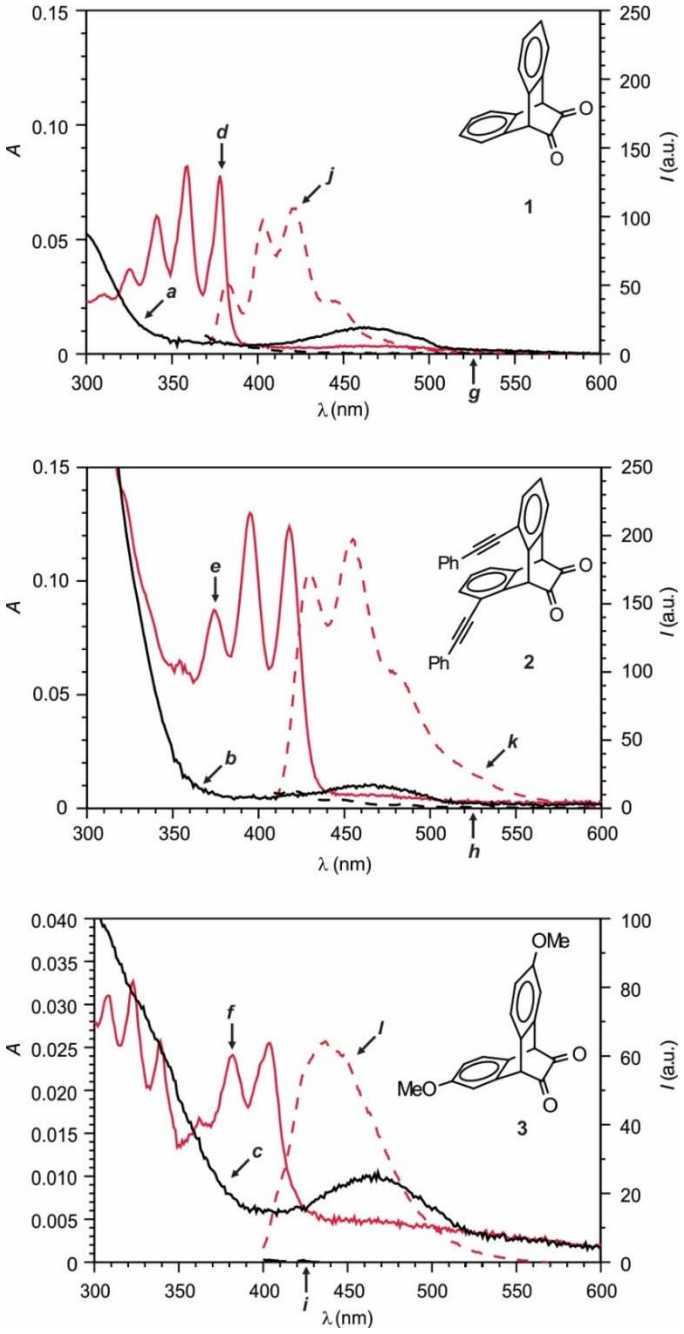

Figure 3.4 Absorption (***a***–***f***) and emission (***g***–***l***) spectra of PBMA films, doped (8% w/w) with **1** (λ_{Ex} = 350 nm) or **2** (λ_{Ex} = 390 nm) or **3** (λ_{Ex} = 380 nm) and spin coated on quartz slides, before (***a***, ***b***, ***c***, ***g***, ***h*** and ***i***) and after (***d***, ***e***, ***f***, ***j***, ***k*** and ***l***) irradiation (420 nm, 2.3 mW cm^{-2}, 300 s for **1**, 60 s for **2** and 120 s for **3**).

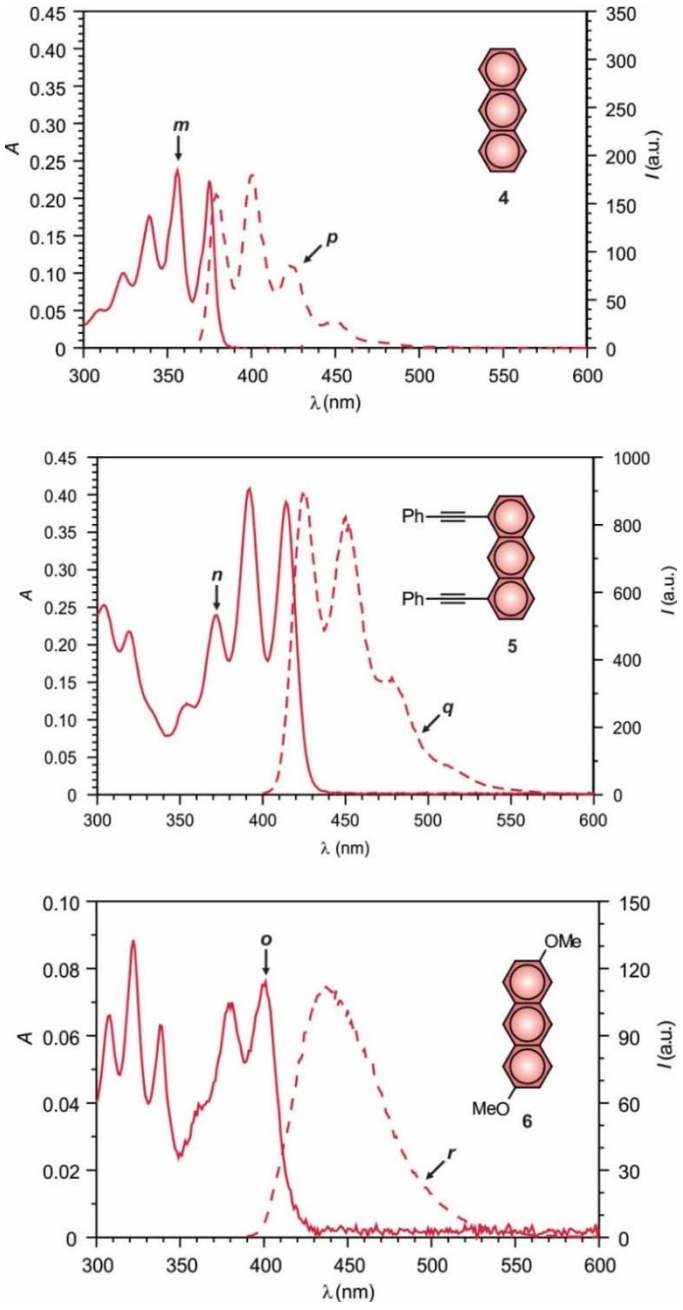

Figure 3.5 Absorption (***m*-*o***) and emission (***p*-*q***) spectra of **4** (30 μM, λ_{Ex} = 350 nm), **5** (20 μM, λ_{Ex} = 390 nm) and **6** (20 μM, λ_{Ex} = 380 nm) in MeCN at 25 °C.

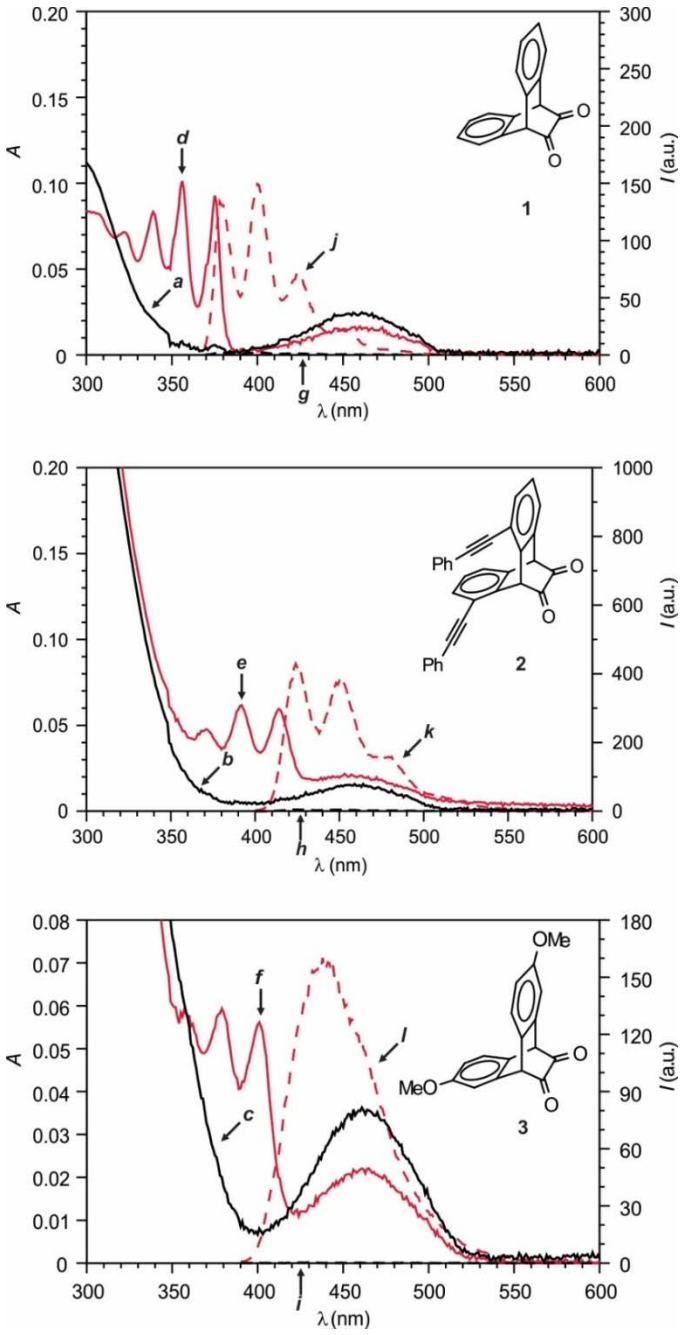

Figure 3.6 Absorption (***a***–***f***) and emission (***g***–***l***) spectra of **1** (30 μM, λ_{Ex} = 350 nm), **2** (20 μM, λ_{Ex} = 390 nm) or **3** (30 μM, λ_{Ex} = 380 nm) in MeCN at 25 °C before (***a***, ***b***, ***c***, ***g***, ***h*** and ***i***) and after (***d***, ***e***, ***f***, ***j***, ***k*** and ***l***) irradiation (420 nm, 2.3 mW cm^{-2}, 300 s for **1**, 60 s for **2** and 360 s for **3**).

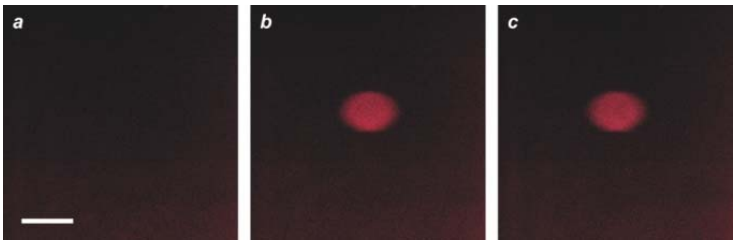

Figure 3.7 Confocal laser-scanning fluorescence images (λ_{Ex} = 405 nm , λ_{Em} = 465–600 nm, scale bar = 200 μm) of a glass slide, coated with a PBMA film doped with **2** (2% w/w), before (***a***), immediately (***b***) and 10 min (***c***) after illumination at 458 nm of a circular area within the imaging field.

The inability of reactant and product to diffuse within the polymer matrix offers the opportunity to induce and probe the transformation of one into the other in a portion of the film with the sole aid of the excitation source of an emission spectrometer. In particular, the sequential acquisition of emission spectra (Figure 3.8) of a PBMA film doped with **2** shows the gradual growth of the characteristic bands of **5**. These spectra were recorded under excitation at a wavelength (390 nm) that matches the $0 \rightarrow 2$ absorption band (***e*** in Figure 3.4) of the photogenerated anthracene chromophore. At this wavelength, the absorbance of **2** (***b*** in Figure 4) is relatively small, yet it is sufficient to initiate the photochemical generation of **5**. Once formed, **5** can absorb part of the incoming photons and emit as a result. In turn, its emission can induce the conversion of another molecule of **2** into a new molecule of **5** and establish an autocatalytic loop. Indeed, a plot (***a*** in Figure 3.9) of the emission intensity, detected at 453 nm in the sequence of spectra, shows the sigmoidal temporal dependence typical of autocatalysis.[205] The reaction accelerates significantly with an increase in the product concentration. By contrast, the same experiment performed with **1** does not reveal any change in fluorescence over the same

temporal scale (***b*** in Figure 3.9).[vi] Indeed, comparison of the emission spectra of **4** and **5** (***j*** and ***k*** in Figure 3.4) reveals optimal spectral overlap with the α-diketone absorption of the corresponding adduct (***a*** and ***b*** in Figure 3.4) only for the latter. In particular, the overlap integral (*J* in Table 4.1) for the **2**/**5** pair is 22.4 10^{-16} M^{-1} cm^{-1}, while it is only 8.3 10^{-16} M^{-1} cm^{-1} for the **1**/**4** counterpart. These values correspond to Förster distances (R_0 in Table 4.1) of 26 and 18 Å respectively and energy-transfer efficiencies (*E* in Table 4.1) of 25.8 and 0.3% respectively at a dopant concentration of 8% w/w relative to the polymer.[vii] Thus, only one of the two photochemical products can transfer efficiently its excitation energy to the corresponding reactant and sensitize its own formation in full agreement with the pronounced difference between the photokinetic profiles of the two reactions (***a*** and ***b*** in Figure 3.9).[viii]

[vi] Only one of the two anthracene chromophores absorbs at 390 nm. Instead, both compounds have similar molar absorption coefficients at 350 nm. As a result, the behavior of the two diketones under illumination was compared using the latter wavelength (***a*** and ***b*** in Figure 3.9). Under these conditions, the spectral changes observed for **2** are similar to those detected with an illumination wavelength of 390 nm (Figure 3.8).

[vii] The average distance between the many molecules immobilized within the rigid polymer matrix is 32 Å at this particular dopant loading. This distance value was estimated from the molar concentration of the reactant (**1** or **2**) in PBMA. The latter parameter was determined from the corresponding absorbance at 462 nm (***a*** and ***b*** in Figure 3.4), the molar absorption coefficient determined in MeCN (***a*** and ***b*** in Figure 3.6) and the film thickness (2.5 μm) measured with a surface profilometer.

[viii] A literature precedent (ref.(239) Nielsen, A.; Kuzmanich, G.; Garcia-Garibay, M. A. *J. Phys. Chem. A*, **2014**, 118, 1858.) demonstrates that Dexter energy transfer governs the cascade responsible for quantum amplification in the photoinduced decarbonylation of a diarylcyclopropanone. In principle, such a mechanism could also contribute to the ability of **5** to sensitize its own formation from **2**. Considering the exponential dependence of Dexter energy transfer on the donor–acceptor separation, however, its efficiency should be negligible at the relatively long distance (32 Å) between **2** and **5** ensured by the selected experimental conditions.

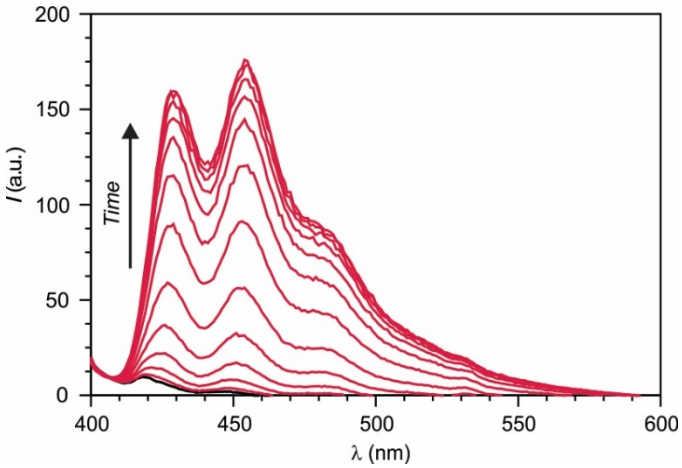

Figure 3.8 Emission spectra (λ_{Ex} = 390 nm) of a PBMA film, doped with **2** (8% w/w) and spin coated on a quartz slide, recorded consecutively over the course of 3000 s (scan rate = 10 nm s^{-1}) at 25 °C.

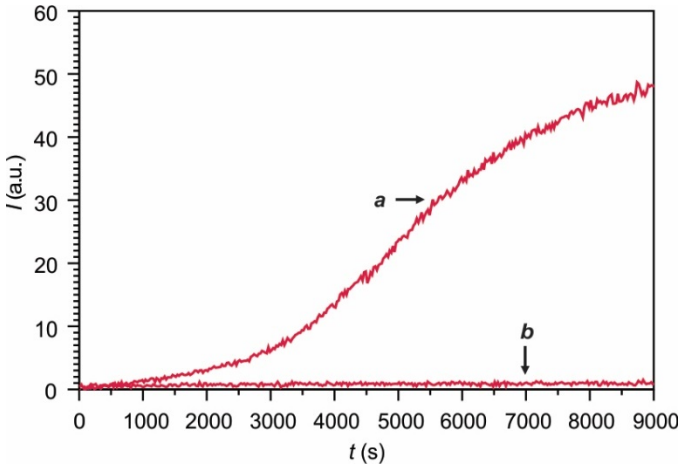

Figure 3.9 Evolution of the emission intensity (λ_{Ex} = 350 nm) of PBMA films, doped (8% w/w) with **2** (***a***, λ_{Em} = 453 nm) or **1** (***b***, λ_{Em} = 400 nm) and spin coated on quartz slides, during the sequential acquisition of spectra over the course of 9000 s (scan rate = 10 nm s^{-1}) at 25 °C.

Alternatively, autocatalytic behavior can also be obtained with the modification of substitution pattern on the anthracene chromophore to satisfy the spectroscopic requirements necessary to enable energy transfer from product to reactant. Specifically, the sequential acquisition of emission spectra (Figure 3.10) under illumination with 380 nm of a PBMA film doped with **3** also shows the gradual growth of the characteristic bands of **6**. In fact, the temporal evolution (***b*** in Figure 3.17) of the emission intensity, under these

illumination conditions, clearly shows once again the sigmoidal dependence characteristic of autocatalysis.

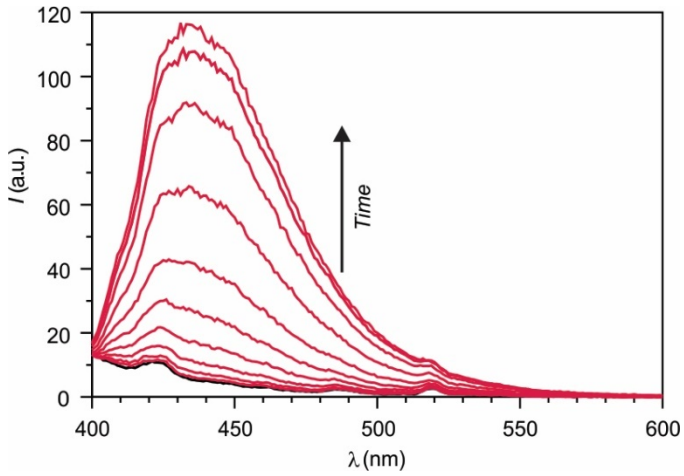

Figure 3.10 Emission spectra (λ_{Ex} = 380 nm) of a PBMA film, doped with **3** (8% w/w) and spin coated on a quartz slide, recorded consecutively over the course of 7000 s (scan rate = 10 nm s^{-1}) at 25 °C.

The role of resonant energy transfers in imposing the sigmoidal profile on the photoinduced conversion of **2** into **5** is further confirmed by the effect of dilution on the reaction course.[ix] Specifically, a tenfold dilution of the sample increases the time required to convert 50% of the reactant from 1450 to 3200 s (***a*** and ***b*** in Figure 3.11). Indeed, the average distance between molecules elongates sufficiently with dilution to lower the energy-transfer efficiency to only 0.01%. Consistently, fittings of the corresponding sigmoidal plots indicate a 35-fold decrease in the quantum yield for the sensitized formation of **5**, under illumination at 390 nm, with dilution.[x]

[ix] In principle, **2** can reabsorb part of the photons emitted by **5** and undergo decarbonylation as a result. However, the contribution of this radiative process, if at all occurring, to the sensitized formation of **5** is most likely negligible under the conditions selected for these experiments. Indeed, the absorbance of the $n \rightarrow \pi^*$ band of **2** is less than 0.01 in all instances and such small values ensure insignificant reabsorption

[x] The mathematical model employed to fit the photokinetic profiles is reported in the experimental section.

In these experiments, the irradiation wavelength of 390 nm is essentially both λ_{Ac} as well as λ_{Ex}. The initial activation of the reactant and the subsequent excitation of the product are both a consequence of absorption at this particular wavelength, which happens to fall within the spectral range associated with the surface-plasmon band of silver nanoparticles (Figure 3.12).[247] As a result of the local enhancement in electromagnetic field,[240-242] these metallic nanostructures can therefore promote the transformation of **2** into **5** in their proximity, under such illumination conditions. Indeed, the sequential acquisition of emission spectra (Figure 3.13) of a PBMA film, doped with **2** and spin coated on silver nanoparticles deposited on a quartz slide, reveals the developing bands of **5** with, yet again, a sigmoidal temporal dependence (***c*** in Figure 3.11) of the emission intensity. However, the time required to convert 50% of the reactant is only 550 s in the presence of the silver nanoparticles, while it is 1450 s in their absence. Fittings of the corresponding sigmoidal plots (Figure 3.14) indicate a 1.6-fold increase in the quantum yield for the sensitized formation of **5** under the influence of the metallic nanostructures.

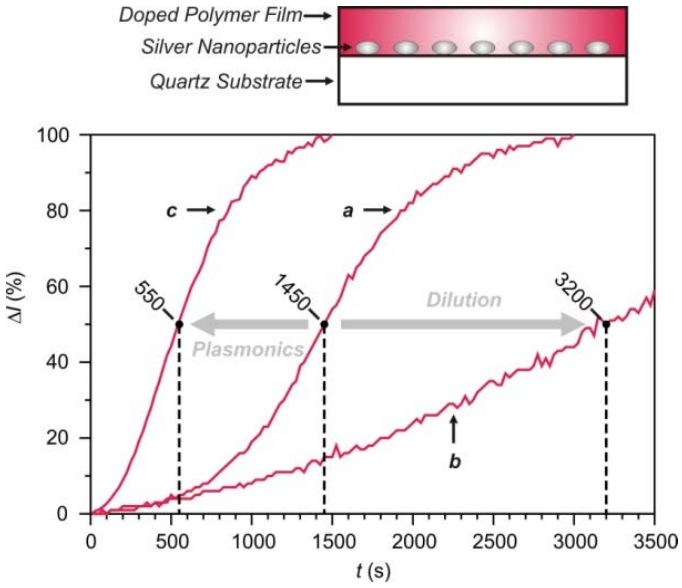

Figure 3.11 Evolution of the emission intensity (λ_{Ex} = 390 nm, λ_{Em} = 453 nm) of PBMA films, doped with **2** at a concentration of 8 (***a***) or 0.8% w/w (***b***), relative to the polymer, in the absence of silver nanoparticles or at a concentration of 8% w/w (***c***) in their presence and spin coated on quartz slides, during the sequential acquisition of spectra over the course of 3000 s (scan rate = 10 nm s^{-1}) at 25 °C.

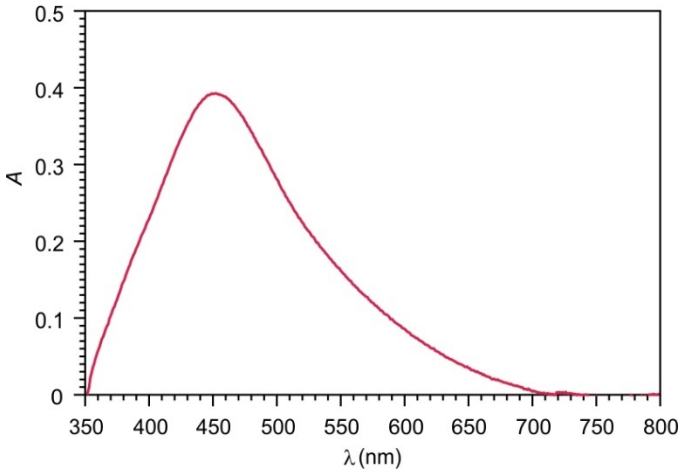

Figure 3.12 Absorption spectrum of a PBMA film doped with **2** (8% w/w) and spin coated on silver nanoparticles deposited on a quartz slide recorded at 25 °C.

The effect of the nanoparticles on the photoinduced conversion of **2** into **5** can be a result of their ability to facilitate the direct excitation of the reactant and the conversion of the resulting excited state into the product. Alternatively, the nanostructures can promote the excitation of the product, enhance its emission and, hence, encourage sensitization.

Comparison of the emission spectra (***a*** and ***b*** in Figure 3.15) of **5**, recorded without and with silver nanoparticles, suggests that the latter mechanism is mostly responsible for accelerating the autocatalytic process. Indeed, the fluorescence of **5** increases significantly in the presence of the nanoparticles. Specifically, the ratio between the integrated emission intensities measured with the nanoparticles and that recorded without is 2.7. Such an enhancement in the fluorescence of **5** elongates the Förster distance to 31 Å and increases the energy transfer to 48%. Interestingly, the ratio between the energy transfer efficiencies, estimated with and without the silver nanoparticles, is 1.8. This value is remarkably close to the enhancement (*cf.*, 1.6) in photoactivation efficiency determined from the sigmoidal plots. Thus, the role of the metallic nanostructures in accelerating the autocatalytic conversion of **2** into **5** appears to be predominantly a consequence of their ability to promote energy transfer from the product to the reactant.

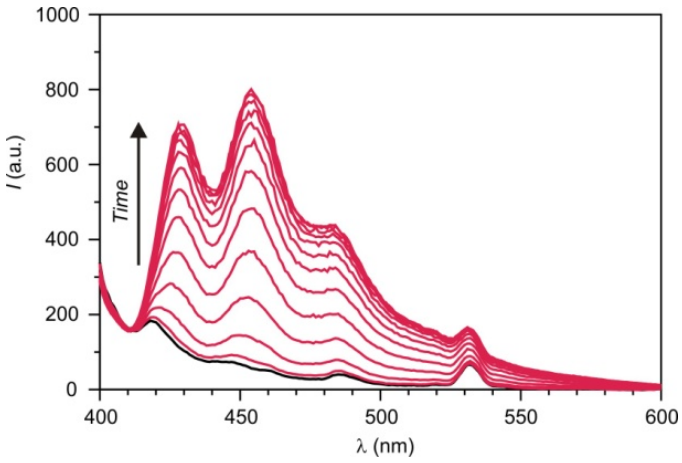

Figure 3.13 Emission spectra (λ_{Ex} = 390 nm) of a PBMA film, doped with **2** (8% w/w) and spin coated on silver nanoparticles deposited on a quartz slide, recorded consecutively over the course of 3000 s (scan rate = 10 nm s^{-1}) at 25 °C.

The role of silver nanoparticle to enhance the photochemical reaction can also be demonstrated when compound **3** was doped in PBMA film on silver nanoparticles and

illuminated at wavelength of 380 nm. Specifically, sequential acquisition of emission spectra (Figure 3.16) recorded in presence of nanoparticles, also show the developing fluorescence of **6** with sigmoidal temporal dependence (***a*** in Figure 3.17). The time (t_{50} in Table 3.1) required to convert 50% of the reactant into the product, however, decreases from 4782 to 2057 s with or without nanoparticles. Furthermore, fittings of the two plots indicate that the apparent activation quantum yield in the presence of the nanoparticle is 1.8 times greater than that in their absence. Thus, the metallic nanostructures enhance the efficiency of the photochemical conversion of **3** into **6** and accelerate significantly the autocatalytic loop as a result.

The influence of the nanoparticles on the photochemical transformation can be a consequence of their ability to promote the absorption of activating photons by **3** and facilitate the population of the excited electronic state responsible for the direct formation of **6**. Alternatively, the nanoparticles can promote the absorption of exciting photons by **6** and facilitate the population of the excited electronic state responsible for sensitization. Comparison of the emission spectra (***a*** and ***b*** in Figure 3.18) of **6** in PBMA without and with silver nanoparticles suggests that the latter mechanism is causing the observed plasmonic acceleration of the autocatalytic loop. Indeed, the emission intensity in the presence of the nanoparticles is 1.8 times greater than that recorded in their absence. Such an enhancement is identical to that observed for the apparent activation quantum yield and, in fact, it translates into the elongation of R_0 to 28 Å with an increase in E to 16%. Thus, the effect of the metallic nanoparticles on the reaction progress demonstrates, once again, that autocatalysis is a consequence of resonant energy transfer. Furthermore, it also

indicates that plasmonic effects can be a valuable tool to accelerate this particular mechanism for photochemical replication.

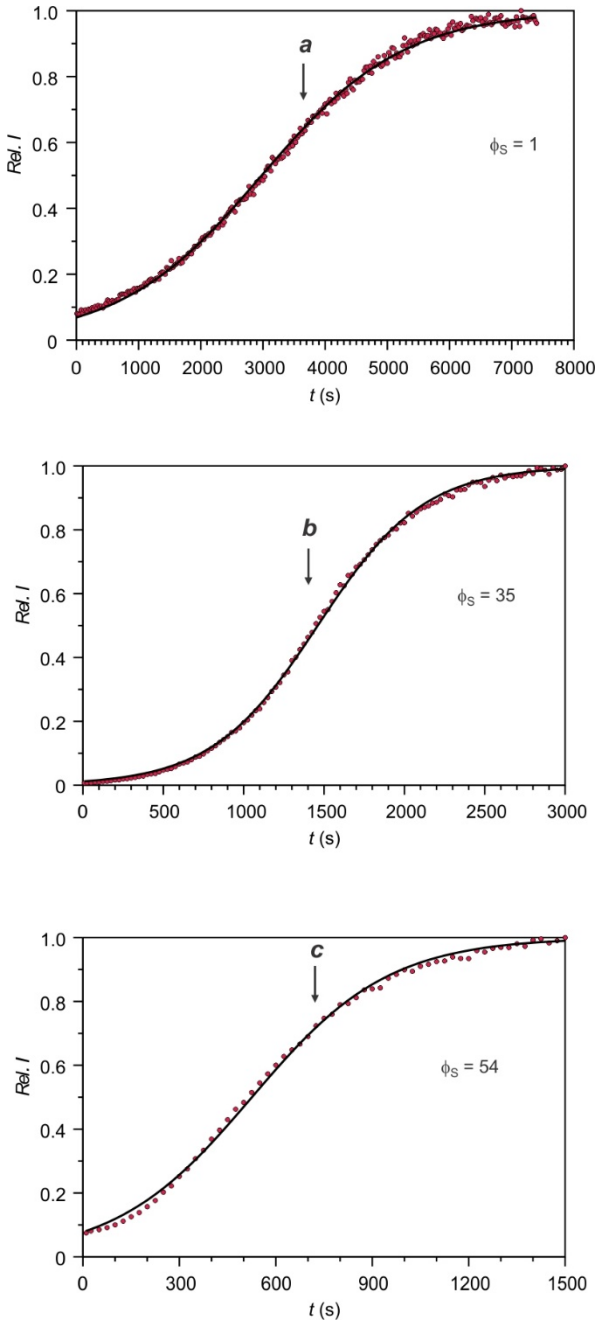

Figure 3.14 Fitting (C.O.D. = 0.999) of the evolution of the relative emission intensity (λ_{Em} = 453 nm) of a PBMA film, doped with **2** (***a***, 0.8% w/w or ***b***, 8% w/w or ***c***, 8% w/w) and spin coated on a quartz slide (***a***, ***b***) and spin coated on silver nanoparticles deposited on a quartz slide (***c***), during the sequential acquisition of spectra (λ_{Ex} = 390 nm) over the course of ***a***, 8000 s, ***b*** 3000 s and ***c*** 1500 s (scan rate = 10 nm s^{-1}) at 25 °C.

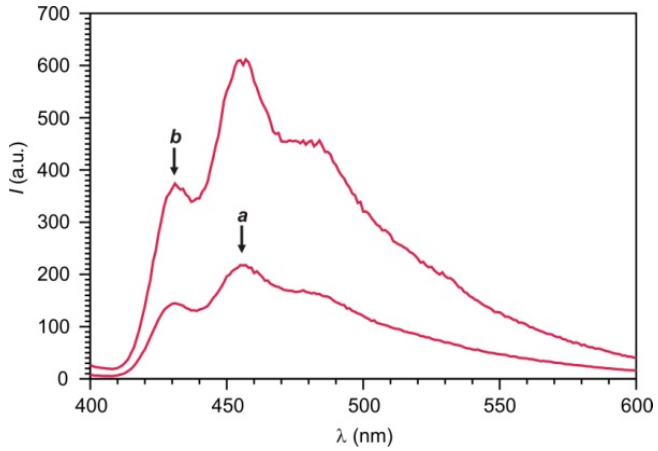

Figure 3.15 Emission spectra (λ_{Ex} = 390 nm) of PBMA films doped with **5** (8% w/w) and spin coated on quartz slides without (***a***) or with (***b***) silver nanoparticles on their surface at 25 °C.

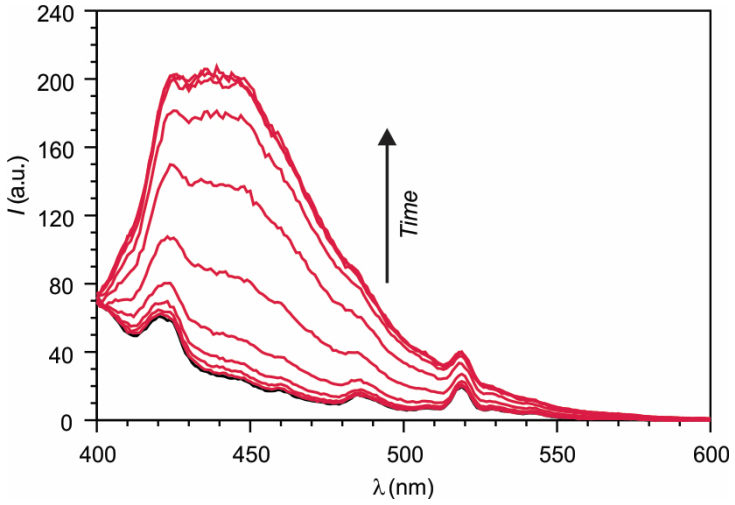

Figure 3.16 Emission spectra (λ_{Ex} = 380 nm) of a PBMA film, doped with **3** (8% w/w, 25 °C) and spin coated on silver nanoparticles deposited on a quartz slide, recorded consecutively over the course of 5000 s (scan rate = 10 nm s^{-1}).

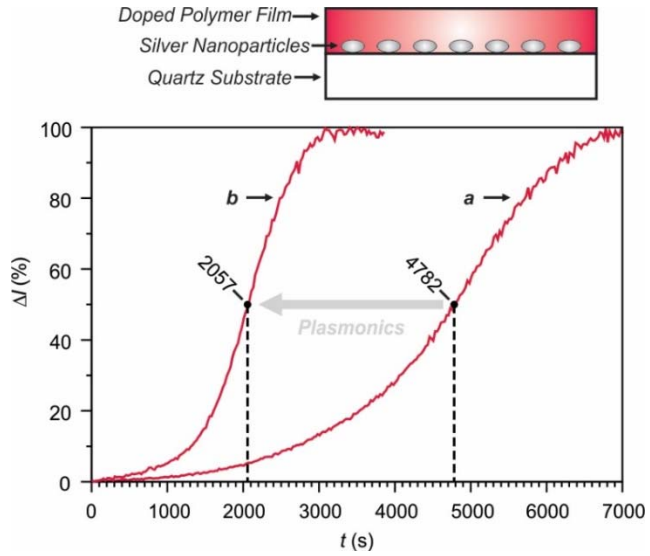

Figure 3.17 Evolution of the emission intensity of PBMA films, doped with **3** (8% w/w, λ_{Ex} = 380 nm, λ_{Em} = 456 nm) in the absence (***a***) and presence (***b***) of silver nanoparticles and spin coated on quartz slides, during the sequential acquisition of spectra over the course of 7000 s (scan rate = 10 nm s^{-1}) at 25 °C.

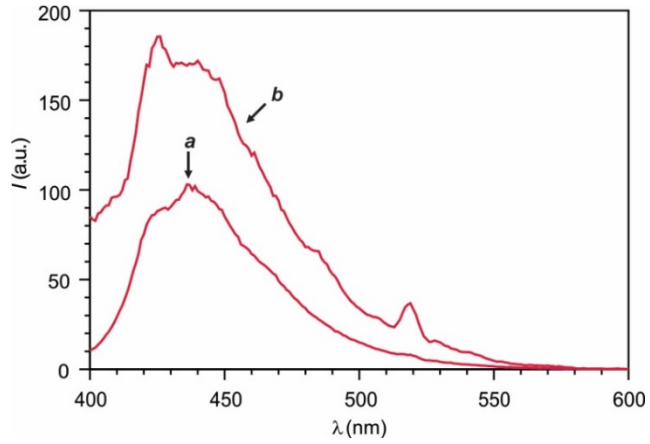

Figure 3.18 Emission spectra (λ_{Ex} = 380 nm) of PBMA films doped with **6** (8% w/w) and spin coated on quartz slides without (***a***) or with (***b***) silver nanoparticles on their surface at 25 °C

3.3. Conclusions

Photochemical autocatalysis can be implemented on the basis of fluorescence activation. The fluorescent product of such a photochemical transformation must be designed to emit in the same range of wavelengths where the nonemissive reactant absorbs. If both species can be excited at the same wavelength and if they are maintained in close proximity, then

resonant energy transfer from the product to the reactant can sensitize the formation of the latter from the former to establish an autocatalytic loop. Furthermore, the local enhancement in electromagnetic field, associated with the illumination of metallic nanoparticles, can be exploited to enhance the energy-transfer efficiency and accelerate the overall photochemical transformation. Ultimately, such operating principles for autocatalysis with plasmonic boost translate into fluorescence amplification. Thus, our representative example of photochemical autocatalysis might eventually evolve into a general design logic for the realization of plasmonic systems capable of signal amplification.

3.4. Experimental section

3.4.1. Materials and methods

Chemicals were purchased from commercial sources and used as received with the exception of CH_2Cl_2 and MeCN, which were distilled over CaH_2, and H_2O, which was purified with a Barnstead International NANOpure DIamond Analytical system. Compounds **1**, **5** and **9** were prepared according to literature procedures.[197,246,248] EISMS was performed with a Bruker micrOTO-Q II spectrometer. NMR spectra were recorded with a Bruker Avance 400 spectrometer. Absorption and emission spectra were recorded with Varian Cary 100 Bio and Varian Cary Eclipse spectrometers respectively. Measurements were performed either in aerated MeCN solutions, using quartz cells with a path length of 1.0 cm, or in PBMA matrices, using quartz slides mounted on custom-built sample holders. The values of ϕ_F listed in Table 1 are literature data.[66] Those of ϕ_A listed in the same table are the quantum yields for the photochemical conversions of **1** into **4, 2** into **5** and of **3** into **6** in aerated acetonitrile at 25 °C. The values of ϕ_A were determined

by monitoring the evolving absorbance of the photochemical product under illumination at 420 nm, using a potassium ferrioxalate actinometer to measure the irradiation power per unit area (2.3 mW cm^{-2}) with an established procedure.[190] Samples were illuminated with a Luzchem Research LZC-4V photoreactor (420 nm, 2.3 mW cm^{-2}) for the experiments in Figures 3.4 and 3.6 and with the excitation source (350, 380 or 390 nm) of the emission spectrometer for the experiments in Figures 3.9, 3.11 and 3.17. A Chemat Technologies KW-4A spin coater was used to prepare the polymer films. A Tencor Instruments 10-00090 surface profilometer was used to measure the thickness of the polymer films. Fluorescence images were recorded with a Leica SP5 confocal laser-scanning microscope. **2**: Trifluoroacetic anhydride (1 mL, 7.0 mmol) was added dropwise over 10 min to a mixture of dry DMSO (1 mL) and CH_2Cl_2 (4 mL) maintained at –60 °C under Ar. The resulting solution was stirred under these conditions for a further 10 min and then a solution of **6** (180 mg, 0.4 mmol) in a mixture of dry DMSO (1 mL) and dry CH_2Cl_2 (2 mL) was added dropwise over 10 min. The resulting solution was stirred for a further 60 min under the same conditions and then *i*-Pr_2EtN (2.7 mL, 16 mmol) was added dropwise over 5 min. The resulting solution was stirred for a further 60 min and then it was allowed to warm up to ambient temperature. After dilution with CH_2Cl_2 (50 mL), the mixture was washed with aqueous HCl (1M, 20 mL), H_2O (20 mL) and brine (20 mL). The organic layer was dried over Na_2SO_4 and then the solvent was distilled off under reduced pressure. The residue was purified by column chromatography [SiO_2: AcOEt/hexanes (2:3, v/v)] to give **2** (90 mg, 50%) as a yellow solid. ESIMS: $m/z = 457.1202$ $[M + Na]^+$ (m/z calcd. for $C_{32}H_{18}O_2Na$ =457.1204); ^1H NMR ($CDCl_3$): δ = 5.04 (1H, s), 6.22 (1H, s), 7.14–7.19 (4H, m), 7.29–7.34 (2H, m), 7.37–7.40 (2H, m), 7.43–7.48 (6H, m), 7.59–7.61 (2H, d, 8 Hz); ^{13}C NMR

($CDCl_3$): δ = 56.4, 60.4, 85.7, 95.0, 122.5, 122.7, 126.4, 128.8, 129.1, 129.6, 132.3, 133.1, 135.8, 136.3, 183.0, 184.0.

3: Trifluoroacetic anhydride (1 mL, 7.0 mmol) was added dropwise over 10 min to a mixture of dry DMSO (1 mL) and CH_2Cl_2 (4 mL) maintained at –60 °C under Ar. The resulting solution was stirred under these conditions for a further 10 min and then a solution of **3** (130 mg, 0.4 mmol) in a mixture of dry DMSO (1 mL) and dry CH_2Cl_2 (2 mL) was added dropwise over 10 min. The resulting solution was stirred for a further 60 min under the same conditions and then *i*-Pr_2EtN (2.7 mL, 16 mmol) was added dropwise over 5 min. The resulting solution was stirred for a further 60 min and then it was allowed to warm up to ambient temperature. After dilution with CH_2Cl_2 (50 mL), the mixture was washed with aqueous HCl (1M, 20 mL), H_2O (20 mL) and brine (20 mL). The organic layer was dried over Na_2SO_4 and then the solvent was distilled off under reduced pressure. The residue was purified by column chromatography [SiO_2: AcOEt/hexanes (2:3, v/v)] to give **1** (40 mg, 30%) as a yellow solid. ESIMS: *m/z* = 317.0778 $[M + Na]^+$ (*m/z* calcd. for $C_{18}H_{14}O_4Na$ =317.0790); ^1H NMR ($CDCl_3$): δ = 3.80 (6H, s), 4.97 (2H, s), 6.91–6.98 (2H, m), 7.10–7.13 (2H, m), 7.41–7.47 (2H, m); ^{13}C NMR ($CDCl_3$): δ = 55.4, 58.9, 111.6, 115.0, 126.4, 127.4, 136.7, 160.7, 183.8.

8: A solution of **5** (360 mg, 0.9 mmol) and vinylene carbonate (1 mL, 16 mmol) in *m*-xylene was heated at 180 °C in sealed tube for 24 hours. The reaction mixture was cooled down to ambient temperature and diluted with dry MeOH (50 mL). The resulting precipitate was filtered off, washed with MeOH (100 mL) and dried to give **8** (345 mg, 78%) as a white solid. ESIMS: *m/z* = 487.1294 $[M + Na]^+$ (*m/z* calcd. for $C_{33}H_{20}O_3Na$ = 487.1309); ^1H NMR [$(CD_3)_2CO$]: δ = 5.05 (1H, s), 5.13–5.18 (1H, m), 5.21–5.26 (1H, m),

5.95 (1H, s), 7.21–7.30 (4H, m), 7.31–7.44 (4H, m), 7.46–7.59 (8H, m); ^{13}C NMR ($CDCl_3$): δ = 43.9, 48.5, 76.3, 76.4, 86.2, 86.5, 93.9, 94.3, 121.6, 122.5, 122.9, 123.3, 125.8, 127.0, 127.9, 128.0, 128.7, 128.8, 129.0, 131.7, 131.9, 132.2, 136.9, 137.8, 138.5, 138.9, 154.4.

10: A mixture of **8** (320 mg, 0.7 mmol) and KOH (160 mg, 3 mmol) in H_2O (2 mL) and EtOH (10 mL) was heated at 80 °C for 3 hours. The hot reaction mixture was filtered and the solid residue was purified by column chromatography [SiO_2: AcOEt/hexanes (1:1, v/v)] to give **10** (200 mg, 66%) as a white solid. ESIMS: *m*/*z* = 461.1504 $[M + Na]^+$ (*m/z* calcd. for $C_{32}H_{22}O_2Na$ =461.1517); ^{1}H NMR [$(CD_3)_2CO$]: δ = 4.05 (2H, s), 4.16 (1H, s), 4.42 (1H, s), 4.54 (1H, s), 5.65 (1H, s), 7.16–7.30 (6H, m), 7.32–7.52 (10H, m); ^{13}C NMR [$(CD_3)_2CO$]: δ = 47.7, 52.0, 59.6, 67.0, 67.3, 86.8, 87.5, 91.8, 92.3, 119.4, 121.0, 123.0, 123.4, 125.0, 125.8, 126.5, 126.7, 128.3, 128.5, 128.5, 129.4, 129.8, 131.5, 131.6, 140.3, 141.0, 141.5.

3.4.2. Crystallographic analysis

The data crystals of **1**, **2** and **3** were glued onto the end of a thin glass fiber. X-ray intensity data were measured with a Bruker SMART APEX2 CCD-based diffractometer, using Mo Kα radiation (λ = 0.71073 Å).[249] The raw data frames were integrated with the SAINT+ program by using a narrow-frame integration algorithm. Corrections for Lorentz and polarization effects were also applied with SAINT+. An empirical absorption correction based on the multiple measurement of equivalent reflections was applied using the program SADABS. The structures were solved by a combination of direct methods and difference Fourier syntheses and refined by full-matrix least-squares on F^2 with the SHELXTL software package.[ii] All non-hydrogen atoms were refined with anisotropic displacement parameters. Hydrogen atoms were placed in geometrically-idealized positions and

included as standard riding atoms during the least-squares refinements. Crystal data, data collection parameters and results of the analysis are listed in Table 3.2.

Table 3.2. Crystallographic Data for **1**, **2** and **3**.

	1	**2**	**3**
Empirical Formula	$C_{16}H_{10}O_2$	$C_{32}H_{18}O_2$	$C_{18}H_{14}O_4$
Formula Weight	234.24	434.46	294.29
Crystal System	Monoclinic	Triclinic	Monoclinic
Lattice Parameters:			
a (Å)	8.6876(4)	10.4626(5)	15.6333(10)
b (Å)	14.2494(7)	12.8543(6)	11.0103(7)
c (Å)	9.2839(5)	18.3722(10)	8.6779(6)
α (°)	90	101.6020(1)	
β (°)	97.417(1)	95.8970(1)	100.578(1)
γ (°)	90	106.6660(1)	
V (Å^3)	1139.67(10)	2284.6(2)	1468.32(17)
Space Group	$P2_1/c$ (# 14)	$P\bar{1}$ (# 2)	$P2_1/c$ (# 14)
Z Value	4	4	4
ρ_{calc} (g cm^{-3})	1.365	1.263	1.331
μ (Mo Kα) (mm^{-1})	0.090	0.078	0.094
T (K)	296	296	296
$2\Theta_{max}$ (°)	54.0	50.0	50.0
No. Obs. ($I > 2\sigma(I)$)	2114	6460	2106
No. Parameters	164	613	201
Goodness of Fit	1.030	1.024	1.084
Max. Shift in Cycle	0.001	0.001	0.000
*Residuals**: R1; wR2	0.0386; 0.0917	0.0467; 0.1170	0.0585; 0.1289;
Absorption Correction, Max/min	Multi-Scan 0.9911 / 0.9549	Multi-Scan 0.9953 / 0.9636	Multi-Scan 0.9962 / 0.9597
Largest Peak in Final Diff. Map (e$^-$ Å^{-3})	0.154	0.419	0.154

* $R = \Sigma_{hkl}(||F_{obs}|-|F_{calc}||)/\Sigma_{hkl}|F_{obs}|$; $R_w = [\Sigma_{hkl}w(|F_{obs}|-|F_{calc}|)^2/\Sigma_{hkl}wF_{obs}^2]^{1/2}$, $w = 1/\sigma^2(F_{obs})$; $GOF = [\Sigma_{hkl}w(|F_{obs}|-|F_{calc}|)^2/(n_{data} - n_{vari})]^{1/2}$.

Yellow single crystals were obtained after diffusion of hexane vapors into benzene solutions of **1, 2** and **3**. Compound **1** and **3** crystallized in the monoclinic crystal system. The systematic absences in the intensity data identified the unique space group $P2_1/c$. Compound **2** crystallized in the triclinic crystal system, and the space group $P\bar{1}$ was assumed and confirmed by the successful refinement of the structure. Two molecules are present in the asymmetric crystal unit.

3.4.3. Synthesis of silver nanoparticles

Aqueous NaOH (1.2 M, 0.1 mL) was added to aqueous $AgNO_3$ (0.22 g, 26 mL) under vigorous stirring. A dark-brown precipitate formed immediately. Aqueous NH_4OH (7.3 M, 1 mL) was added dropwise to dissolve the precipitate. The resulting clear solution was cooled down to 5 °C. Quartz slides were submerged in the cooled solution and aqueous D-glucose (0.35 g, 4 mL) was added. The mixture was stirred for 2 min at 5 °C, allowed to warm up to ambient temperature, heated to 40 °C and stirred for a further 10 min at this temperature. In the process, the yellow-green solution turned brown and a greenish coating deposited on the slides. The slides were removed from the solution, washed with H_2O, sonicated in H_2O for 1 min at ambient temperature, washed again with H_2O, dried in air for 2 hours and coated with the polymer films.

3.4.4. Preparation of polymer films

A solution of PBMA ($M_W = 337 \times 10^3$) and either **1** or **2** or **3** (0.8, 2 or 8% w/w for **1** or **2** and 2 or 8% for **3** relative to PBMA) was deposited dropwise on either a glass or a quartz slide. The substrate was spun at 1000 rpm for 20 s and then again at 1000 rpm for a further 60 s. The coated slides were stored under reduced pressure for 6 hours prior to any imaging

(glass) and spectroscopic (quartz) experiments. The same protocol was employed to deposit polymer films on quartz slides pre-coated with silver nanoparticles.

3.4.5. Kinetic model

The autocatalytic transformation of **2** into **4** demands the initial absorption of one activating photon by the reactant (*R*) with the formation of one molecule of the product (*P*). Once formed, *P* can absorb a second photon at the same wavelength, transfer energy to another molecule of *R* and sensitize the formation of a second molecule of *P*. If the molar absorption coefficient of *R* is negligible relative to that of *P*,[xi] then the sensitized formation of *P* dominates the progress of the overall transformation after the initial activation.[xii] Under these conditions, the temporal evolution of the concentration of *P* can be modeled with equation (1),[250] where [*P*] and [*R*] are the concentrations of the species, I_P is the number of photons absorbed by *P* per unit time and ϕ_S is the quantum yield for the sensitized formation of *P*.

$$\frac{d[P]}{dt} = I_P \, \phi_S \, [R] \tag{3.1}$$

At the low absorbance values of the photochemical experiment,[xiii] I_P can be estimated with equation (3.2),[251] where I_0 is the number of incident photons per unit time, ε_P is the molar absorption coefficient of *P* and *d* is the path length.

$$I_P = 2.302 \, I_0 \, \varepsilon_P \, d \, [P] \tag{3.2}$$

[xi] The molar absorption coefficient of **2** at 390 nm is two orders of magnitude smaller than that of **5** (b and e in Figure 3.4).

[xii] The lack of any significant conversion of 1 into 4 (b in Figure 3.9) confirms that the influence of direct activation on the temporal evolution the overall photochemical transformation is negligible.

[xiii] The absorbance at 390 nm remains smaller than 0.1 at any point in time during the photoinduced transformation of 2 into 5.

If [*R*] is converted exclusively into [*P*], then the sum of their concentrations at any point in time during the photochemical transformation will be equal to the initial concentration (*c*) of *R* according to equation (3.3).

$$c = [R] + [P] \tag{3.3}$$

The combination of equations (3.1), (3.2) and (3.3) and the rearrangement of the resulting expression gives equation (3.4), where the parameter χ is constant and is defined by equation (3.5).

$$\frac{d[P]}{dt} = \chi\, c\, [P] - \chi\, [P]^2 \tag{3.4}$$

$$\chi = 2.302\, I_0\, \varepsilon_P\, d\, \phi_S \tag{3.5}$$

Integration of equation (3.4) gives equation (3.6),[250] where *Z* is the ratio between the concentrations of reactant and product immediately after activation.

$$[P] = \frac{c}{1 + Z\, e^{-c\, \chi\, t}} \tag{3.6}$$

The ratio (*Rel.* I_{Em}) between the emission intensity measured at any point in time during the photochemical transformation and that determined after the quantitative conversion of *R* into *P* is equal to the ratio between [*P*] and *c*.[251] As a result, equation (3.6) can be rearranged into equation (3.7):

$$Rel.\, I_{Em} = \frac{1}{1 + Z\, e^{-c\, \chi\, t}} \tag{3.7}$$

Fittings (Figure 3.14) of the three sigmoidal plots illustrated in Figure 3.11 to equation (3.7) provide estimates of *Z* and of the product between *c* and χ for the three experiments. The ratios between the fitted values of this product are equivalent to the ratios between the corresponding ϕ_S, according to equation (3.5) and knowing that I_0, ε_P and *d* are identical in all instances and that *c* is equal in two experiments but diluted ten times in the other. The resulting values of ϕ_S are reported in Figure 3.14 relative to the smallest one of the three.

CHAPTER 4

ENERGY-TRANSFER SCHEMES TO PROBE FLUORESCENT NANOCARRIERS AND THEIR EMISSIVE CARGO

4.1. Background

The entrapment of hydrophobic fluorophores within micelles of amphiphilic polymers[90-102,104-106,108-110] permits the convenient visualization of these supramolecular constructs with the aid of conventional fluorescence microscopes and, possibly, even their localization in the intracellular space.[252] However, the noncovalent interactions responsible for maintaining the emissive guests inside their nanostructured hosts, as well as for holding the supramolecular containers together, are reversible. Under certain experimental conditions, these micelles can dissociate into their constituent components. In turn, the separation of the emissive species from the amphiphilic macromolecules prevents the identification of the latter with fluorescence measurements. As a result, the localization of the actual polymer components, after cellular internalization, is generally unclear because they cannot be detected directly. Thus, the identification of strategies to monitor independently nanocarriers and their cargo with fluorescence measurements would be particularly valuable to elucidate the intracellular behavior of these promising supramolecular systems.

Energy-transfer schemes can be designed to probe the stability of micellar aggregates of amphiphilic polymers as well as to investigate their ability to exchange their constituent components.[111,253-268] Specifically, donors and acceptors can be co-encapsulated in the interior of the same nanocarriers to allow the transfer of energy from the former chromophores to latter upon excitation. Experimental conditions that encourage the dissociation of the supramolecular constructs into their individual components, however,

can separate the donors from the acceptors and suppress energy transfer. Therefore, measurements of the energy-transfer efficiency can provide a quantitative indication of the environmental influence on the integrity of such supramolecular assemblies in a diversity of media. Similar measurements can also establish if distinct nanocarriers can exchange their cargo, when combined within the same aqueous phase. In fact, the mixing of two sets of micelles, loaded with donors and acceptors respectively, can result in the redistribution of the chromophoric guests within their supramolecular hosts. This dynamic process can eventually lead to the co-encapsulation of donors and acceptors within the same nanostructured containers and enable energy transfer.

Strategies to investigate micellar aggregates on the basis of energy transfer are generally based on the noncovalent encapsulation of the chromophoric units within the hydrophobic interior of the supramolecular constructs.[111,253-268] Under these conditions, measurements of the donor and/or acceptor fluorescence provide information on the relative location of the complementary chromophoric guests. However, the actual supramolecular hosts and their individual amphiphilic components cannot be probed directly with these methods, simply because they are generally not emissive. In principle, this limitation could be overcome with the covalent attachment of at least one of the two complementary chromophores to the macromolecular backbone of the amphiphilic synthons. Indeed, the noncovalent encapsulation of donors within micelles connected covalently to acceptors, or *vice versa*, would offer the opportunity to assess the relative location of supramolecular hosts and molecular guests. Such a strategy would be particularly valuable to probe simultaneously nanocarriers and their cargo after cellular internalization. Similarly, the covalent attachment of donors and acceptors to distinct amphiphilic polymer and then the

co-assembly of the resulting macromolecules into the same micelles would permit the direct assessment of the stability of such supramolecular constructs and enable the direct visualization of the individual polymer components in the intracellular environment. On the basis of these considerations, we designed amphiphilic polymers with decyl and oligo(ethylene glycol) side chains as well as either anthracene donors or borondipyrromethene (BODIPY) acceptors along a poly(methacrylate) backbone. In this thesis, we report their synthesis and structural characterization, together with a detailed spectroscopic characterization of their photophysical properties and the investigation of their ability to transport guests inside living cells.

4.2. Results and discussion

4.2.1. Noncovalent encapsulation of fluorescent chromophores within supramolecular nanocarriers

Compounds **1** and **2** absorb and emit in the visible region of the electromagnetic spectrum.[269,270] The characteristic bands (***a***–***d*** in Figure 4.1) of their anthracene and BODIPY chromophores, however, can be detected in phosphate buffer saline (PBS) only in the presence of **3**. This particular amphiphilic polymer has a number average molecular weight ($\bar{M}_n$ in Table 4.1) of 14.7 kDa and a ratio (*m*:*n* in Figure 4.1) between its hydrophobic and hydrophilic side chains of 1:1.[xiv] At concentrations greater than a critical micellar concentration (CMC in Table 4.1, Figure 4.2) of 29 μg mL^{-1} in PBS, an average of 3.9 macromolecules of **3** assemble into individual particles with hydrodynamic diameter

[xiv] The values of $\bar{M}_n$ (Table 4.1) and *m*:*n* (Figure 4.1) were determined by gel permeation chromatography (GPC) and ^{1}H nuclear magnetic resonance (NMR) spectroscopy respectively. The latter parameter was estimated from the integrals of the resonances associated with the methyl protons at the termini of the hydrophobic and hydrophilic chains.

of 11 nm (d_H in Table 4.1).[xv] In the process of self-assembling, these supramolecular constructs can capture either **1** or **2** in their hydrophobic interior, transfer the otherwise insoluble chromophores into the aqueous phase and allow their spectroscopic detection. The resulting absorption and emission spectra are essentially identical to those (λ_{Ab} and λ_{Em} in Table 4.2, Figure 4.3) recorded without the polymer in tetrahydrofuran (THF), indicating that the environment surrounding the encapsulated guests is similar to that experienced by both chromophores in this particular organic solvent. Nonetheless, the fluorescence quantum yield decreases with encapsulation from 0.86 to 0.68 for **1** and from 0.92 to 0.56 for **2** at a guest loading of 0.4% w/w (ϕ in Table 4.2). This particular loading corresponds to an average of 0.6 chromophores per micelle. Presumably, some of the supramolecular hosts encapsulate more than one guest and interchromophoric interactions in their interior can facilitate the nonradiative deactivation of the excited fluorophores with a concomitant depressive effect on the fluorescence quantum yield detected for the overall ensemble of micelles.

[xv] The values of d_H (Table 4.1) and the average "supramolecular" weight (w_S) of the micelles were determined by dynamic light scattering (DLS) and static light scattering (SLS) respectively. The latter parameter is 57.4, 70.4 and 64.5 kDa for **3**, **4** and **5** respectively. Considering that these polymers have a $\overline{M}_n$ of 14.7, 14.3 and 15.9 kDa respectively (Table 4.1), an average of 3.9, 4.9 and 4.0 polymer chains must be assembling together into individual micelles.

Table 4.1 Number average molecular weight ($\bar{M}_n$), dispersity index (***Đ***), critical micellar concentration (CMC) and hydrodynamic diameter ($\boldsymbol{D}_h$) of **3**, **4** and **5** in neutral PBS at 25 °C.

	$\bar{M}_n$ (kDa)	*Đ*	CMC (μg mL^{-1})	d_H (nm)
3	14.7	1.20	29	11
4	14.3	1.68	19	12
5	15.9	1.65	13	13

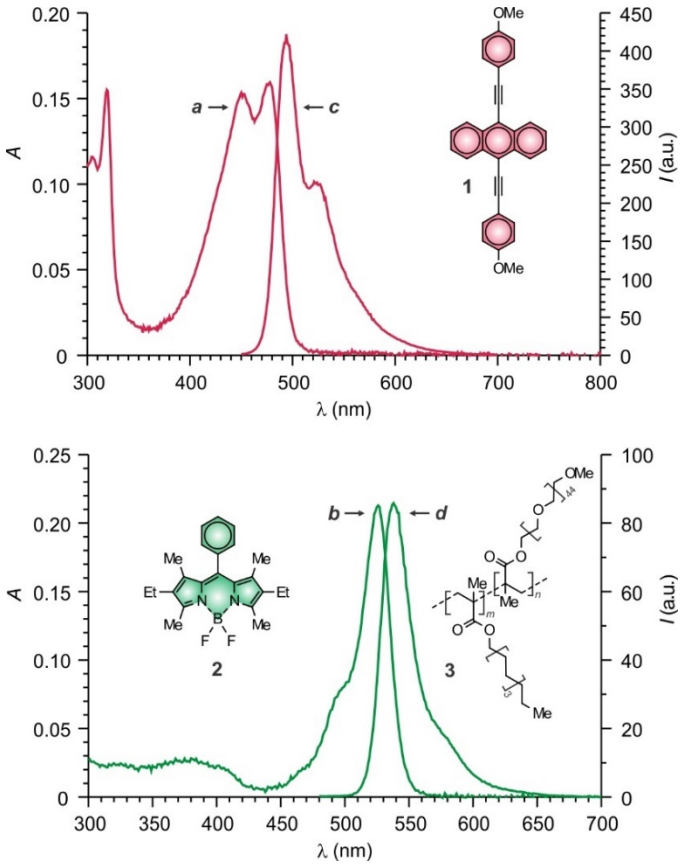

Figure 4.1 Absorption (***a*** and ***b***) and emission (***c*** and ***d***) spectra of **3** (500 μg mL^{-1}) and either **1** (***a*** and ***c***, 2 μg mL^{-1}, λ_{Ex} = 440 nm) or **2** (***b*** and ***d***, 2 μg mL^{-1}, λ_{Ex} = 470 nm) in PBS (pH = 7.0, 25 °C).

Table 4.2 Absorption (λ_{Ab}) and emission (λ_{Em}) wavelengths and fluorescence quantum yields of **1**, **2**, **4** and **5** at 25 °C [*a*].

	λ_{Ab} (nm)		λ_{Em} (nm)		ϕ	
	THF	PBS	THF	PBS	THF	PBS
1	471	478	488	494	0.86	0.68
2	524	526	535	538	0.92	0.41
4	445	445	484	492	0.66	0.36
5	526	529	542	548	0.22	0.19

[*a*] The data listed for **1** and **2** in PBS were determined in the presence of **3** at a guest loading of 0.4% w/w.

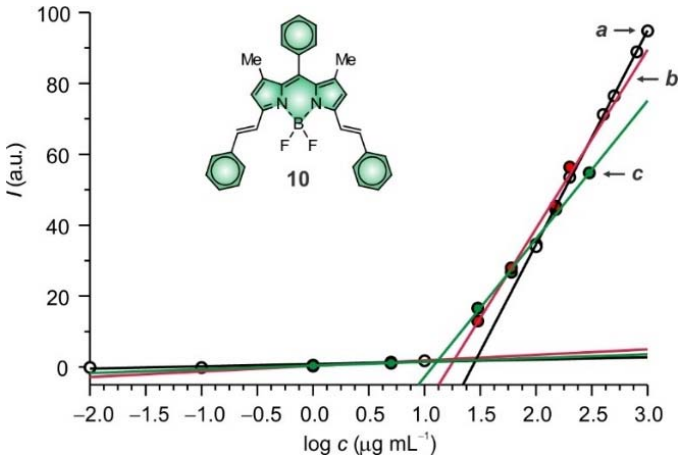

Figure 4.2 Plots of the emission intensity of **10** (0.25 μg mL^{-1}, λ_{Ex} = 580 nm, λ_{Em} = 640 nm) against the concentration of **3** (***a***), **4** (***b***) or **5** (***c***) in PBS at 25 °C.

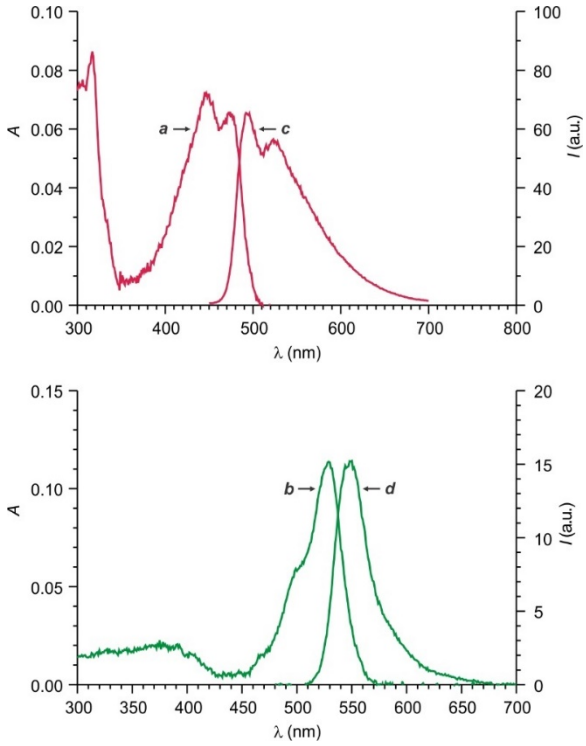

Figure 4.3 Absorption (***a***–***d***) and emission (***e***–***h***) spectra of **1** (***a*** and ***e***, 2 μM, λ_{Ex} = 440 nm) or **2** (***c*** and ***g***, 1 μM, λ_{Ex} = 470 nm) in THF and of **3** (500 μg mL^{-1}) and either **1** (***b*** and ***f***, 2 μg mL^{-1}, λ_{Ex} = 440 nm) or **2** (***d*** and ***h***, 2 μg mL^{-1}, λ_{Ex} = 470 nm) in PBS (pH = 7.0, 25 °C).

4.2.2. Covalent attachment of fluorescent chromophores to amphiphilic polymers

The chromophoric guests encapsulated within micellar assemblies of **3** are maintained inside their supramolecular hosts solely on the basis of noncovalent interactions. Alternatively, fluorescent groups can be attached covalently to the polymer components of the nanostructured constructs. Specifically, **4** and **5** (Figure 4.4) incorporate anthracene and BODIPY chromophores respectively within their covalent skeleton, in addition to the very same hydrophobic and hydrophilic chains of **3**. These fluorescent and amphiphilic polymers can be prepared by reacting either **6** or **7** with appropriate amounts of **8** and **9**, under the influence of azobis(*i*-butyronitrile) (AIBN), to ensure a *m*:*n* value of 1:1 in the final macromolecular assembly. In analogy to **3**, also **4** and **5** form particles with hydrodynamic diameters of 12 and 13 nm respectively in PBS (*cf.* 11 nm for **3**, Table 4.1).

[xv] However, the critical micellar concentrations of **4** and **5** required to encourage the assembly of micelles are 19 and 13 μg mL^{-1} respectively (Table 4.1, Figure 4.2), while it is 29 μg mL^{-1} for **3**. The decrease of this parameter with the covalent attachment of the chromophoric units to the macromolecular backbone is, presumably, a consequence of their hydrophobic character, which can enhance the magnitude of the noncovalent contacts responsible for the association of distinct polymer components into nanostructured particles.

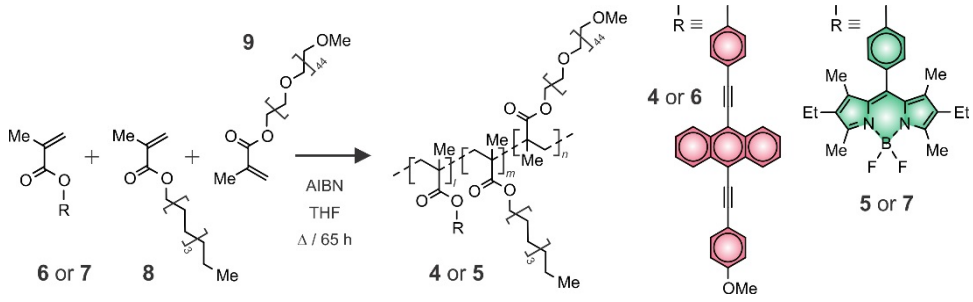

Figure 4.4 Synthesis of amphiphilic polymers **4** and **5**.

The absorption and emission spectra (***a***–***d*** in Figure 4.5) of **4** and **5**, recorded in PBS at concentrations greater than the corresponding critical values required for micelle assembly, show the characteristic bands of their anthracene and BODIPY chromophores respectively. Normalization of these spectra to those determined for **1** and **2** in micelles of **3** reveal differences in the vibronic structure of the anthracene components and in the Stokes shift of the BODIPY fluorophores (λ_{Ab} and λ_{Em} in Table 4.2, Figure 4.6). These minor, but noticeable, changes suggest that covalent attachment and noncovalent encapsulation position the chromophoric units in different environments. Furthermore, comparison of the spectra of **4** and **5** recorded in PBS to those determined in THF shows similar differences (Figure 4.7), while the bands detected for **1** and **2** within micelles of **3** in PBS

are essentially identical to those observed in THF (Figure 4.3). Presumably, the covalently-attached chromophores are partially exposed to the aqueous environment, while the noncovalently-encapsulated counterparts are effectively insulated from the water molecules surrounding their supramolecular containers.

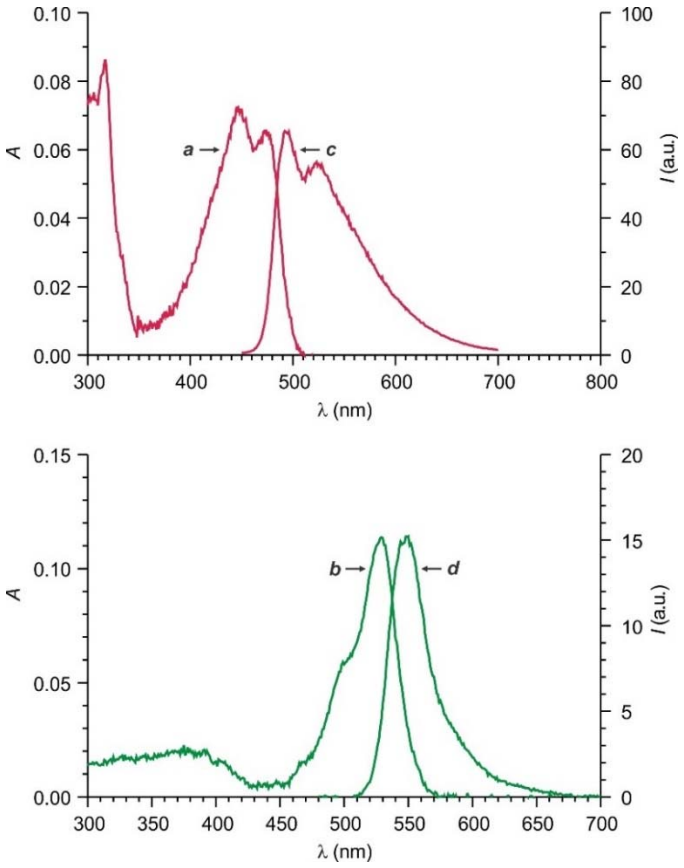

Figure 4.5 Absorption (***a*** and ***b***) and emission (***c*** and ***d***) spectra of **4** (***a*** and ***c***, 30 μg mL^{-1}, λ_{Ex} = 440 nm) and **5** (***b*** and ***d***, 15 μg mL^{-1}, λ_{Ex} = 470 nm) in PBS (pH = 7.0, 25 °C).

Comparison of the absorbance values recorded for **1** and **2** in THF to those determined for **4** and **5** under the same conditions indicates the average number of chromophores covalently-attached to each polymer to be 1.1 and 1.7 respectively. In spite of the relatively low content of chromophoric units, the fluorescence quantum yields of **4** and **5** in THF are 0.66 and 0.22 respectively (ϕ in Table 4.2). Both values are lower than those of **1** and **2** in

the same solvent (*cf.* 0.86 and 0.92 respectively). Thus, the covalent attachment of the fluorescent units to a macromolecular backbone tends to facilitate the nonradiative deactivation of their excited state. Additionally, the fluorescence quantum yields of **4** and **5** decrease even further to 0.36 and 0.19 respectively in PBS at concentrations greater than the corresponding critical values. Under these conditions, an average of 4.9 and 4.0 chains of **4** and **5** respectively assemble into individual micelles [xv] to cluster an average of 5.4 and 6.8 chromophores respectively within each of the resulting supramolecular assemblies. These values are one order of magnitude greater than the number of chromophores noncovalently-encapsulated within each micelle of **3** (*cf.* 0.7 at a guest loading of 0.4% w/w). In fact, the fluorescence quantum yields for the noncovalently-encapsulated fluorophores are significantly greater than those of the covalent counterparts. Presumably, the relatively large chromophoric content of the latter systems tends to encourage interchromophoric interactions in the excited state to promote nonradiative deactivation.

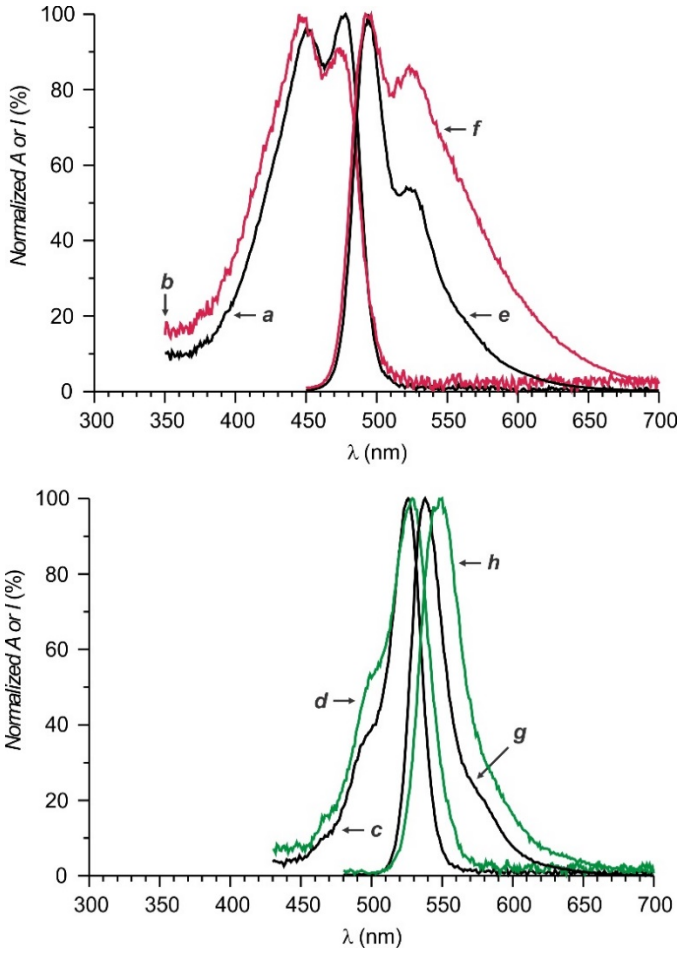

Figure 4.6 Absorption (***a***–***d***) and emission (***e***–***h***) spectra of **3** (500 μg mL^{-1}) and either **1** (***a*** and ***e***, 2 μg mL^{-1}, λ_{Ex} = 440 nm) or **2** (***c*** and ***g***, 2 μg mL^{-1}, λ_{Ex} = 470 nm), of **4** (***b*** and ***f***, 30 μg mL^{-1}, λ_{Ex} = 440 nm) and of **5** (***d*** and ***h***, 15 μg mL^{-1}, λ_{Ex} = 470 nm) in PBS (pH = 7.0, 25 °C).

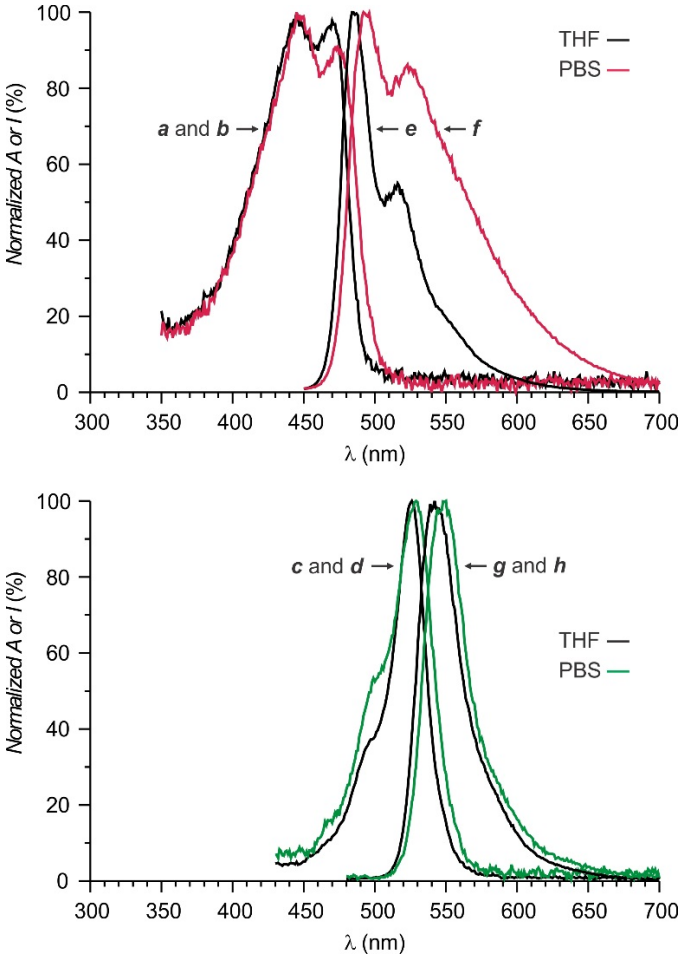

Figure 4.7 Absorption (***a***–***d***) and emission (***e***–***h***) spectra of **4** (***a*** and ***e***, 30 μg mL^{-1}, λ_{Ex} = 440 nm) or **5** (***c*** and ***g***, 15 μg mL^{-1}, λ_{Ex} = 470 nm) in THF and of **4** (***b*** and ***f***, 30 μg mL^{-1}, λ_{Ex} = 440 nm) or **5** (***d*** and ***h***, 15 μg mL^{-1}, λ_{Ex} = 470 nm) in PBS (pH = 7.0, 25 °C).

4.2.3. Energy transfer within supramolecular nanocarriers

The emission of **1** (***c*** in Figure 4.1) is positioned in the same spectral range of the absorption of **2** (***b*** in Figure 4.1). Their overlap integral is 11×10^{-14} M^{-1} cm^3 and corresponds to a Förster distance of 49 Å.[xvi] These values, in conjunction with the physical dimensions of the micelle of **3** (*cf.* d_H in Table 4.1), suggest that the co-encapsulation of **1** and **2** within these supramolecular containers can promote the transfer of excitation energy from the former to the latter.

The emission spectra (***a*** and ***b*** in Figure 4.8) of nanocarriers, containing either **1** or **2**, reveal intense anthracene emission or weak BODIPY fluorescence respectively, upon excitation at 440 nm. Indeed, the absorbance of **1** at this particular wavelength is significant (***a*** in Figure 4.1), while that of **2** is negligible (***b*** in Figure 4.1). Under identical illumination conditions, the emission spectrum (***c*** in Figure 4.8) of micelles, loaded with both chromophores, shows instead modest anthracene emission and intense BODIPY fluorescence. These observations demonstrate that the supramolecular host maintains the co-entrapped guests in close proximity to allow the transfer of excitation energy from the anthracene donors to the BODIPY acceptors. Comparison of the emission intensities of

[xvi] The overlap integral (J) and Förster distance (R_0) were calculated with equations (4.1) and (4.2) respectively (ref.1). The emission intensity (I_D) of the anthracene donor and the molar absorption coefficient (ε_A) of the BODIPY acceptor at a given wavelength (λ) were determined from the corresponding emission and absorption spectra (***c*** and ***b*** in Figure 4.1) respectively. The orientation factor (κ^2), fluorescence quantum yield (ϕ_D) of the donor and refractive index (n) of the solvent are 2/3, 0.68 and 1.33 respectively.

$$J = \frac{\int_0^\infty I_D \, \varepsilon_A \, \lambda^4 \, d\lambda}{\int_0^\infty I_D \, d\lambda} \tag{4.1}$$

$$R_0 = \sqrt[6]{\frac{9000 \, (\ln 10) \, \kappa^2 \, \phi_D \, J}{128 \, \pi^5 N n^4}} \tag{4.2}$$

the donor, measured in the absence and presence of the acceptor, indicates the energy-transfer efficiency to be 0.74.[xvii]

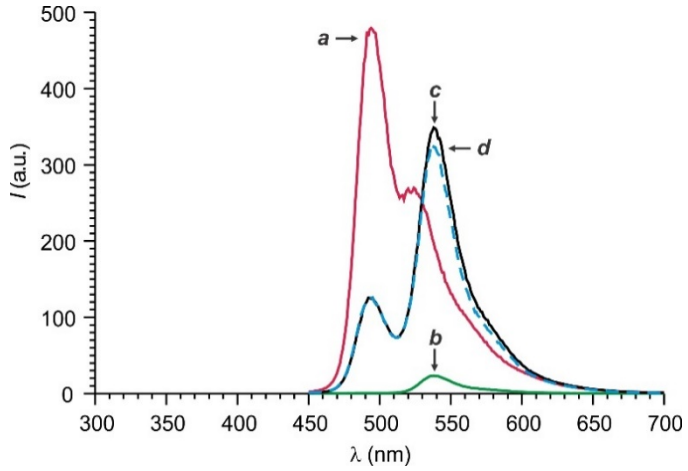

Figure 4.8 Emission spectra (λ_{Ex} = 440 nm) in PBS (pH = 7.0, 25 °C) of **3** (500 μg mL^{-1}) and **1** (***a***, 3 μg mL^{-1}), **2** (***b***, 3 μg mL^{-1}) or both (***c***, 3 μg mL^{-1} each). Emission spectrum (***d***, λ_{Ex} = 440 nm) recorded immediately after mixing identical volumes of two PBS dispersions (pH = 7.0, 25 °C) containing **1** (6 μg mL^{-1}) and **3** (500 μg mL^{-1}) or **2** (6 μg mL^{-1}) and **3** (500 μg mL^{-1}) respectively.

The noncovalent co-encapsulation of donors and acceptors within the supramolecular nanocarriers ensures the short separations that are necessary for the transfer of energy to occur. In principle, such distance requirements can also be satisfied with the covalent attachment of the complementary chromophores to the macromolecular components of the micelles. Specifically, the co-assembly of **4** and **5** within the same supramolecular construct can bring their anthracene and BODIPY appendages in close proximity to allow energy transfer.

[xvii] The energy-transfer efficiency (E) was calculated from the emission intensities of the donor in the absence (I_D) and presence (I_{DA}) of the acceptor with equation (4.3) (ref.1)

$$E = 1 - \frac{I_{DA}}{I_D} \qquad (4.3)$$

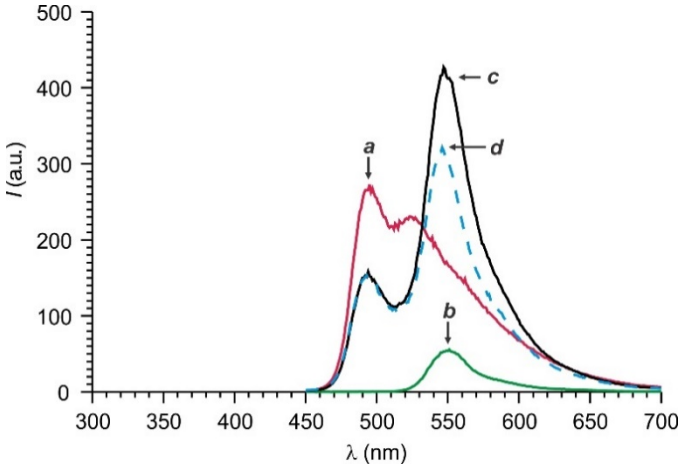

Figure 4.9 Emission spectra (λ_{Ex} = 440 nm) in PBS (pH = 7.0, 25 °C) of **4** (***a***, 300 μg mL^{-1}), **5** (***b***, 300 μg mL^{-1}) and both (***c***, 300 μg mL^{-1} each). Emission spectrum (***d***, λ_{Ex} = 440 nm) recorded immediately after mixing identical volumes of two PBS dispersions containing **4** (600 μg mL^{-1}) or **5** (600 μg mL^{-1}) respectively.

The emission spectra (***a*** and ***b*** in Figure 4.9) of **4** and **5**, dispersed in separate PBS dispersions at concentrations greater than the corresponding critical values, show intense anthracene emission and weak BODIPY fluorescence respectively, upon excitation at 440 nm. Once again, this particular wavelength ensures the effective excitation of the former chromophore with minimal absorption of the latter. By contrast, the emission spectrum (***c*** in Figure 4.9) of a dispersion of both amphiphilic polymers reveals weak anthracene emission but intense BODIPY fluorescence. These observations demonstrate that the two distinct macromolecules are incorporated within the same supramolecular constructs to maintain donors and acceptors at distances compatible with energy transfer. Comparison of the emission intensities of the donor, measured in the absence and presence of the acceptor, indicates the efficiency of energy transfer to be 0.44.[xvii] This value is lower than that recorded for **1** and **2** within micelles of **3** (*cf.* 0.74), in spite of the negligible difference in spectral overlap between the donors and acceptors of both systems as well as in the ratio between the number of donors and that of acceptors, which is close to 1:1 in both

instances.[xviii] Presumably, the relative positions of the chromophores within the supramolecular assemblies differ in the two systems. As a result, covalent attachment and noncovalent encapsulation translate into different donor–acceptor separations and/or orientations of the complementary chromophores.

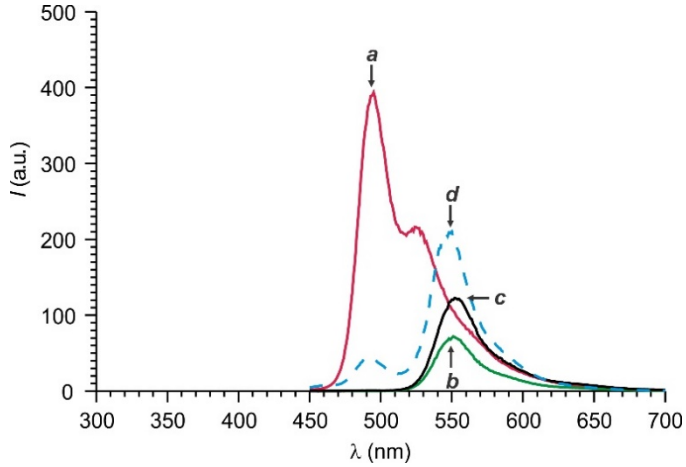

Figure 4.10 Emission spectra (λ_{Ex} = 440 nm) in PBS (pH = 7.0, 25 °C) of **3** (500 μg mL^{-1}) and **1** (***a***, 3 μg mL^{-1}), of **5** (***b***, 300 μg mL^{-1}) or of **1** (3 μg mL^{-1}) and **5** (***c***, 300 μg mL^{-1}). Emission spectrum (***d***, λ_{Ex} = 440 nm) recorded immediately after mixing identical volumes of two PBS dispersions (pH = 7.0, 25 °C) containing **1** (6 μg mL^{-1}) and **3** (1.0 mg mL^{-1}) or **1** (6 μg mL^{-1}) and **5** (600 μg mL^{-1}) respectively.

Analogous energy-transfer processes can be established if one of the two chromophores is covalently attached to the macromolecular components and the other is noncovalently encapsulated within the nanocarriers. In fact, the encapsulation of **1** in micelles of **5** results in the complete suppression of the anthracene emission (Figure 4.10) with a concomitant enhancement in the BODIPY fluorescence, relative to that recorded in the absence of **1** under identical illumination conditions. Similarly, the entrapment of **2** in micelles of **4** also causes a decrease in anthracene emission (Figure 4.11) with an increase in BODIPY

[xviii] The donor/acceptor ratios were estimated from the absorbance values measured at the λ_{Ab} (Table 2) of the corresponding chromophores, using the molar absorption coefficients of **1** and **2** determined in THF.

fluorescence, relative to those detected for micelles of **4** in the absence of **2** and for **2** in nanocarriers of **3** respectively under identical illumination conditions. The experimental implementation of these two systems, however, requires the concentration of the macromolecular component to be greater than the corresponding critical value. As a result, the number of covalently-attached chromophores incorporated in the final supramolecular construct is greater than that of the noncovalently-encapsulated counterparts. Specifically, the ratio between the number of donors and that of acceptors is 1:6 for the combination of **1** and **5** and it is 8:1 for **2** and **4**.[xviii]

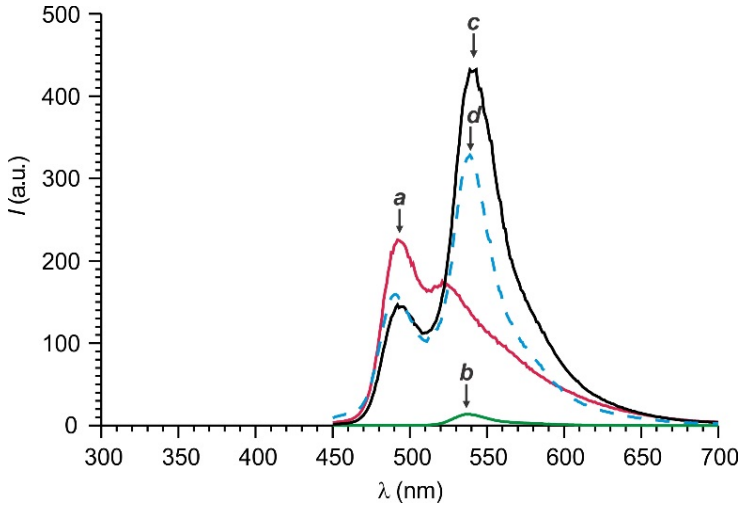

Figure 4.11 Emission spectra (λ_{Ex} = 440 nm) in PBS (pH = 7.0, 25 °C) of **3** (500 μg mL^{-1}) and **2** (***a***, 2 μg mL^{-1}), of **4** (***b***, 300 μg mL^{-1}) or of **2** (2 μg mL^{-1}) and **5** (***c***, 300 μg mL^{-1}). Emission spectrum (***d***, λ_{Ex} = 440 nm) recorded immediately after mixing identical volumes of two PBS dispersions (pH = 7.0, 25 °C) containing **2** (4 μg mL^{-1}) and **3** (1.0 mg mL^{-1}) or **2** (4 μg mL^{-1}) and **4** (600 μg mL^{-1}) respectively.

These four sets of supramolecular constructs were prepared by mixing appropriate amounts of their separate components in chloroform and, after the evaporation of the solvent, dispersing the residues in PBS. This protocol encourages the assembly of the amphiphilic polymers into micelles, upon exposure to the aqueous medium, and the covalent and/or noncovalent integration of anthracene donors and BODIPY acceptors within the very same

supramolecular construct. Essentially the same result is observed if aqueous dispersions of micelles, incorporating exclusively the donors, and constructs, integrating only the acceptors, are prepared individually and then combined in appropriate volumes.[xix] Indeed, the emission spectrum (***d*** in Figure 4.8), recorded after mixing a PBS dispersion of nanocarriers of **3**, containing **1**, and a PBS dispersion of micelles of **3**, incorporating **2**, is almost identical to that (***c*** in Figure 4.8) of the very same supramolecular constructs prepared initially with both chromophores in their interior. These observations indicate that the two sets of micelles exchange their components with fast kinetics, upon mixing, to produce supramolecular assemblies with donors and acceptors in their hydrophobic interior and enable energy transfer.

In principle, this dynamic process can be a consequence of the leakage of the chromophoric guests out of their respective supramolecular hosts and their subsequent capture by different micelles. Nonetheless, the hydrophobic character of **1** and **2** translates into the lack of any significant solubility in the surrounding aqueous phase, discouraging their possible separation from the supramolecular containers. Alternatively, some of the polymer chains can dissociate from one micelle and associate with another, carrying part of the noncovalently-bound chromophores along within their hydrophobic domains. In fact, the latter mechanism would be the only viable one to bring donors and acceptors from separate micelles to the same construct for the two polymers with covalently-connected

---

[xix] The guest loading was 0.4% w/w for the donor as well as for the acceptor in the final dispersion. This value translates into an average number of chromophores per micelle of 0.6 for each one of the two guests. DLS measurements, performed before and after combining the two solutions, indicate that d_H does not change with mixing and is 12 nm in all instances (*cf.* 11 nm for **3** in Table 4.1).

chromophores. In agreement with this interpretation, the combination of a PBS dispersion of **4** with a PBS dispersion of **5** results in the assembly of both within the same supramolecular construct to allow energy transfer.[xx] The corresponding emission spectrum (***d*** in Figure 4.9) shows the decrease in donor fluorescence and enhancement in acceptor emission, relative to the spectra of the separate components (***a*** and ***b*** in Figure 4.9), that is characteristic of energy transfer.[xxi] Thus, this spectral response clearly demonstrates that separate micelles are able to exchange their polymer components with fast kinetics upon mixing.[xxii]

4.2.4. Intracellular transport of complementary donors and acceptors

Incubation of cervical cancer (HeLa) cells with PBS dispersions of micelles of **3**, containing either **1** or **2**, results in the internalization of the nanostructured constructs. Consistently, the corresponding fluorescence images (***a*** in Figures 4.12 and 4.13) show significant emission intensity in the intracellular space. A similar result is also observed if the fluorophores are covalently attached to the amphiphilic polymers, instead of being noncovalently entrapped in the micelles. Once again, fluorescence images (***b*** in Figures 4.12 and 4.13) of cells incubated with either **4** or **5** reveal significant intracellular

---

[xx] DLS measurements, performed after mixing the two dispersions, reveal d_H to be 12 nm (*cf.* 12 and 13 nm for **4** and **5** respectively in Table 4.1).

[xxi] The same behavior is observed if a PBS dispersion of micelles of **3**, containing either **1** or **2**, is mixed with a PBS dispersion of either **5** or **4** respectively (***d*** in Figures 4.10 and 4.11). The guest loading was 0.4% w/w in the final dispersion of each experiment. DLS measurements, performed after mixing the two dispersions, reveal d_H to be 10 or 11 nm respectively (*cf.* 11, 12 and 13 nm for **3**, **4** and **5** respectively in Table 4.1).

[xxii] In principle, energy transfer could also be established after the cleavage of the chromophores from the macromolecular backbone of **4** and/or **5** and their exchange among distinct micelles. Both amphiphilic polymers, however, are stable under the conditions of the exchange experiment. Indeed, thin-layer chromatographic analyses demonstrate that the chromophores do not separate from the polymers, even after maintaining **4** and **5** in PBS at ambient temperature for up to 24 hours.

fluorescence, confirming the internalization of the emissive macromolecules. These images were recorded by exciting either the anthracene chromophores of **1** and **4** at 458 nm and collecting the emission between 470 and 510 nm or the BODIPY chromophores of **2** and **5** at 518 nm and recording their fluorescence between 530 and 560 nm. Alternatively, the two sets of complementary fluorophores can be integrated within the same supramolecular assembly and images can be recorded by exciting the anthracene donors at 458 nm and collecting the emission of the BODIPY acceptors between 530 and 560 nm. Specifically, one of the two chromophores can be attached covalently to the macromolecular components and the other entrapped noncovalently in the resulting micelles. Under these conditions, the acceptor fluorescence can be detected in the intracellular space only if the amphiphilic polymers and hydrophobic guests do not separate in the process of traveling into the intracellular space. Indeed, fluorescence images (***c*** in Figures 4.12 and 4.13) of cells incubated with micelles of either **5**, containing **1**, or **4**, containing **2**, clearly reveal that the excitation of the donors produces intense acceptor fluorescence intracellularly in both instances. Control experiments with the same micelles, in the absence of their guests, confirm the occurrence of energy transfer. In fact, the corresponding images (Figure 4.14) do not reveal any emission, demonstrating that donors and acceptors must both be present to ensure intracellular fluorescence under these illumination conditions. Thus, these observations demonstrate that donors and acceptors are maintained in close proximity and suggest that the nanocarriers and their cargo remain associated.

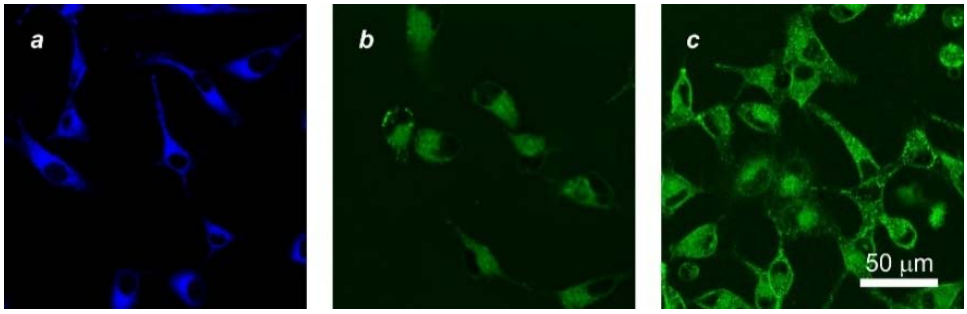

Figure 4.12 Fluorescence images of HeLa cells recorded after incubation with PBS dispersions of micelles of (***a***) **3** (125 μg mL^{-1}), containing **1** (1.25 μg mL^{-1}, λ_{Ex} = 458 nm, λ_{Em} = 470–510 nm), (***b***) **5** (250 μg mL^{-1}, λ_{Ex} = 518 nm, λ_{Em} = 530–560 nm) and (***c***) **5** (250 μg mL^{-1}), containing **1** (2.5 μg mL^{-1}, λ_{Ex} = 458 nm, λ_{Em} = 530–560 nm) for 3 hours and washing.

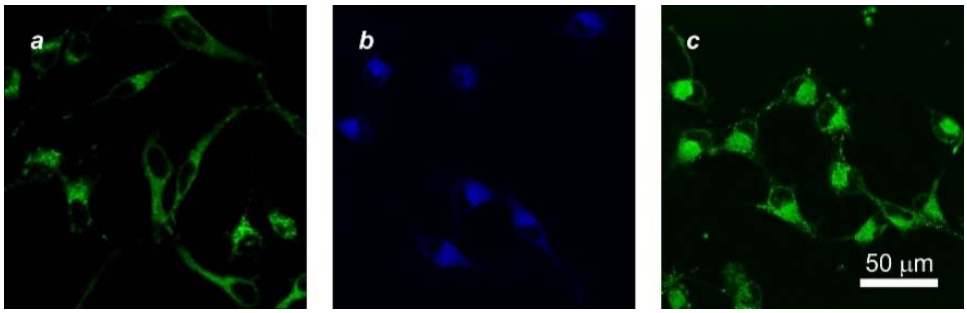

Figure 4.13 Fluorescence images of HeLa cells recorded after incubation with PBS dispersions of micelles of (***a***) **3** (125 μg mL^{-1}), containing **2** (1.25 μg mL^{-1}, λ_{Ex} = 518 nm, λ_{Em} = 530–560 nm), (***b***) **4** (250 μg mL^{-1}, λ_{Ex} = 458 nm, λ_{Em} = 470–510 nm) and (***c***) **4** (250 μg mL^{-1}), containing **2** (2.5 μg mL^{-1}, λ_{Ex} = 458 nm, λ_{Em} = 530–560 nm) for 3 hours and washing.

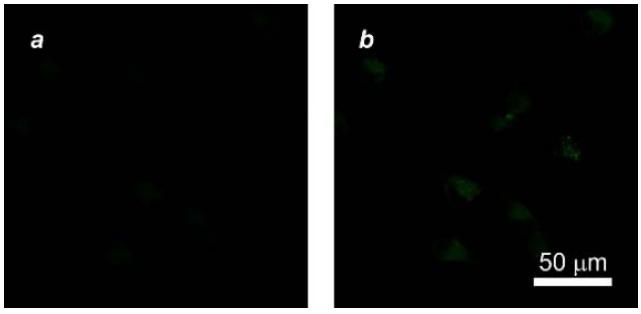

Figure 4.14 Fluorescence images (λ_{Ex} = 458 nm, λ_{Em} = 530–560 nm) of HeLa cells recorded after incubation with PBS dispersions of micelles of either (***a***) **4** (250 μg mL^{-1}) or (***b***) **5** (250 μg mL^{-1}) for 3 hours and washing.

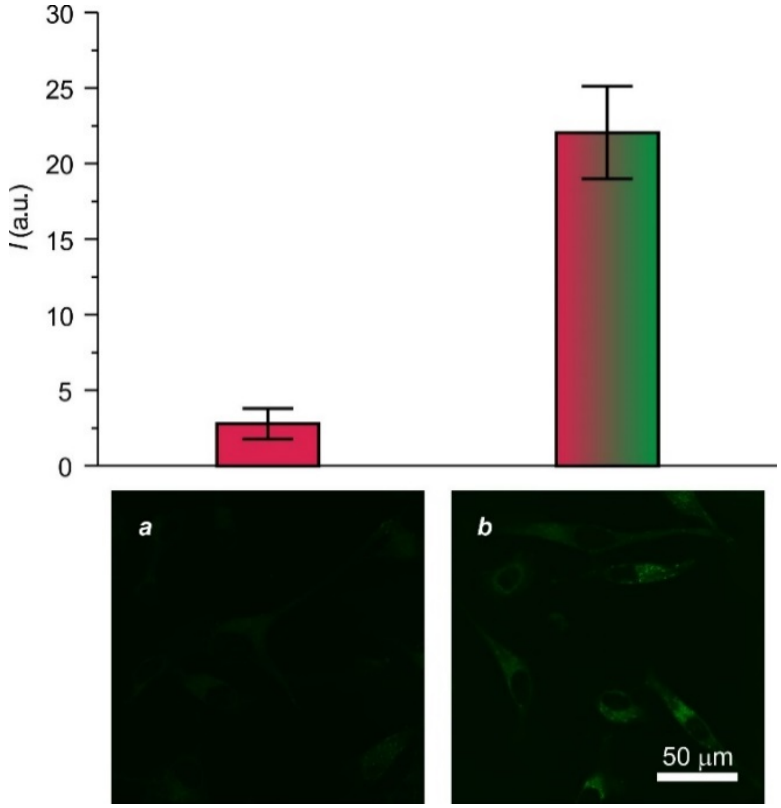

Figure 4.15 Fluorescence images (λ_{Ex} = 458 nm, λ_{Em} = 530–560 nm) of HeLa cells recorded after incubation with a PBS dispersion of micelles of **4** (250 μg mL^{-1},) for 3 hours and washing before (***a***) and after (***b***) subsequent incubation with a PBS dispersion of micelles of **5** (250 μg mL^{-1}) for 3 hours and washing together with the corresponding mean emission intensities measured along lines drawn across the cells.

The same illumination and detection conditions can be exploited to assess the ability of the nanostructured constructs to exchange their components in the intracellular space. Specifically, images (***a*** in Figures 4.15 and 4.16) of cells incubated with either **4** or **5** reveal only negligible fluorescence. In one instance, illumination at 458 nm excites the anthracene chromophores, but detection in the 530–560 nm range cannot record their emission. In the other case, the detection window overlaps the BODIPY emission, but their modest absorbance at the illumination wavelength prevents effective excitation. The subsequent incubation of the very same cells with the complementary macromolecular component produces instead intense intracellular fluorescence. More precisely, cells were

incubated with **4**, washed, incubated with **5** washed and finally imaged in one instance (***b*** in Figure 4.15). Alternatively, the two incubations steps were inverted in the other case (***b*** in Figure 4.16). Both protocols result in the localization of the two sets of macromolecules in close proximity within the intracellular space to enable efficient energy transfer and allow the detection of the acceptor fluorescence upon donor excitation. Consistently, measurements of the emission intensity along lines drawn across the cells before and after the second incubation step show a 7-fold fluorescent enhancement in both instances (bars in Figures 4.15 and 4.16).

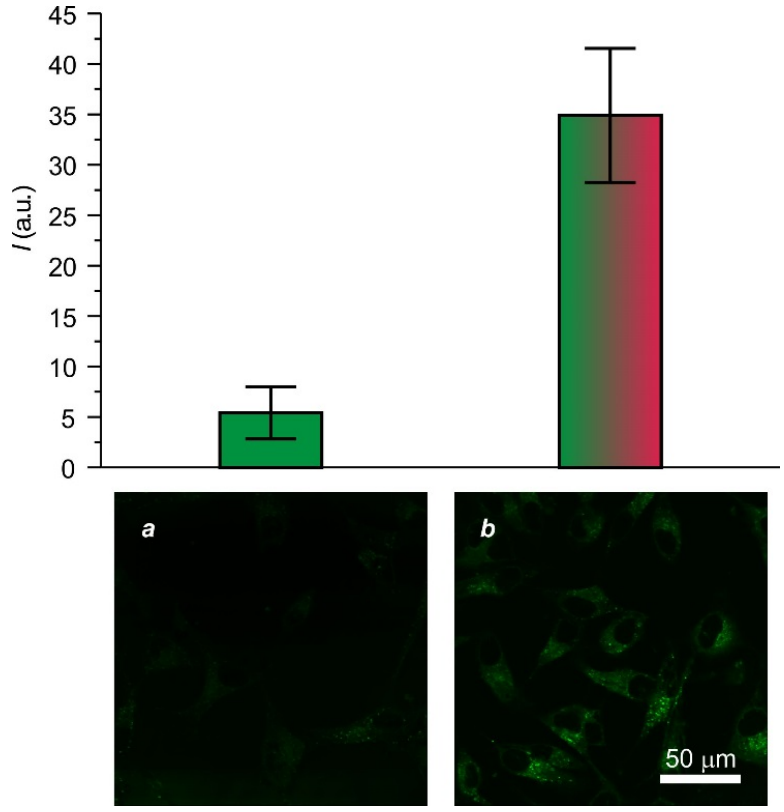

Figure 4.16 Fluorescence images (λ_{Ex} = 458 nm, λ_{Em} = 530–560 nm) of HeLa cells recorded after incubation with a PBS dispersion of micelles of **5** (250 µg mL^{-1},) for 3 hours and washing before (***a***) and after (***b***) subsequent incubation with a PBS dispersion of micelles of **4** (250 µg mL^{-1}) for 3 hours and washing together with the corresponding mean emission intensities measured along lines drawn across the cells.

4.3. Conclusions

Hydrophilic oligo(ethylene glycol) chains and hydrophobic decyl tails can be attached to a common poly(methacrylate) backbone to generate amphiphilic polymers capable of assembling spontaneously into micelles in aqueous environments. The resulting supramolecular assemblies can capture anthracene and/or BODIPY chromophores in their interior and allow the transfer of these, otherwise insoluble, hydrophobic molecules in hydrophilic media. Alternatively, the chromophoric components can be attached covalently to the amphiphilic macromolecules without preventing their ability to form nanostructured assemblies. In fact, covalent attachment actually tends to facilitate self-assembly and, as a result, lowers the critical concentration of the polymer required for micelle formation. Additionally, minor differences in the absorption and emission spectra suggest that the covalently- and noncovalently-encapsulated chromophores are in slightly different environments within the resulting micelles.

The covalent or noncovalent incorporation of anthracene and BODIPY chromophores in the same supramolecular construct results in energy transfer from the former to the latter upon excitation. The optimal spectral overlap of this particular donor–acceptor pair and their close proximity within the supramolecular assembly are responsible for energy transfer. However, the efficiency of the process when both chromophores are noncovalently encapsulated is greater than that observed when donor and acceptor are covalently attached. Presumably, the donor–acceptor distances and relative orientations differ in the two sets of supramolecular constructs. Energy transfer occurs also if one of the two fluorophores is covalently connected to the polymer components and the other is noncovalently encapsulated, or *vice versa*. Furthermore, these supramolecular constructs

exchange their polymer components with fast kinetics in aqueous dispersions. As a result, energy transfer is also observed upon mixing separate dispersions of micelles incorporating, either covalently or noncovalently, donors and acceptors.

The micellar assemblies can transport their covalently- and/or noncovalently-associated chromophores inside living cells and allow the detection of significant intracellular fluorescence. Furthermore, the nanocarriers and their cargo do not separate from each other after internalization. Indeed, the covalent attachment of the donors to the macromolecular components with the concomitant noncovalent encapsulation of the acceptors, or *vice versa*, results in efficient energy transfer in the intracellular space. Intracellular energy transfer is also established if cells are incubated with micelles containing the donors first and then with nanocarriers connected to the acceptors, or *vice versa*. In both instances, sequential incubation results in the localization of the complementary chromophores in close proximity within the intracellular space and allows energy transfer.

4.4. Experimental section

4.4.1. Materials and methods

Chemicals were purchased from commercial sources and used as received with the exception of THF, which was distilled over sodium and benzophenone, and H_2O, which was purified with a Barnstead International NANOpure DIamond Analytical system. Compounds **1**, **2** and **7**–**10** were prepared according to literature procedures.[117,269-273] GPC was performed with a Phenomenex Phenogel 5-μm MXM column (7.8 × 300 mm) operated with a Varian ProStar system, coupled to a ProStar 330 photodiode array detector, in THF at a flow rate of 1.0 mL min^{-1}. Monodisperse polystyrene standards (2,700–200,000) were

employed to determine the $\overline{M}_n$ and PDI of the polymers from the GPC traces, following a literature protocol.[274] EISMS was performed with a Bruker micrOTO-Q II spectrometer. NMR spectra were recorded with a Bruker Avance 400 spectrometer. DLS measurements were performed with a Malvern ZEN1600 apparatus. The values listed for d_H in Table 4.1 are averaged over ten independent experiments of ten runs of 10 s each. SLS measurements were performed with the same apparatus. The values of w_S reported in ref. [274] were determined from the concentration dependence of the scattering intensity, following a literature protocol.[274] Absorption spectra were recorded with a Varian Cary 100 Bio spectrometer, using quartz cells with a path length of 1.0 cm. Emission spectra were recorded with a Varian Cary Eclipse spectrometer in aerated solutions. Fluorescence quantum yields were determined with a fluorescein standard, following a literature protocol.[1] Fluorescence images were recorded with a Leica SP5 confocal laser-scanning multiphoton microscope, equipped with an incubator maintained at 37 °C in O_2/CO_2/air (20:5:75, v/v/v).

4.4.2. Synthesis of 3

A solution of **8** (73 mg, 0.3 mmol), **9** (1 g, 0.5 mmol) and AIBN (3 mg, 0.03 mmol) in degassed THF (8 mL) was heated for 72 hours at 75 °C under Ar in a sealed vial. After cooling down to ambient temperature, the reaction mixture was transferred to a centrifuge tube and diluted with THF to a total volume of 10 mL. Hexane was added in portions of 1 mL and the tube was shaken vigorously, after each addition, until the formation of a precipitate was clearly observed. After centrifugation, the oily layer at the bottom of the tube was separated from the supernatant and dissolved in THF (10 mL). The treatment with hexane, followed by centrifugation, was repeated 3 times and the final oily residue

was dried under reduced pressure to give **3** (0.4 g) as a white solid. GPC: $\overline{M}_n$ = 14,692, $Đ$ = 1.20; ^{1}H NMR ($CDCl_3$): δ = 0.75–0.91 (3H, m), 0.95–1.36 (16H, m), 1.55–1.65 (6H, m), 1.75–2.05 (4H, m), 3.34–3.38 (3H, s), 3.45–3.75 (178H, m), 3.85–4.25 (4H, m).

4.4.3. Synthesis of 4 and 5

A solution of **8** (64 mg, 0.3 mmol), **9** (940 mg, 0.5 mmol), AIBN (5 mg, 0.03 mmol) and either **6** (42 mg, 0.1 mmol) or **7** (46 mg, 0.1 mmol) in degassed THF (8 mL) was heated at 75 °C for 65 h under Ar in a sealed vial. After cooling down to ambient temperature, the mixture was transferred to a centrifuge tube and diluted with THF to a total volume of 10 mL. Hexane was added in portions of 1 mL and the tube was shaken vigorously, after each addition, until the formation of a precipitate was clearly observed. After centrifugation, the oily layer at the bottom of the tube was separated from the supernatant and dissolved in THF (10 mL). Hexane was added in portions of 1 mL and the tube was shaken vigorously, after each addition, until the formation of a precipitate was clearly observed. After centrifugation, the oily residue was separated from the supernatant and dried under reduced pressure to give either **4** (250 mg) or **5** (170 mg) as a yellow or red solid respectively. **4**: GPC: $\overline{M}_n$ = 14,332, $Đ$ = 1.68; ^{1}H NMR ($CDCl_3$): δ = 0.75–0.92 (14H, m), 1.17–1.41 (74H, m), 1.52–1.68 (34H, m), 1.86–1.98 (22H, m), 3.37 (17H, s), 3.50–3.75 (997H, m), 3.88 (3H, s), 4.05–4.20 (20H, m), 6.55–7.02 (5H, m), 7.5–8.0 (9H, m), 8.60–8.72 (2H, m). **5**: GPC: $\overline{M}_n$ = 15,911, $Đ$ = 1.65; ^{1}H NMR ($CDCl_3$): δ = 0.85–0.95 (5H, m), 1.10–1.21 (6H, m), 1.25–1.46 (34H, m), 1.65–1.75 (14H, m), 1.90–2.10 (8H, m), 2.16 (4H, s), 2.25–2.35 (1H, m), 2.51 (6H, s), 3.37 (6H, s), 3.50–3.76 (347H, m), 3.90–4.03 (7H, m), 7.14–7.22 (4H, m).

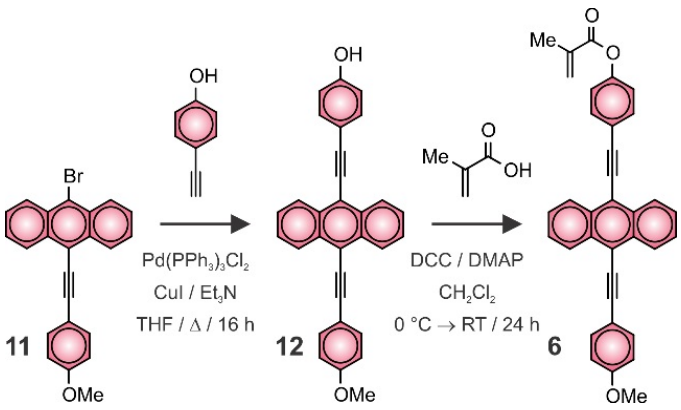

Figure 4.17 Synthesis of **6**.

6: A solution of DCC (68 mg, 11 mmol) in CH_2Cl_2 (4 mL) was added dropwise, over the course of 20 min, to a solution of **12** (130 mg, 0.3 mmol), DMAP (7 mg, 0.06 mmol) and methacrylic acid (29 mg, 0.3 mmol) in CH_2Cl_2 (8 mL) maintained at 0 °C under Ar. The mixture was allowed to warm to ambient temperature and was stirred for a further 24 hours under these conditions. The solvent was distilled off under reduced pressure. The residue was purified by column chromatography [SiO_2: hexane/EtOAc (9:1, v/v)] to afford **6** (80 mg, 54%) as a yellow solid. ESIMS: m/z = 492 $[M - H]^-$; ^{1}H NMR ($CDCl_3$): δ = 2.12 (3H, s), 3.91 (3H, s), 5.83 (1H, s), 6.42 (1H, s), 7.00–7.03 (2H, d, 9 Hz), 7.25 (1H, s), 7.61–7.70 (5H, m), 7.73–7.76 (2H, d, 9 Hz), 7.81–7.84 (2H, d, 9 Hz), 8.68–8.73 (4H, m); ^{13}C NMR ($CDCl_3$): δ = 18.3, 18.5, 26.7, 55.4, 85.4, 86.9, 101.4, 102.7, 114.3, 115.5, 117.8, 119.1, 121.0, 121.8, 122.0, 126.7, 126.8, 127.2, 127.4, 127.6, 127.9, 129.9,132.0, 132.8, 133.2, 134.7,135.5, 135.7, 151.1, 154.7, 160.1, 165.3, 165.3, 165.6, 196.9.

12: Ar was bubbled through a solution of **13** (335 mg, 0.9 mmol) in a mixture of THF (3 mL) and Et_3N (6 mL) for 15 min at ambient temperature. 4-Ethynylphenol (308 mg, 3 mmol), $Pd(PPh_3)_3Cl_2$ (120 mg, 0.2 mmol) and CuI (33 mg, 0.3 mmol) were added to the degassed solution and the resulting mixture was heated under reflux and Ar for 16 h. After

cooling down to ambient temperature, the solvent was distilled off under reduced pressure. The residue was purified by column chromatography [SiO_2, hexane/EtOAc (9:1, v/v)] to afford **12** (150 mg, 41%) as a yellow solid. ESIMS: $m/z = 423$ $[M - H]^-$; ^1H NMR ($CDCl_3$): $\delta = 3.89$ (3H, s), 5.12 (1H, bs), 6.87−6.89 (1H, d, 8 Hz), 6.92–6.94 (2H, d, 8 Hz), 6.98–7.0 (2H, d, 8 Hz), 7.60–7.74 (7H, m), 7.90–7.92 (1H, d, 8 Hz), 8.66–8.71 (3H, m); ^{13}C NMR ($CDCl_3$): $\delta = 26.4$, 55.4, 85.3, 85.4, 102.2, 102.5, 114.2, 115.3, 115.6, 115.7, 115.9, 118.4, 118.5, 126.6, 127.3,127.3, 131.0, 132.0, 132.0, 133.2, 133.4, 156.08, 160.0.

4.4.4. Micelles of 3 loaded with 1, 2 or both

A solution of **3** (2.5 mg mL^{-1}) in $CHCl_3$ (200 μL) was mixed with a solution of **1** (0.1 mg mL^{-1}), **2** (0.1 mg mL^{-1}) or both (0.1 mg mL^{-1} each) in $CHCl_3$ (30 μL). The solvent was evaporated under reduced pressure and the residue was dispersed in PBS (1.0 mL, pH = 7.0). After sonication for 5 min, the dispersion was passed through a syringe filter (0.2 μm cellulose acetate membrane) and the filtrate was used for the spectroscopic experiments without further purification.

4.4.5. Micelles of 4 and 5

A solution of **4** (1.0 mg mL^{-1}) in $CHCl_3$ (300 μL) was mixed with a solution of **5** (1.0 mg mL^{-1}) in $CHCl_3$ (300 μL). The solvent was evaporated under reduced pressure and the residue was dispersed in PBS (1.0 mL, pH = 7.0). After sonication for 5 min, the dispersion was passed through a syringe filter (0.2 μm cellulose acetate membrane) and the filtrate was used for the spectroscopic experiments without further purification. Alternatively, the $CHCl_3$ solutions of **4** and **5** were concentrated under reduced pressure individually and the two residues were dispersed in PBS (0.5 mL, pH = 7.0). After sonication for 5 minutes,

the two dispersions were filtered and equal volumes of the filtrates were mixed and the resulting dispersion was used for spectroscopic experiments without further purification.

4.4.6. Micelles of 4 loaded with 2

A solution of **4** (1.0 mg mL^{-1}) in $CHCl_3$ (300 μL) was mixed with a solution of **2** (0.1 mg mL^{-1}) in $CHCl_3$ (20 μL). The solvent was evaporated under reduced pressure and the residue was dispersed in PBS (1.0 mL, pH = 7.0). After sonication for 5 min, the dispersion was passed through a syringe filter (0.2 μm cellulose acetate membrane) and the filtrate was used for the spectroscopic experiments without further purification.

4.4.7. Micelles of 5 loaded with 1

A solution of **5** (1.0 mg mL^{-1}) in $CHCl_3$ (300 μL) was mixed with a solution of **1** (0.1 mg mL^{-1}) in $CHCl_3$ (30 μL). The solvent was evaporated under reduced pressure and the residue was dispersed in PBS (1.0 mL, pH = 7.0). After sonication for 5 min, the dispersion was passed through a syringe filter (0.2 μm cellulose acetate membrane) and the filtrate was used for the spectroscopic experiments without further purification.

4.4.8. Cells

HeLa cells were cultured in Dulbecco's modified Eagle's media supplemented with fetal bovine serum (10%, v/v), penicillin (200 U mL^{-1}), streptomycin (200 μg mL^{-1}) and nonessential amino acids (0.1 mM) and incubated at 37 °C in O_2/CO_2/air (20:5:75, v/v/ v). The cells were seeded in 384-well glass-bottom plates at a density of 5×10^4 cells mL^{-1} and incubated overnight at 37 °C in O_2/CO_2/air (20:5:75, v/v/v). The cultured cells were incubated further with PBS dispersions (50%, v/v) of micelles of **3** (250 μg mL^{-1}) loaded with either **1** (2.5 μg mL^{-1}) or **2** (1.25 μg mL^{-1}) for 3 hours and then washed three times with PBS (80 μL) and imaged. Alternatively, cells were incubated with PBS dispersions

(50%, v/v) of micelles of either **4** (250 μg mL^{-1}) or **5** (250 μg $mL^{-1)}$ with and without loading of the complementary donor or acceptor [*i.e.*, either **1** (2.5 μg mL^{-1}) or **2** (2.5 μg mL^{-1})] for 3 hours and then washed three times with PBS (80 μL) and imaged. In selected experiments, cells incubated with PBS dispersions (50%, v/v) of micelles of **4** (250 μg mL^{-1}) or **5** (250 μg mL^{-1}) for 3 hours were washed and subsequently incubated with micelles of **3** (250 μg mL^{-1}) containing the complementary donor or acceptor [*i.e.*, either **1** (2.5 μg mL^{-1}) or **2** (2.5 μg mL^{-1})] for a further 3 hours, washed three times with PBS (80 μL) and imaged.

CHAPTER 5

BIOIMAGING WITH MACROMOLECULAR PROBES INCORPORATING MULTIPLE BODIPY FLUOROPHORES

5.1. Background

Fluorescence measurements[1] permit the detection of cells in biological fluids[275] and the visualization of tissues in living organisms.[276] Fast response, inherent sensitivity and noninvasive character are the main reasons behind their widespread application in cytometry and imaging. Their experimental implementation, however, requires first the labeling of a given biotarget with appropriate fluorescent probes.[277] Generally, a fluorescent chromophore is attached to a targeting agent, in the form of an antibody, an aptamer, a peptide or even a relatively small ligand, capable of directing selectively the signaling unit to the target of interest. The supramolecular association of the complementary components then immobilizes the fluorophore on the target and allows the detection of the latter after collecting the emission of the former. Under these conditions, the brightness of the fluorophore ultimately dictates the intensity of the detected signal and the sensitivity of the overall protocol.[275,276] This particular photophysical parameter is equal to the product of the molar absorption coefficient (ε) of the fluorophore at the excitation wavelength and its fluorescence quantum yield (ϕ).[1] For most organic fluorophores, ε is lower than 10^2 mM^{-1} cm^{-1} and, therefore, their brightness ($\varepsilon \times \phi$) barely approaches 10^2 mM^{-1} cm^{-1}, even when ϕ is close to unity. For example, indocyanine green, which is one of the most common synthetic dyes for fluorescence measurements *in vivo* and is approved for use in humans, has a brightness of only 11 mM^{-1} cm^{-1}.[278]

In principle, more than one fluorescent chromophore can be attached to a single targeting agent, in order to increase the values of ε and, hence, the brightness associated with each

binding event. However, the clustering of independent fluorophores within a restricted volume generally leads to significant interactions in the excited state that inhibit radiative deactivation.[1] Therefore, the increase in ε with the assembly of multiple chromophores into a single molecular, macromolecular or supramolecular construct is often counteracted by a pronounced decrease, or even complete suppression, of ϕ. As a consequence of this fundamental limitation, inherent to the excitation dynamics of organic chromophores, the identification of viable designs to integrate multiple fluorophores within relatively compact synthetic structures to enhance brightness remains far from trivial.[111,248,252,279-286]

Hundreds of identical chromophores can be encapsulated within the same polymer particle to generate fluorescent assemblies with a brightness approaching 10^4 mM^{-1} cm^{-1}.[287-291] Such brightness levels are several orders of magnitude greater than those accessible with individual organic fluorophores and far exceed even those of semiconductor quantum dots.[292,293] Nonetheless, the encapsulation of the fluorescent guests within the polymer particles and, often, also the structural integrity of the host matrix itself are a result of noncovalent interactions. The reversible nature of these supramolecular contacts can lead to the leakage of the guests out of the particles, as well as to the disassembly of the hosts, under the extreme dilution that can occur in biological fluids. A possible solution to this problem can be the covalent connection, rather than the noncovalent encapsulation, of many emissive chromophores to a common polymer chain[248,286] or cross-linked scaffold.[284] For example, polymers with borondipyrromethene (BODIPY) fluorophores in their side chains can be assembled with relatively simple synthetic procedures to generate efficiently covalent constructs with a brightness that can also approach 10^4 mM^{-1} cm^{-1}.[271,294] Nonetheless, the hydrodynamic diameter (d_H) of these fluorescent constructs, as well as of

those of their noncovalent counterparts, exceeds 50 nm in most instances.[287-291] Such physical dimensions are more than two orders of magnitude greater than those of a single chromophore and can have detrimental effects on the supramolecular association of the targeting agent, as well as complicate administration *in vivo* and clearance from the organism. Thus, viable structural designs to engineer fluorescent probes with bright emission together with long-term stability, compact dimensions, targeting compatibility and lack of toxicity are still very much needed. The availability of such materials would be particularly valuable in the biomedical laboratory and could ultimately facilitate the implementation of clinical and surgical applications based on convenient fluorescence measurements.

Our laboratories developed a series of amphiphilic polymers with multiple decyl and oligo(ethylene glycol) side chains along a common poly(methacrylate) backbone.[23,29,32,34,111-114,117,148,295-299] In aqueous environments, these macromolecules assemble spontaneously into particles with d_H close to 20 nm, hydrophilic surface and hydrophobic interior. In the process of assembling, they can capture multiple hydrophobic fluorophores in their interior and transfer these, otherwise insoluble, chromophores into aqueous solutions. The supramolecular shell encapsulating the fluorescent components protects them from the aqueous environment and preserves their photophysical properties. Furthermore, the hydrophobic side chains of the macromolecular components isolate the entrapped fluorophores form each other, preventing interchromophoric interactions in both the ground as well as excited states. As a result, a negligible influence on ϕ is generally observed upon encapsulation of multiple fluorophores within these supramolecular containers, offering the possibility of constructing supramolecular assemblies with

relatively large brightness. Nonetheless, noncovalent contacts are solely responsible for holding fluorophores and polymers together. In fact, these supramolecular nanocarriers can discharge their fluorescent cargo into the many lipophilic domains found in biological preparations.[114,148] These considerations suggested the design of similar amphiphilic macromolecular constructs with multiple fluorophores covalently connected to the polymer backbone, instead of being noncovalently encapsulated into the corresponding supramolecular nanocarriers.[114] This chapter reports the synthesis and characterization of two families of macromolecular probes engineered around this structural design, together with the spectroscopic investigation of their photophysical properties and the assessment of their performance in model biological preparations.

5.2. Results and discussion

5.2.1. Design, synthesis and structural characterization

Two structural designs for the covalent integration of borondipyrromethene (BODIPY) chromophores within amphiphilic macromolecular constructs were envisaged. In one, the chromophoric units are directly attached to a poly(methacrylate) backbone together with decyl and oligo(ethylene) side chains (**1** Figure 5.1). In the other, the chromophores are connected to the ends of the hydrophobic side chains (**2** in Figure 5.2). Both were prepared from the random polymerization of the corresponding methacrylate monomers in tetrahydrofuran (THF), under the assistance of azobis(*i*-butyrronitrile) (AIBN). In the first instance, the stoichiometry of the three monomers was varied systematically to produce six macromolecules (**1a**–**e** in Table 5.1) differing in the number (*N* in Table 5.1) of chromophores per polymer chain and in the ratio (χ in Table 5.1) between the hydrophobic and hydrophilic side chains. The second design was exploited to assemble macromolecules

without and with (**2a** and **2b** in Figure 5.2) a third side chain terminated by a carboxylic acid. The latter was treated with *N*-hydroxysuccinimide (NHS), *N*,*N*-dicyclohexylcarbodiimide (DCC) and 4-*N*,*N*-dimethylaminopyridine (DMAP) in dichloromethane and then coupled to a secondary antibody (**9** in Figure 5.2) in *N*,*N*-dimethylformamide (DMF) and bicarbonate buffer (BCB). The resulting conjugate (**2c** in Figure 5.2) was isolated from any unreacted starting materials by size-exclusion chromatography.

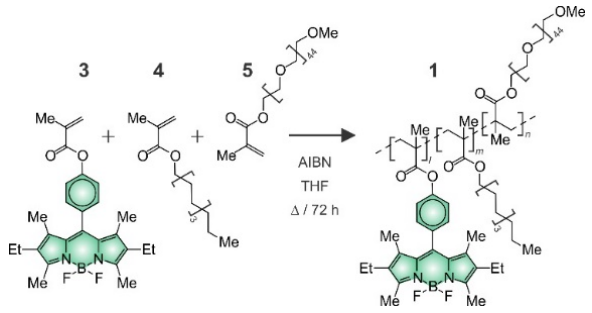

Figure 5.1 Synthesis of amphiphilic polymers **1a–e**.

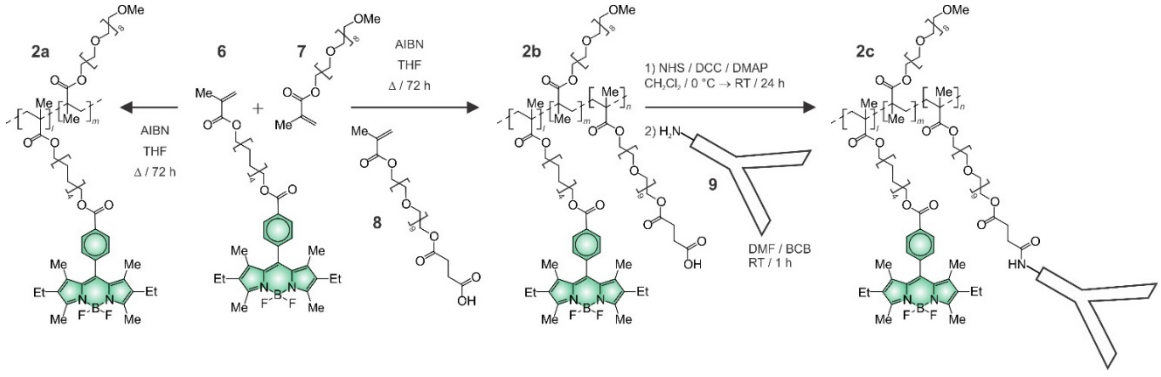

Figure 5.2 Synthesis of amphiphilic polymers **2a** and **2b** and antibody conjugation of the latter to produce **2c**.

Table 5.1 Structural parameters of **1a–e**, **2a** and **2b** [*a*].

	$\bar{M}_n$ (kDa)	$Đ$	N	χ	CMC (μg mL^{-1})	d_H (nm)
1a	14.0	1.42	1.2	1.3	57.1	13.4
1b	24.9	2.34	2.7	1.1	53.7	8.7
1c	17.9	1.69	1.0	1.2	61.5	13.4
1d	16.4	1.53	5.6	2.0	104.1	21.0
1e	21.8	1.90	5.3	3.6	98.3	10.0
2a	20.2	2.26	7.4	0.2	43.4	9.0
2b	15.8	2.36	6.4	0.3	41.7	8.0

[*a*] The number average molecular weight ($\bar{M}_n$) and dispersity index ($Đ$) were determined by GPC in THF, against monodisperse polystyrene standards (2.7–200.0 kDa). The number (N) of chromophore per polymer chain and the ratio (χ) between the hydrophobic and hydrophilic segments of each macromolecule were determined by ^{1}H NMR spectroscopy in CD_2Cl_2 or $CDCl_3$. The critical micellar concentration (CMC) was determined by emission spectroscopy in PBS. The hydrodynamic diameter (d_H) were measured by DLS in PBS at a concentration greater than the corresponding CMC.

Gel permeation chromatography (GPC) of **1a**–**e**, **2a** and **2b** indicated their number average molecular weight ($\bar{M}_n$ in Table 5.1) to range from 15.8 to 24.9 kDa with a dispersity index ($Đ$ in Table 5.1) varying from 1.39 to 2.36. Integration of the resonances associated with protons of the BODIPY chromophores, hydrophobic chains and hydrophilic tails in the corresponding ^{1}H NMR spectra provided estimates of N and χ (Table 5.2). For example, the ^{1}H NMR spectrum (Figure 5.3) of **1e** shows a multiplet at 7.30 ppm for the two pairs of homotopic protons on the phenylene ring of the BODIPY chromophores, a singlet at 3.36 ppm for the methoxy protons at termini of the hydrophilic chains and a multiplet at 0.88 ppm for the methyl protons at the ends of the hydrophobic chains. These three sets of resonances integrate for 4, 5 and 18 protons respectively. These values correspond to a N of 5.3 and a χ of 3.6. Similarly, the ^{1}H NMR spectrum (Figure 5.3) of **2b** shows a pair of doublets at 8.16 and 7.39 ppm for the phenylene protons of the BODIPY chromophores and a singlet at 3.36 ppm for the methoxy protons of the hydrophilic chains. These resonances integrate for 4 and 10 protons respectively and correspond to N and χ of 6.4

and 0.3 respectively. Additionally, the spectrum shows also a multiplet at 2.64 ppm for the methylene protons adjacent to the carboxylic acid, integrating for 1 proton. This value suggest that **2b** incorporates an average of 1.6 chains with terminal carboxylic acids within its macromolecular backbone.

Table 5.2 Absorption (λ_{Ab}) and emission (λ_{Em}) wavelengths, molar absorption coefficient (ε), fluorescence quantum yield (ϕ) and brightness ($\varepsilon \times \phi$) of **1a–e**, **2a**, **2b** and **10** at 25 °C [*a*].

	λ_{Ab} (nm)		λ_{Em} (nm)		ε (mM^{-1} cm^{-1})		ϕ		$\varepsilon \times \phi$ (mM^{-1} cm^{-1})	
	THF	PBS	THF	PBS	THF	PBS	THF	PBS	THF	PBS
1a	526	528	538	546	69.6	53.28	0.71	0.38	49.4	20.2
1b	526	527	537	541	156.6	119.88	0.54	0.18	84.6	21.6
1c	526	528	540	545	58	44.4	0.46	0.17	26.7	7.5
1d	526	529	541	550	324.8	248.64	0.55	0.1	178.6	24.9
1e	526	529	541	546	307.4	235.32	0.67	0.26	206.0	61.2
2a	526	529	542	550	429.2	328.56	0.45	0.18	193.1	59.1
2b	526	529	542	553	359.6	275.28	0.50	0.18	179.8	49.6
10	527	528	541	541	58	44.4	0.63	0.51	36.4	22.6

[*a*] The photophysical parameters of **1a–e**, **2a** and **2b** were determined at a concentration (30 μg mL^{-1}) that is lower than the corresponding CMC. The values of ε listed for **1a–3**, **2a** and **2b** are the products of that of **10** and the number (*N* in Table 1) of chromophores per polymer chain. The values of ϕ were determined in aerated solutions against a fluorescein standard.

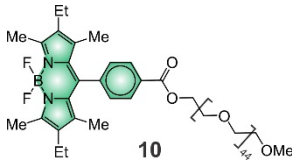

10

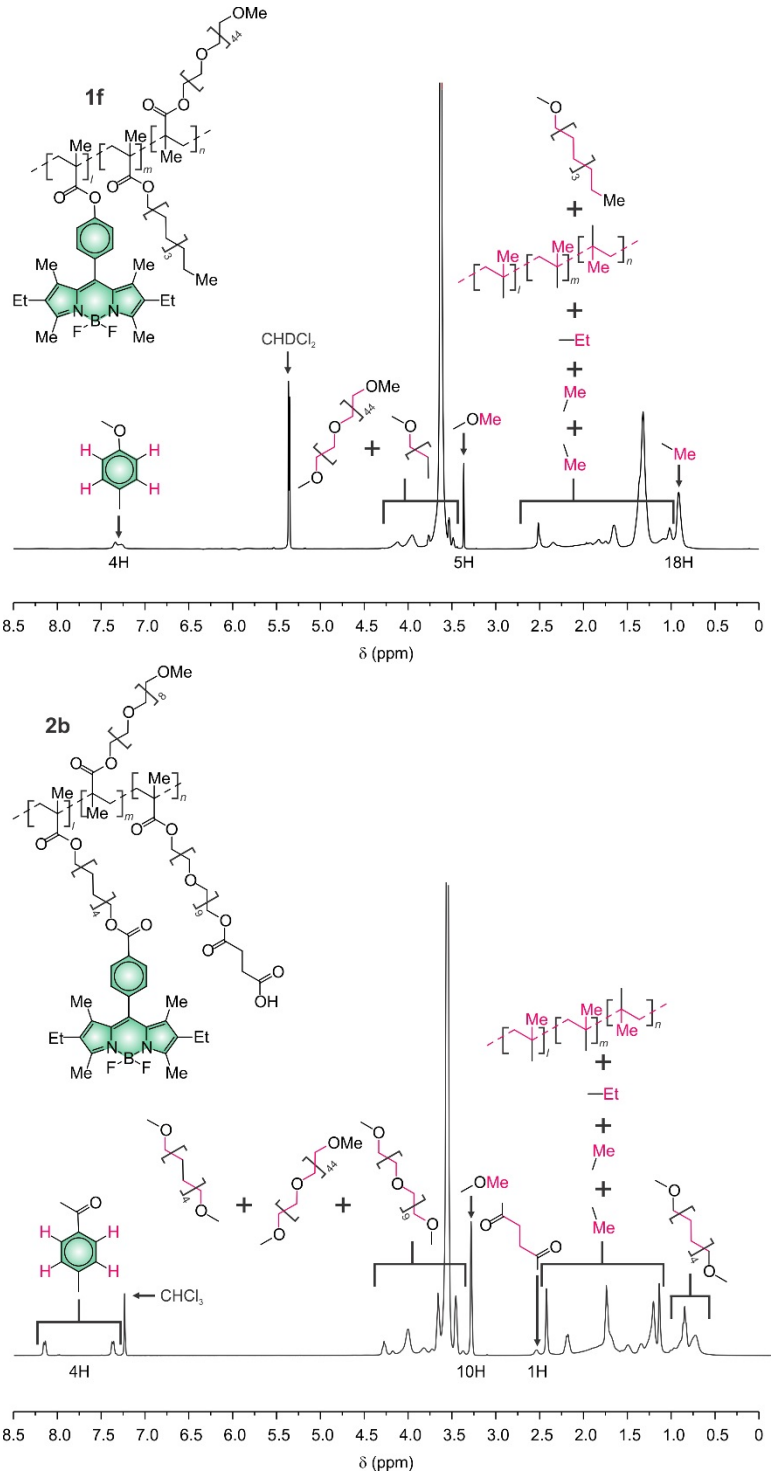

Figure 5.3 ^{1}H NMR spectra (500 MHz) of **1e** and **2b** in CD_2Cl_2 and $CDCl_3$ respectively at 25 °C.

5.2.2. Absorption and emission spectroscopies

The absorption and emission spectra (Figure 5.4) of a model monomer (**10** in Table 5.2) dissolved in THF show the characteristic bands of the BODIPY chromophore with maxima at wavelengths (λ_{Ab} and λ_{Em} in Table 5.2) of 527 and 540 nm. The very same bands are also observed for all polymers (Figure 5.3) with minimal shifts in λ_{Ab} and λ_{Em}. The presence of multiple BODIPY chromophores, however, enhances the molar absorption coefficient (ε in Table 5.2) at λ_{Ab} from 58.0 mM^{-1} cm^{-1} for monomer **10** to up to 429.24 mM^{-1} cm^{-1} for polymer **2a**, but has negligible influence on the fluorescence quantum yield (ϕ in Table 5.2). Specifically, ϕ is 0.63 for **10** and ranges from 0.45 to 0.71 for the polymers. As a result, the brightness ($\varepsilon \times \phi$ in Table 5.2) of all polymers is greater than that of the monomer and approaches 206.0 mM^{-1} cm^{-1} for polymer **1e**, while it is only 36.4 mM^{-1} cm^{-1} for **10**. Furthermore, this photophysical parameter increases with N for both series of polymers. The only outliner on this trend is **1d**, which has more chromophores per polymer chain but lower brightness than **1e**. Presumably, this apparent contradiction is a consequence of the high relative amount (χ in Table 5.1) of hydrophobic components in **1e** that ensure the effective insulation of the chromophores from each other. These observations suggest that the brightness of these macromolecules can be optimized even further with the elongation of their polymer backbone, and hence of their $\bar{M}_n$, as long as a significant excess of hydrophobic components, relative to their hydrophilic counterparts, is maintained within the overall amphiphilic construct.

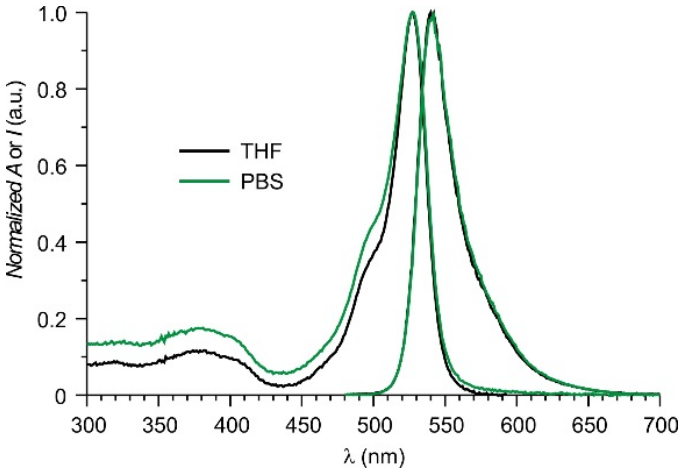

Figure 5.4 Normalized absorption and emission spectra (14 μg mL^{-1}, λ_{Ex} = 470 nm) of **10** in THF and PBS at 25 °C.

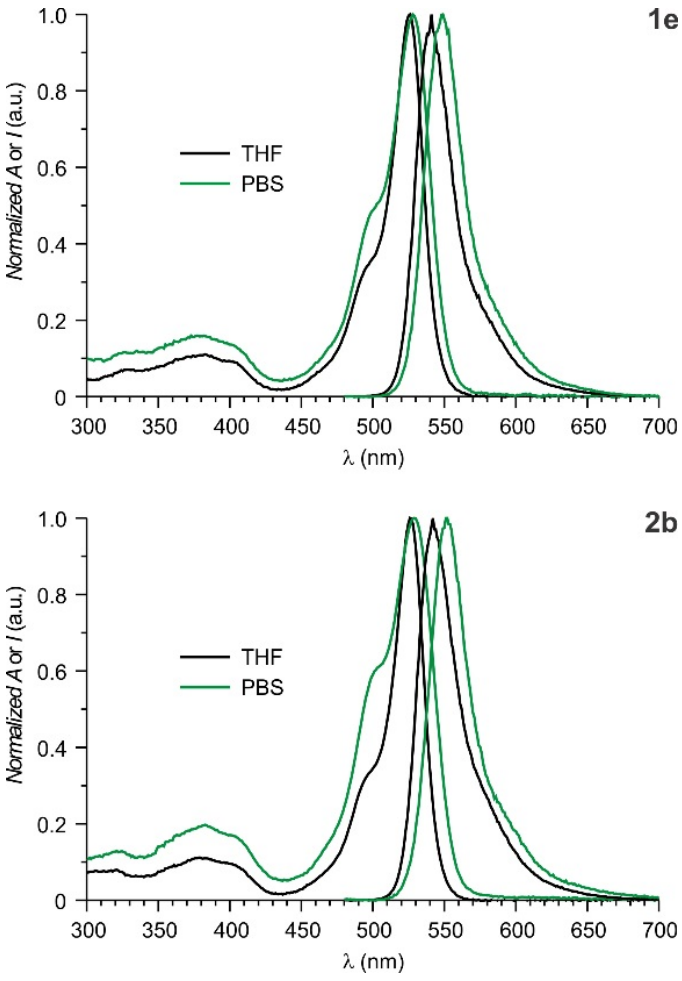

Figure 5.5 Normalized absorption and emission spectra (30 μg mL^{-1}, λ_{Ex} = 470 nm) of **1e** and **2b** in THF and PBS at 25 °C.

The transition from THF to phosphate buffer saline (PBS) has negligible influence on the photophysical parameters of the monomer (Table 5.2 and Figure 5.4). By contrast, it shifts bathochromically λ_{Em} and depresses ϕ for all polymers (Table 5.2 and Figure 5.5). These observations suggest that the environment around the BODIPY chromophores changes drastically on going from organic to aqueous solution only when they are attached to a macromolecular backbone. Presumably, the amphiphilic polymers alter their geometry significantly to avoid direct exposure of their hydrophobic domains to water molecules and encourage the nonradiative deactivation of the excited BODIPY chromophores. In spite of these effects, the brightness of some of the polymers remains greater than that of the monomer, which is only 22.6 mM^{-1} cm^{-1} under these conditions. Specifically, **1e** maintains the largest brightness, out of all the macromolecular constructs tested, to approach 61.2 mM^{-1} cm^{-1}.

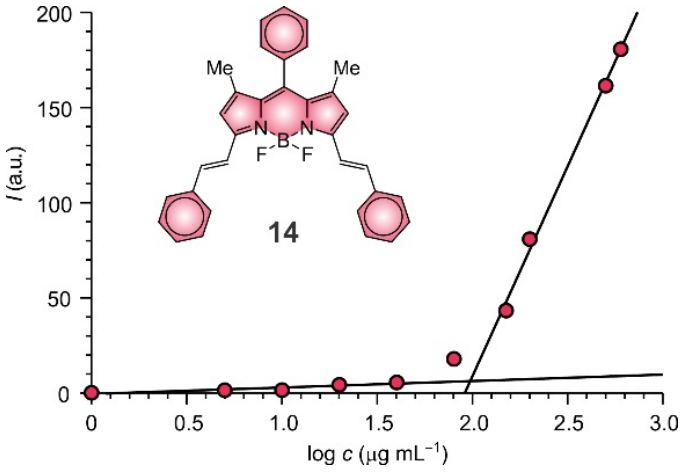

Figure 5.6 Dependence of the emission intensity (λ_{Ex} = 580 nm, λ_{Em} = 635 nm) of **14** on the concentration of **1f** in PBS at 25 °C.

The photophysical parameters of **1a**–**e**, **2a** and **2b** were determined at a concentration of 30 μg mL^{-1}. This value is lower than the corresponding critical micellar concentration

(CMC in Table 5.1), which ranges from 43.4 to 104.1 μg mL^{-1}, and was selected to avoid the aggregation of the amphiphilic polymers into supramolecular assemblies in aqueous environment. In turn, the CMC of all macromolecules was determined with the aid of a hydrophobic BODIPY chromophore (**14** in Figure 5.6) with extended electronic conjugation. This compound is essentially insoluble in PBS and its fluorescence can be detected only in the presence of sufficient amounts of any one of the eight amphiphilic polymers. Indeed, plots (Figure 5.6) of the emission intensity of **14** against the polymer concentration all show a sudden fluorescence increase above a given concentration threshold, which is the corresponding CMC value. These observations suggest that at concentrations greater than the threshold values the amphiphilic macromolecules assemble into supramolecular nanocarriers capable of capturing **14** in their hydrophobic interior, transfer it into the aqueous phase and allow the detection of its fluorescence. Consistently, dynamic light scattering (DLS) measurements performed at concentrations greater than CMC confirm the formation of nanoscaled aggregates with hydrodynamic diameters (d_H in Table 5.1) ranging from 8.0 to 21.0 nm.

5.3. Fluorescence imaging

Images of live *Caenorhabditis elegans*, microinjected with either blank PBS (***a*** in Figure 5.7) or a PBS solution of **10** (***b*** in Figure 5.7) in the gonadal region, show the fluorescent probes to accumulate in the fate droplets of the intestinal tract of the nematode. Under identical experimental conditions, injection of **1e** (***c*** in Figure 5.7) resulted in bright, diffuse fluorescence throughout the rest of the nematode with the exception of the eggs. Presumably, the different distribution of **1e** and **10** is a consequence of the amphiphilic character of the former and hydrophilic of the latter. The hydrophilic model system can

only localize into the hydrophilic intestinal tract, while the amphiphilic polymer can diffuse also into hydrophobic domains of the worm.

The emission intensity detected within the living organism for the macromolecular probe is significantly greater than that measured for the model monomer. Fluorescence profiles (Figure 5.5), collected along lines drawn across the imaged nematodes, reveal a 4-fold enhancement in emission for the polymer, even although the concentration (50 μM) of the probes was the same in both injected solutions. These observations are fully consistent with the brightness measured spectroscopically for the two systems in PBS, which is 61.2 mM^{-1} cm^{-1} for **1e** but only 22.8 mM^{-1} cm^{-1} for **10** (Table 5.2), and demonstrate that the macromolecular probe retains its photophysical properties within the living organism. Furthermore, the injected polymer does not appear to have any effect on the nematode. Sequences of images, recorded to monitor the movements of the worms in real time, do not reveal any significant difference in the behavior of three injected nematodes over the course of 60 min.

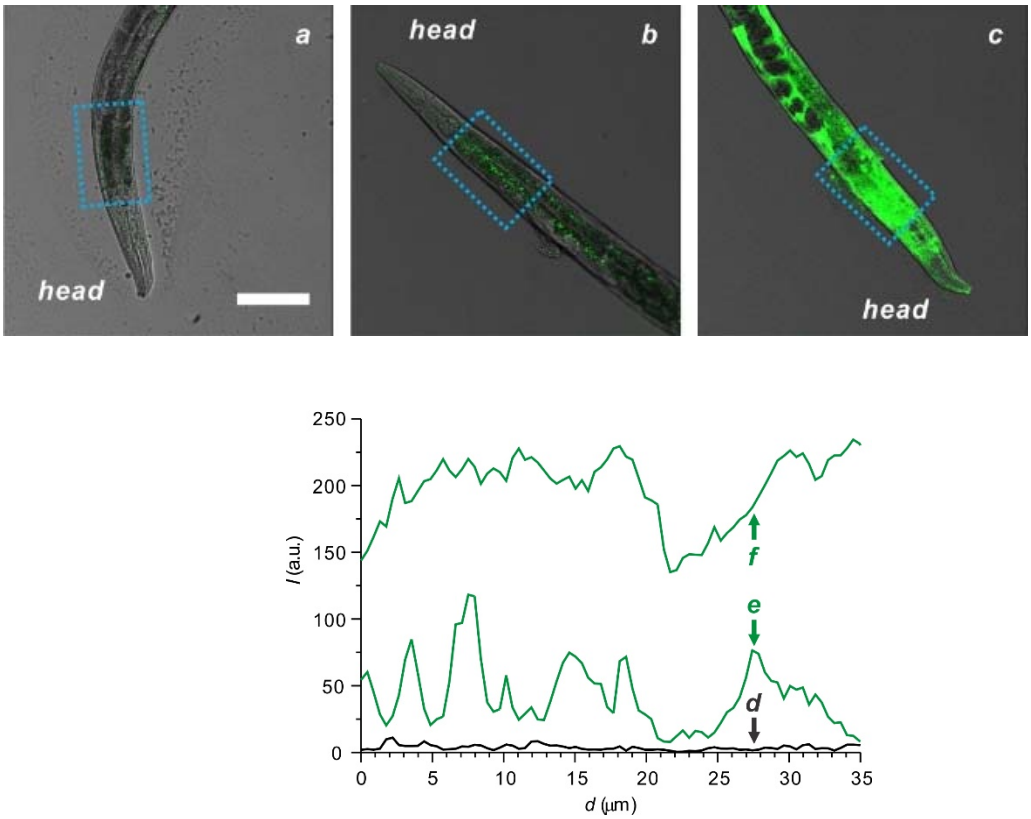

Figure 5.7 Overlaid fluorescence (λ_{Ex} = 514 nm, λ_{Em} = 530–650 nm) and bright field (scale bar = 100 μm) of *Caenorhabditis elegans* injected with PBS (***a***), a PBS solution of **10** (***b***) or a PBS solution of **1e** (***c***). Plots of the emission intensity measured along lines drawn across the nematodes injected with PBS (***d***), a PBS solution of **10** (***e***) or a PBS solution of **1e** (***f***) in the rectangular areas indicated in the corresponding image. Each plot is the average of five lines parallel to the short axis of the rectangle and equally spaced along the long axis.

The ability of **2c** to immunolabel biological preparations can be assessed with the aid of Alexa Fluor® 647-conjugated affinipure goat anti-mouse IgG (H+L). This model bioconjugate incorporates the very same secondary antibody of **2c** and is known to associate with *anti*-α-tubulin to allow the imaging of tubulin filaments in a variety of cell lines.[300] Furthermore, the absorption and emission bands of the BODIPY fluorophores of **2c** and those of the alexa dyes of the model system are sufficiently resolved across the visible region of the electromagnetic spectrum (Figure 5.8) to permit the imaging of both in separate detection channels. As a result, cells can be labeled with the two conjugates simultaneously and their localization probed independently. Specifically, images of HeLa

cells treated with both bioconjugates show the BODIPY fluorescence in one channel (***a*** in Figure 5.9) and alexa emission in the other (***b*** in Figure 5.9). Both images reveal the characteristic shape of the tubulin filaments and an overlay (***c*** in Figure 5.9) of the two clearly shows the co-localization of the two sets of probes. These observations demonstrate that the conjugation of the macromolecular probe to the antibody does not affect the ability of the biomolecule to associate selectively with its target and that such antibody–polymer construct can, indeed, be employed to label and visualize biological preparations.

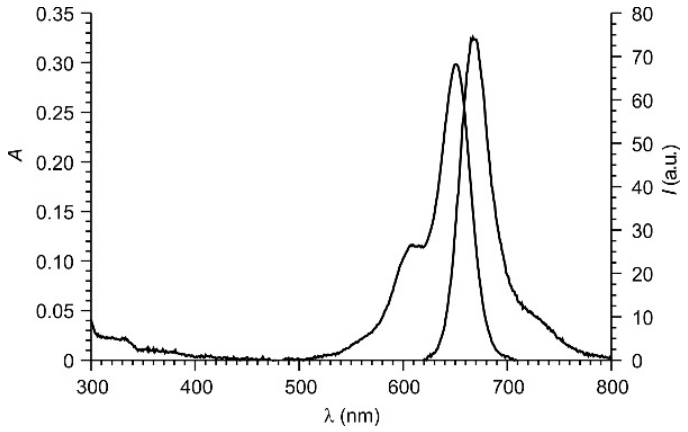

Figure 5.8 Absorption and emission spectra (30 μg mL^{-1}, λ_{Ex} = 610 nm) of alexa Fluor® 647-conjugated affinipure Goat anti-mouse IgG (H+L) in PBS at 25 °C.

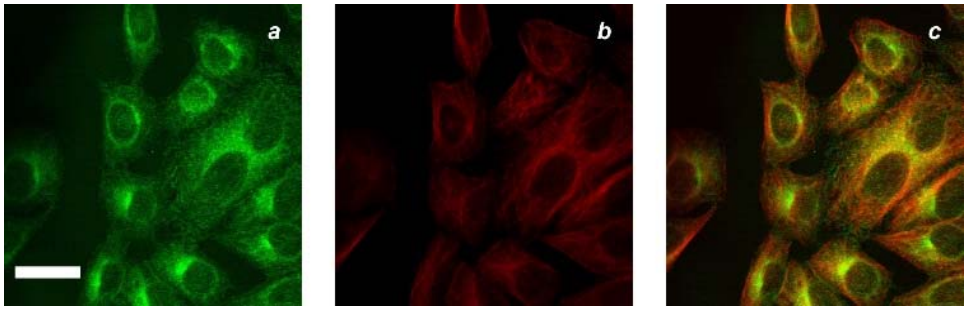

Figure 5.9 Fluorescence images (scale bar = 100 μm) of HeLa cells, immunolabeled with **2c** and Alexa Fluor® 647-conjugated affinipure goat anti-mouse IgG (H+L), recorded with either a λ_{Ex} of 514 nm and a detection window of 530–650 nm (***a***) or a λ_{Ex} of 633 nm and a detection window of 650–750 nm (***b***) together with an overlay (***c***) of the two frames.

5.4. Conclusions

Multiple BODIPY chromophores can be appended to a common poly(methacrylate) backbone together with decyl and oligo(ethylene glycol) side chains. The hydrophobic decyl components isolate the fluorophores effectively from each other, preventing interchromophoric interactions. As a result, the fluorescence quantum yield of these macromolecular constructs remains relatively high and is comparable to that of a model BODIPY monomer. In turn, the hydrophilic components ensure solubility in aqueous environment, where the photophysical properties of the emissive species are, once again, preserved by the effective insulation of the hydrophobic side chains. The presence of multiple chromophoric units, however, enhances the molar absorption coefficient significantly and translates into a three-fold increase in brightness, relative to the model BODIPY. Such macromolecular probes can be microinjected into living nematodes, where they retain their characteristic brightness levels and allow the visualization of the organisms with signal-to-noise ratios greater than those accessible with the model monomer. Furthermore, the fluorescent polymers do not have any significant effects on the behavior of the living organisms. The architecture of these macromolecular assemblies can be modified to permit the subsequent conjugation of antibodies and enable the immunolabeling of biological preparations. Specifically, carboxylic acids can be appended to the termini of some of the hydrophilic chains and then connected to the primary amino groups of a secondary antibody. Comparison of the resulting antibody conjugates to model systems demonstrate that the biomolecules retain their ability to bind their complementary targets and allow the visualization of the tubulin filaments of model cells with optimal signal-to-noise ratios. In summary, these particular structural designs for the covalent

integration of multiple fluorescent chromophores into the same construct provide (1) brightness levels greater than those accessible with conventional fluorophores, (2) allow the imaging of living organisms and (3) enable the immunolabeling of model biological preparations. Thus, a general strategy for the assembly of macromolecular probes with optimal photophysical properties and targeting capabilities for bioimaging applications can ultimately evolve from these investigations.

5.5. Experimental section

5.5.1. Materials and methods

Chemicals were purchased from commercial sources and used as received with the exception of THF, which was distilled over Na and benzophenone, and H_2O, which was purified with a Barnstead International NANOpure DIamond Analytical system. Compounds **3**–**5**, **10**, **12** and **14** were prepared according to literature procedures.[112,148,273,301] The synthesis of **6** and **8** are illustrated in Figures 5.10 and 5.11. GPC was performed with a Phenomenex Phenogel 5-μm MXM column (7.8 × 300 mm) operated with a Shimadzu Nexera X2 system in THF at a flow rate of 1.0 mL min^{-1}. Monodisperse polystyrene standards (2.7–200.0 kDa) were employed to determine the $\bar{M}_n$ and $Đ$ of the polymers from the GPC traces, following a literature protocol.[274] EISMS was performed with a Bruker micrOTO-Q II spectrometer. NMR spectra were recorded with a Bruker Avance 500 spectrometer. DLS measurements were performed with a Malvern ZEN1600 apparatus. The values listed for d_H in Table 5.1 are averaged over ten independent experiments of ten runs of 10 s each. Absorption spectra were recorded with a Varian Cary 100 Bio spectrometer, using quartz cells with a path length of 1.0 cm. Emission spectra were recorded with a Varian Cary Eclipse spectrometer in aerated

solutions. Fluorescence quantum yields were determined with a fluorescein standard, following a literature protocol.[302] Fluorescence images were recorded with a Leica SP5 confocal laser-scanning microscope.

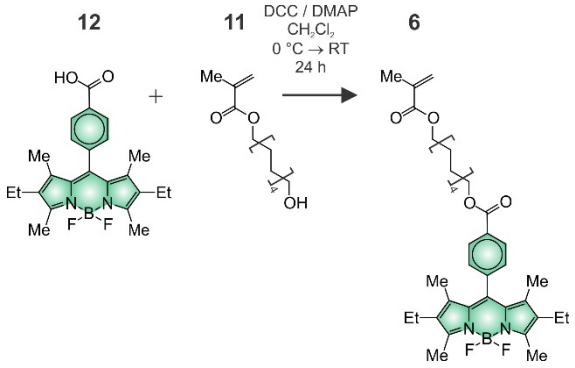

Figure 5.10 Synthesis of **6**.

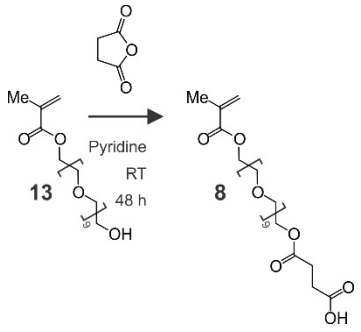

Figure 5.11 Synthesis of **8**.

5.5.2. General procedure for the synthesis of 1a–e

A solution of **3** (23.2 mg, 0.05 mmol), **4** (40.9 mg, 0.18 mmol for ***a***; 56.8 mg, 0.25 mmol for ***b***; 40.9 mg, 0.18 mmol for ***c***; 18.2 mg, 0.08 mmol for ***d***; 68.1 mg, 0.3 mmol for ***e***), **5** (540 mg, 0.27 mmol for ***a***; 540 mg, 0.27 mmol for ***b***; 340 mg, 0.17 mmol for ***c***; 280 mg, 0.14 mmol for ***d***; 300 mg, 0.15 mmol for ***e***) and AIBN (4.9 mg, 0.03 mmol) in degassed THF (8 mL) was heated for 72 hours at 75 °C under Ar in a sealed vial. After cooling down to ambient temperature, the reaction mixture was transferred to a centrifuge tube and

diluted with THF to a total volume of 10 mL. Hexane was added in portions of 1 mL and the tube was shaken vigorously, after each addition, until the formation of a precipitate was clearly observed. After centrifugation, the oily layer at the bottom of the tube was separated from the supernatant and dissolved in THF (10 mL). The treatment with hexane, followed by centrifugation, was repeated 3 times and the final oily residue was dried under reduced pressure to give **1** (90 mg for ***a***; 100 mg for ***b***; 65 mg for ***c***; 39 mg for ***d***; 48 mg for ***e***) as a red solid.

1a: GPC: $\bar{M}_n$ = 14.0 kDa, $Đ$ = 1.42; ^{1}H NMR (CD_2Cl_2): δ = 0.82–0.95 (19H, m), 0.96–1.18 (17H, m), 1.20–1.46 (58H, m), 1.54–1.74 (15H, m), 1.76–2.06 (11H, m), 2.09–2.16 (4H, m), 2.33 (4H, bs), 2.44–2.56 (6H, m), 3.36 (15H, s), 3.39–3.82 (702H, m), 3.86–4.25 (16H, m), 7.18–7.42 (4H, m).

1b: GPC: $\bar{M}_n$ = 21.8 kDa, $Đ$ = 1.90; ^{1}H NMR (CD_2Cl_2): δ = 0.81–0.96 (13H, m), 0.96–1.19 (15H, m), 1.21–1.48 (45H, m), 1.54–2.22 (34H, m), 2.34 (3H, s), 2.50 (4H, s), 3.36 (12H, s), 3.41–3.86 (551H, m), 3.88–4.35 (17H, m), 7.18–7.44 (4H. m).

1c: GPC: $\bar{M}_n$ = 17.9 kDa, $Đ$ = 1.69; ^{1}H NMR ($CDCl_3$): δ = 0.75–0.90 (28H, m), 0.94–1.02 (20H, m), 1.18–1.38 (106H, m), 1.55–1.66 (16H, m), 1.68–1.92 (20H, m), 2.29 (8H, bs), 2.45–2.57 (14H, m), 3.37 (23H, s), 3.52–3.74 (1024H, m), 3.89–4.20 (23H, m), 7.16–7.24 (4H, m).

1d: GPC: $\bar{M}_n$ = 16.4 kDa, $Đ$ = 1.53; ^{1}H NMR (CD_2Cl_2): δ = 0.81–0.96 (6H, m), 0.97–1.05 (4H, m), 1.19–1.46 (23H, m), 1.65 (4H, bs), 2.14 (2H, s), 2.20–2.40 (4H, m), 2.44–2.56 6H, m), 3.36 (3H, s), 3.41–3.82 (187H, m), 3.90–4.22 (64H, m), 7.19–7.41 (4H, m).

1e: GPC: $\overline{M}_n$ = 24.9 kDa, $Đ$ = 2.34; ^{1}H NMR (CD_2Cl_2): δ = 0.81–0.95 (18H, m), 0.96–1.09 (11H, m), 1.19–1.48 (63H, m), 1.65 (9H, bs), 1.72–1.86 (6H, m), 2.23–2.42 (5H, m), 2.51 (5H, bs), 3.36 (5H, s), 3.43–3.82 (254H, m), 3.86–4.24 (11H, m), 7.22–7.38 (4H, m).

5.5.3. General procedure for the synthesis of 2a and 2b

A solution of 6 (100 mg, 0.15 mmol), 7 (225 mg, 0.45 mmol for a; 205 mg, 0.41 mmol for b) without (for a) or with 8 (29 mg, 0.03 mmol for b) and AIBN (5 mg, 0.03 mmol) in degassed THF (8 mL) was heated for 72 hours at 75 °C under Ar in a sealed vial. After cooling down to ambient temperature, the reaction mixture was transferred to a centrifuge tube and diluted with THF to a total volume of 10 mL. Hexane was added in portions of 1 mL and the tube was shaken vigorously, after each addition, until the formation of a precipitate was clearly observed. After centrifugation, the oily layer at the bottom of the tube was separated from the supernatant and dissolved in THF (10 mL). The treatment with hexane, followed by centrifugation, was repeated 3 times and the final oily residue was dried under reduced pressure to give **2** (100 mg for a; 110 mg for d) respectively as a red solid.

2a: GPC: $\overline{M}_n$ = 20.1 kDa, $Đ$ = 2.26; ^{1}H NMR ($CDCl_3$): δ = 0.80–0.91 (25H, m), 0.95–1.02 (11H, m), 1.25–1.30 (19H, m), 1.32–1.40 (15H, m), 1.58–1.65 (4H, m), 1.70–1.78 (4H, m), 1.80–1.90 (8H, m), 2.50–2.56 (6H, s), 3.38 (15H, s), 3.51–3.72 (158H, m), 3.85–3.96 (3H, m), 4.04–4.14 (10H, m), 4.32–4.40 (2H, m), 7.41 (2H, d, 8Hz), 8.18 (2H, d, 8 Hz).

2b: GPC: $\overline{M}_n$ = 15.8 kDa, $Đ$ = 2.36; ^{1}H NMR ($CDCl_3$): δ = 0.75–0.90 (7H, m), 0.92–1.05 (11H, m), 1.25 (7H, s), 1.28–1.38 (12H, m), 1.40–1.1.48 (3H, m), 1.55–1.62 (3H, m), 1.75–1.90 (14H, m), 2.25–2.35 (4H, m), 2.58 (6H, s), 2.60–2.67 (1H, m), 3.36 (10H, s), 3.55–

3.70 (113H, m), 3.78–3.82 (1H, m), 3.85–3.95(2H, m), 4.08 (7H, bs), 4.30–4.37 (2H, m), 7.39 (2H, d, 8Hz), 8.16 (2H, d, 8Hz).

5.5.4. Synthesis of 2c

A solution of DCC (19.3 mg, 0.09 mmol) in CH_2Cl_2 (2 mL) was added dropwise, over the course of 20 min, to a solution of **2b** (150 mg, 0.009 mmol), DMAP (2.2 mg, 0.1 mmol) and NHS (12.9 mg, 0.11 mmol) in CH_2Cl_2 (6 mL) maintained at 0 ^oC under Ar. The reaction mixture was allowed to warm up to ambient temperature and was stirred for 24 hours under these conditions. The resulting precipitate was filtered off and the solvent was distilled off under reduced pressure to afford a red oil (120 mg). ^1H NMR ($CDCl_3$): δ = 0.78–0.90 (7H, m), 0.92–1.05 (10H, m), 1.22–1.28 (10H, m), 1.30–1.40 (12H, m), 1.42–1.1.50 (3H, m), 1.55–1.65 (3H, m), 1.75–1.90 (13H, m), 2.23–2.34 (4H, m), 2.52 (6H, bs), 2.80–2.86(2H, m), 3.36 (10H, s), 3.55–3.70 (109H, m), 3.78–3.82 (1H, m), 3.85–3.95(2H, m), 4.04–4.15 (8H, m), 4.30–4.37 (2H, m), 7.39 (2H, d, 8Hz), 8.16 (2H, d, 8Hz). An aliquot (1.5 mg) of the residue was dissolved in PBS (100 μL) and combined with an aqueous solution of **9** (Jackson ImmunoResearch Inc. 115-005-003; 1 mg, 435 μL), whose pH was adjusted to 8.8 with BCB (1 M, 75 μL). The mixture was stirred for 1 hour at ambient temperature and purified by column chromatography (Sephadex G25, PBS). The collected fractions (0.4 mL each) were analyzed by absorption spectroscopy and those showing the characteristic absorption of the BODIPY chromophores at 528 nm were used for further spectroscopic and imaging experiments.

6: A solution of DCC (106.6 mg, 0.52 mmol) in CH_2Cl_2 (2 mL) was added dropwise, over the course of 20 min, to a solution of **11** (114 mg, 0.48 mmol), DMAP (12 mg, 0.1 mmol), and **12** (200 mg, 0.48 mmol) in CH_2Cl_2 (5 mL) maintained at 0 ^0C under Ar. The reaction

mixture was allowed to warm up to ambient temperature and was stirred for 24 hours under these conditions. The resulting precipitate was filtered off and the solvent was distilled off under reduced pressure. The residue was purified by column chromatography [SiO_2: hexane/ EtOAc (4:1, v/v)] to afford **6** (120 mg, 39%) as a red oil. ESIMS: *m/z* = 671.3783 $[M + Na]^+$ (*m/z* calcd. for $C_{38}H_{51}BF_2N_2O_4Na$ = 671.3808); ^1H NMR ($CDCl_3$): δ = 0.97 (6H, t, 8Hz), 1.27 (6H, s), 1.30–1.43 (10H, m), 1.45–1.52 (2H, m), 1.65–1.72 (2H, m), 1.78–1.85 (2H, m), 1.95 (3H, s), 2.28–2.234 (4H, q, 8Hz), 2.55 (6H, s), 4.13–4.17 (2H, t, 8Hz), 4.36–4.39 (2H, t, 8Hz), 5.55 (1H, s), 6.10 (1H, s), 7.40–7.42 (2H, d, 8Hz), 8.17–8.19 (2H, d, 8Hz); ^{13}C NMR ($CDCl_3$): δ 11.9, 12.5, 14.5, 14.7, 17.1, 17.8, 18.3, 18.9, 26.0, 28.6, 29.3, 29.4, 64.8, 65.5, 125.2, 128.6, 128.7, 130.1, 130.3, 130.9, 133.1, 136.5, 138.1, 138.7, 140.6, 154.2, 166.2, 167.6.

8: A solution of succinic anhydride (2.28 g, 22.8 mmol) and **13** (4.0 g, 7.6 mmol) in pyridine (21 mL) was stirred for 48 hours at ambient temperature. The solvent was distilled off under reduced pressure and the residue was purified by column chromatography [SiO_2: hexane/ EtOAc (3:2, v/v)] to afford **8** (3.2 g, 67%) as a colorless oil. ESIMS: *m/z* = 649.3031 $[M + Na]^+$ (*m/z* calcd. for $C_{28}H_{50}O_{15}Na$ = 649.3047); ^1H NMR (CDCl3): δ = 1.92 (3H, s), 2.62 (6H, bs), 3.55–3.72 (56H, m), 4.20–4.30 (5H, m), 5.55 (1H, s), 6.10 (1H, s).

11: A solution of DCC (1.3 g, 6.3 mmol) in CH_2Cl_2 (5 mL) was added dropwise, over the course of 20 min, to a solution of 1,10-decanediol (1.0 g, 5.7 mmol), DMAP (140 mg, 1.1 mmol) and methacrylic acid (494 mg, 5.7 mmol) in CH_2Cl_2 (5 mL) maintained at 0 °C under Ar. The reaction mixture was allowed to warm up to ambient temperature and stirred for 24 hours under these conditions. The resulting precipitate was filtered off and the solvent was distilled off under reduced pressure. The residue was purified by column

chromatography [SiO_2: hexane/ EtOAc (4:1, v/v)] to afford **11** (700 mg, 50%) as a colorless oil. ESIMS: *m/z* = 265.1780 $[M + Na]^+$ (*m/z* calcd. for $C_{14}H_{26}O_3Na$ = 265.1780); ^1H NMR ($CDCl_3$): 1.24–1.40 (12H m), 1.50–1.70 (6H, m), 1.92 (3H, s), 3.59–3.63(2H, t, 8Hz), 4.09–4.13(2H, t, 8Hz), 5.52 (1H, s), 6.07 (1H, s); ^{13}C NMR (CDCl3): δ = 17.8, 18.3, 18.9,25.7, 25.9, 28.6, 29.2, 29.4, 29.5, 32.8, 63.0, 64.8, 125.1, 136.5, 141.8, 154.0, 167.6, 173.8.

5.5.5. Nematode imaging

Caenorhabditis elegans strain KG1188 *lite-1(ce314)* strain was used for fluorescence imaging.[303] Microinjections were done using a Zeiss Axio Observer inverted microscope in age-matched adult hermaphrodites ~24 hours past the L4 stage as described.[304] Borosilicate glass needles were loaded with PBS or PBS solutions of **1e** (1.10 mg mL^{-1}) or **10** (0.12 mg mL^{-1}) by capillary action, and injections (~200 pL each) were performed into worm gonads. Worms were recovered in M9 buffer, mounted onto Nematode Growth Media agar chunks, and overlaid with a glass coverslip for imaging using a HC Plan-Apo 20x (0.7 NA) objective Leica SP5 laser-scanning confocal microscope as described.[305]

5.5.6. Cell imaging

HeLa cells were cultured in Dulbecco's modified Eagle's media supplemented with fetal bovine serum (10% v/v), penicillin (100 U mL^{-1}) and streptomycin (0.01% v/v) at 37 °C. Cells were fixed in MeOH (0.2 mL) at –20 °C for 15 min, washed with PBS (0.1 mL) three times and maintained in a PBS solution of bovine serum albumin (BSA, 10 mg mL^{-1}, 0.1 mL) for 30 min at ambient temperature. Then, PBS solutions of *anti*-α-tubulin antibody (mouse monoclonal antibody, DM1A, Sigma; 0.8 μg mL^{-1}, 0.1 mL) and BSA (10 mg mL^{-1}, 0.1 mL) were added to the extracellular matrix and the resulting sample was maintained for 1 hour at ambient temperature. Cells were washed a PBS solution of BSA (10 mg mL^{-}

^{1}, 0.1 mL) three times, incubated in a PBS solution (0.1 mL of 1% BSA) of **2c** (20 μL, 2 μg mL^{-1}) and Alexa Fluor® 647-conjugated affinipure g anti-mouse IgG (H+L) (100 μL, 3 μg mL^{-1}) for 1 hour at ambient temperature, washed with a PBS solution of BSA (10 mg mL^{-1}, 0.1 mL) a further three times and imaged with a Leica SP5 confocal laser-scanning microscope.

CHAPTER 6

FLUORESCENCE PATTERNING WITH MILD ILLUMINATION IN POLYMER FILMS OF PHOTOCLEAVABLE OXAZINES

6.1. Background

Irreversible chemical reactions often follow the photoexcitation of organic chromophores.[191] Although these photoinduced transformations are generally inefficient, their cumulative effect, over multiple excitation cycles, can gradually lead to the complete degradation of the absorbing species. The overall process, termed bleaching, restricts the exposure to exciting radiations that any chromophore can tolerate to relatively short times and can limit drastically the performance of fluorescent probes.[1] Indeed, the fluorescence of organic molecules eventually turns off irreversibly, because of bleaching, after a given number of excitation cycles. Nonetheless, certain imaging applications are actually designed to take advantage of bleaching, in order to control the spatial distribution of fluorescence within a sample of interest. Specifically, fluorescence recovery after photobleaching (FRAP) has become the protocol of choice to monitor dynamic events in a diversity of biological specimens.[306] A region of interest in a sample labeled with fluorescent molecules is irradiated at high intensity and for prolonged time until all fluorophores in the illuminated area bleach. At this point, fluorescence images of the entire specimen are collected sequentially to follow the translocation of intact fluorescent molecules from the non-bleached to the bleached area.

The sequence of events, designed into FRAP to probe dynamics in biological samples, can be adapted to imprint optically fluorescent patterns in synthetic materials instead.[307-311] Generally, a polymer film, doped with appropriate amounts of fluorescent chromophores, is deposited on a supporting substrate and illuminated at high intensities either with a

scanning laser or through a mask. The fluorophores exposed to the exciting radiation bleach, while those in the other portions of the sample remain intact. The subsequent reading of their fluorescence, therefore, offers the opportunity to image the pattern imprinted within the sample through bleaching. In fact, this relatively simple protocol to write and read information optically is a valuable alternative to methods based on photoswitchable dopants embedded in inert matrices.[312-322]

A stringent limitation of imaging and patterning protocols based on bleaching is that harsh illumination conditions are generally a must.[306] Indeed, high irradiation intensities for prolonged time are required to ensure the complete degradation of the fluorophores and switch fluorescence permanently off in the illuminated area. Furthermore, the presence of sufficient amounts of molecular oxygen is also often necessary to promote the degradation of the absorbing species. In principle, these significant shortcomings can be overcome by avoiding bleaching altogether and relying on photosensitive matrices instead of inert polymer films. Specifically, a photoresponsive polymer host could be engineered to undergo a photochemical transformation efficiently, even under mild illumination conditions, and quench the emission of entrapped fluorescent guests as a result. In order to explore the possible implementation of such operating principles, we designed a photoresponsive polymer based on the established photochemistry of photocleavable oxazines developed in our laboratory.[23,299,319] In this article, we report the synthesis of this macromolecular construct, the characterization of its photochemical properties and the fabrication of microscaled fluorescent patterns.

6.2. Results and discussion

6.2.1. Synthesis and structural characterization

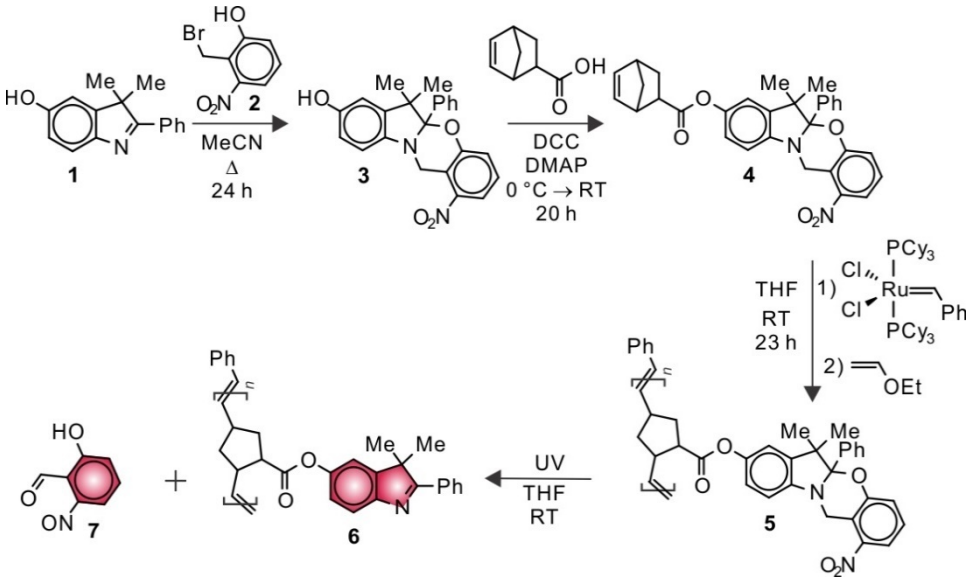

Figure 6.1 Synthesis of **5** and its photoinduced transformation into **6** and **7**.

The photoresponsive polymer was synthesized in three steps from known precursors (Figure 6.1). Specifically, reaction of **1** and **2** in acetonitrile, under reflux for 24 hours, produced **3** in a yield of 49%. Esterification of **3** with 5-norborene-2-carboxylic acid in dichloromethane at ambient temperature over 20 hours, under the assistance of *N*,*N*'-dicyclohexylcarbodiimide (DCC) and 4-dimethylaminopyridine (DMAP), generated **4** in a yield of 51%. Ring-opening polymerization of **4** in tetrahydrofuran (THF) at ambient temperature for 23 hours, under the influence of Grubbs' catalyst and after quenching with vinylethylether, afforded target macromolecule **5**. The structural identity of the synthetic intermediates was confirmed by electrospray ionization mass spectrometry (ESIMS), ^{1}H and ^{13}C nuclear magnetic resonance (NMR) spectroscopies. The final polymer was characterized by ^{1}H NMR spectroscopy and gel permeation chromatography (GPC). The

latter technique revealed the number-average molecular weight (M_n) and polydispersity index (PDI) of the polymer to be 16.3 kDa and 1.44 respectively.

6.2.2. Photochemical and photophysical properties

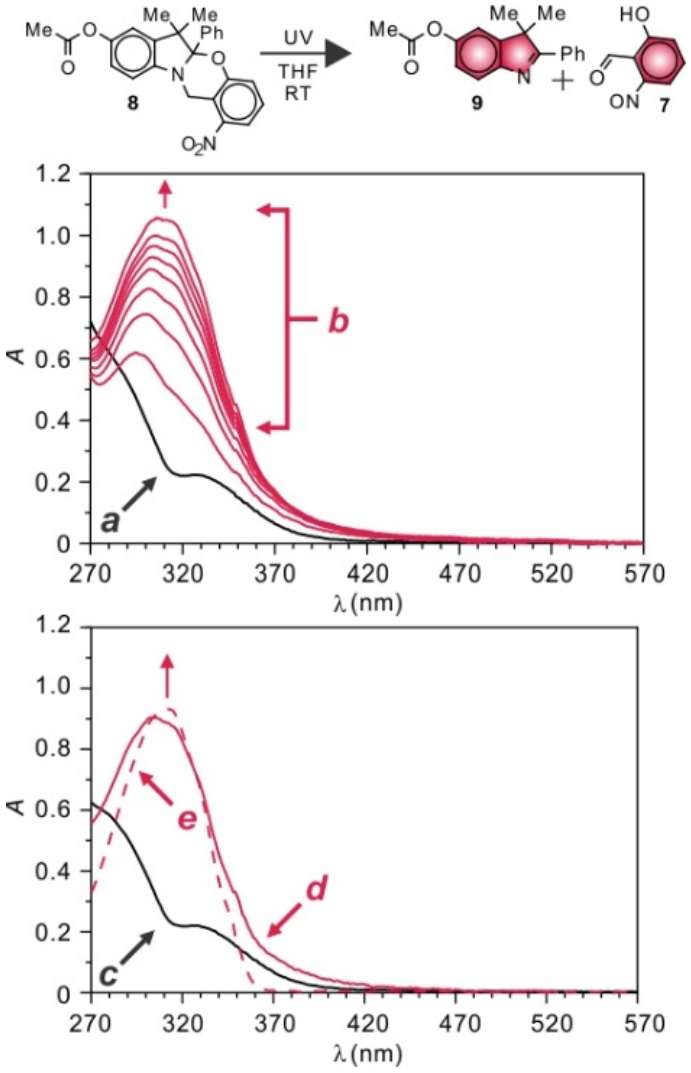

Figure 6.2 Absorption spectra of a THF solution of **5** (50 μg mL^{-1}) recorded before (***a***) and during (***b***) irradiation (350 nm, 4.3 mW cm^{-2}, 45 min). Absorption spectra of a THF solution of **8** (50 μM) recorded before (***c***) and after (***d***) irradiation (350 nm, 4.1 mW cm^{-2}, 45 min) together with normalized spectrum of **9** (***e***).

The absorption spectrum (***a*** in Figure 6.2) of **5** in THF shows a band at 327 nm for the 3-nitrophenoxy chromophore. Ultraviolet (UV) illumination of the sample induces the cleavage of the oxazine heterocycle with the formation of **6** and **7** (Figure 6.1). As a result,

the characteristic absorption of the 3*H*-indole chromophore of **6** develops at 311 nm (***b*** in Figure 6.2), during the course of the photolytic transformation. These spectral changes parallel those (***c*** and ***d*** in Figure 6.2) observed for the photoinduced conversion of **8** into **9** and **7**, under the same conditions and are consistent with literature data on related photocleavable oxazines.[23,299,319] Furthermore, the absorption spectrum (***e*** in Figure 6.2) of **9**, prepared independently from **1** (Figure 6.15), shows essentially the same band that develops during the photolysis of either **5** or **8**. The photoinduced formation of **7** and **9** from **8** is further confirmed by high-performance liquid chromatography (HPLC, Figure 6.3.), which indicates the quantum yield for this photochemical transformation to be 0.08. Additionally, the increase in absorbance at 311 nm (Figure 6.4.), observed with the photolysis of **8**, is remarkably similar to that recorded for **5**. These observations suggest that the attachment of multiple photocleavable oxazines to a common macromolecular backbone has negligible influence on the quantum efficiency of their photochemical transformation.

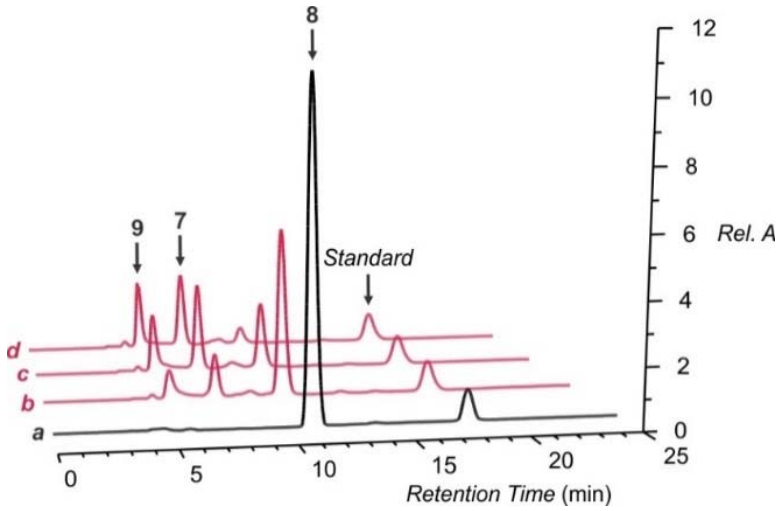

Figure 6.3 Chromatograms of a THF solution of **8** (0.2 mM) recorded before (***a***) and after irradiation (350 nm, 4.3 mW cm^{-2}) for 4 (***b***), 12 (***c***) and 25 min (***d***) against a standard **10**.

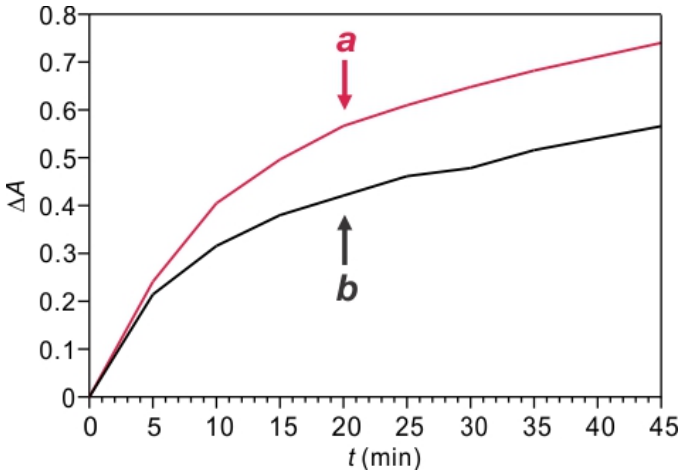

Figure 6.4 Absorbance evolution at 311 nm for THF solutions of **5** (***a***, 50 μg mL^{-1}) or **8** (***b***, 50 μM) during irradiation (350 nm, 4.3 mW cm^{-2}).

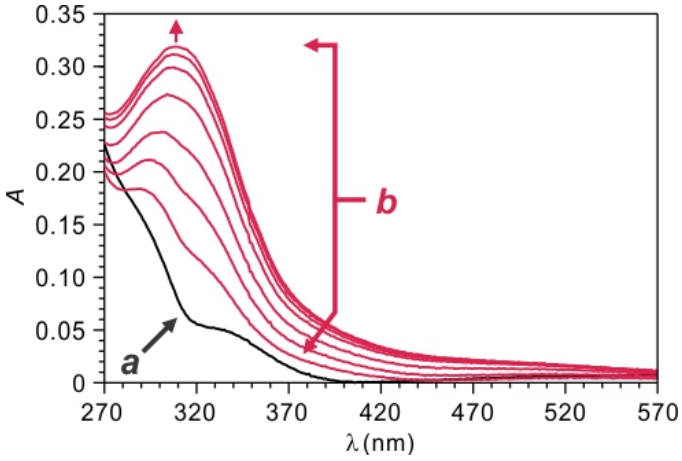

Figure 6.5 Absorption spectra of **5**, spin coated on quartz, recorded before (***a***) and during (***b***) irradiation (350 nm, 4.3 mW cm^{-2}, 50 min).

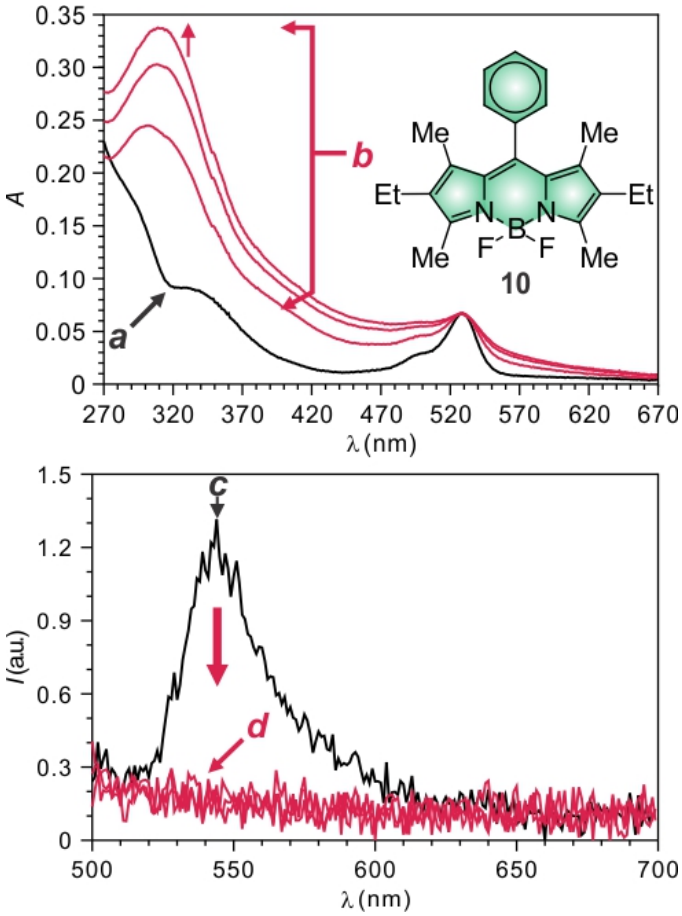

Figure 6.6 Absorption and emission (λ_{Ex} = 470 nm) spectra of **5**, spin coated on quartz and doped with **10** (10% w/w), recorded before (***a*** and ***c***) and during (***b*** and ***d***) irradiation (350 nm, 4.3 mW cm^{-2}, 50 min).

The photochemical transformation of the polymer occurs also in the absence of any solvent. Specifically, absorption spectra (Figure 6.5) of **5**, spin-coated on quartz, also reveal the developing absorption of the 3*H*-indole chromophore of **6**, upon illumination. Doping the polymer film with **10**, at a concentration of 10% w/w, has negligible influence on the photolytic transformation. The corresponding spectra (***a*** and ***b*** in Figure 6.6) show, once again, the developing absorbance of **6** at 312 nm together with an additional band at 529 nm for the BODIPY chromophore of **10**. Interestingly, the BODIPY absorbance remains unchanged during the course of the photochemical reaction. These observations indicate that the BODIPY chromophore (1) does not bleach, under the relatively mild illumination

conditions sufficient to convert **5** into **6** and **7** and (2) does not react with these photochemical products. Nonetheless, the characteristic fluorescence of the BODIPY dopant is completely suppressed with the photoinduced transformation of its polymer matrix. Indeed, the characteristic emission of **10** at 544 nm (***c*** and ***d*** in Figure 6.6) disappears with the conversion of **5** into **6** and **7**.[xxiii],[xxiv] This behavior suggests that **6** and/or **7** quench the excited state of **10** to prevent its radiative deactivation. In fact, comparison of the redox potentials of appropriate model compounds[23,319] suggests that electron transfer from the excited BODIPY chromophore to the nitroso group of **7** is exergonic with a free energy change of –0.45 eV. Consistently with this interpretation, the addition of increasing amounts of nitrosobenzene to a THF solution of **10** results in significant fluorescence quenching with a Stern-Volmer constant of 77.6 M^{-1} (Figure 6.7), while **9** has no influence on the emission of **10** under the same conditions. Furthermore, a control polymer (**11** in Figure 6.15) with the same macromolecular backbone of **5**, but lacking the photocleavable oxazine appendages, has negligible influence on the fluorescence of **10** (Figure 6.8), upon illumination. If a film of **11** is doped with a mixture of **8** and **10** instead, the fluorescence (Figure 6.9) of the BODIPY components is completely suppressed upon the photoinduced cleavage of the oxazine chromophores co-entrapped within the very same polymer matrix.

[xxiii] The concentration of **10** in films of **5** was varied systematically (1–50% w/w) to find that the largest fluorescence contrast is obtained at a dopant loading of 10% w/w. This particular value corresponds to a ratio between the number photocleavable oxazines and that of fluorescence BODIPYs of 54:1.

[xxiv] The fluorescence quantum yield of **10** in a film of **5** is 0.01 at a dopant concentration of 10% w/w.

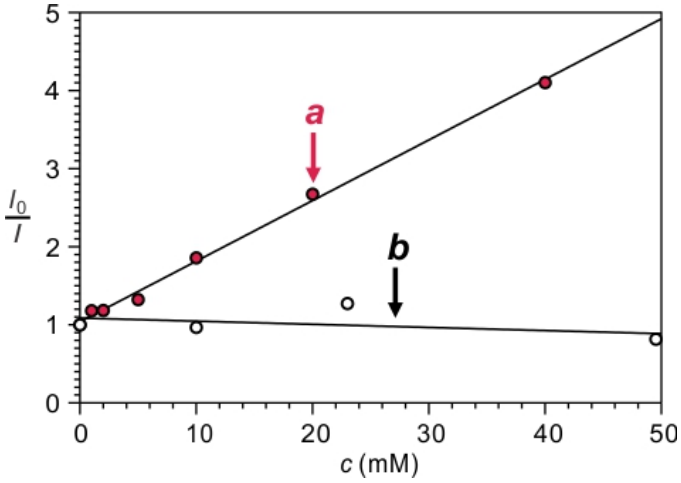

Figure 6.7 Plots of the relative emission intensity of **10** (1 μM, THF, 25 °C, λ_{Ex} = 470 nm) against the concentration of either nitrosobenzene (***a***) or **9** (***b***).

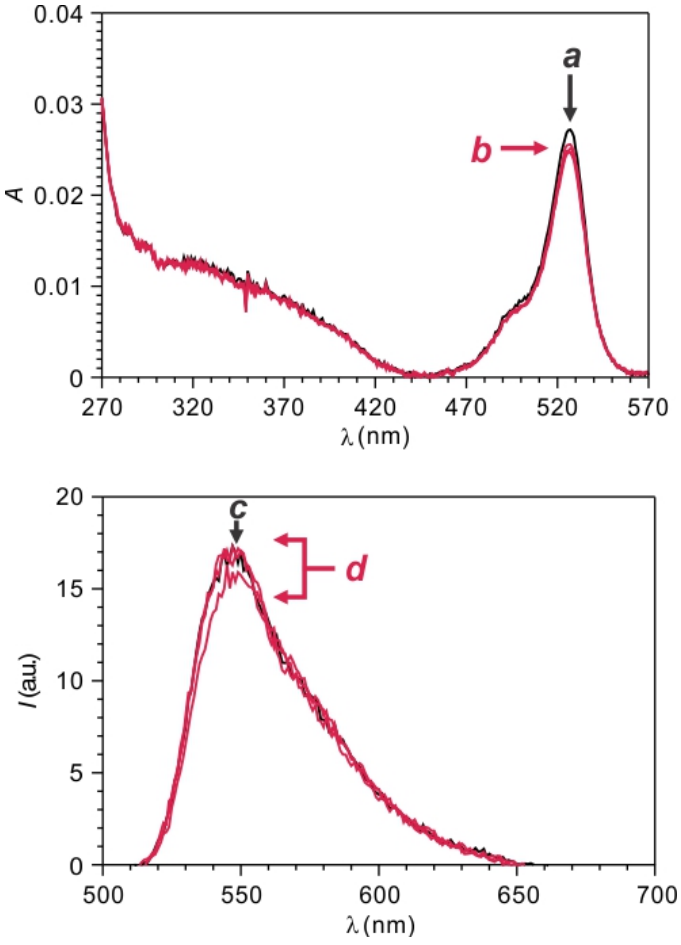

Figure 6.8 Absorption and emission (λ_{Ex} = 470 nm) spectra of **11**, spin coated on quartz and doped with **10** (10% w/w), recorded before (***a*** and ***c***) and during (***b*** and ***d***) irradiation (350 nm, 4.3 mW cm^{-2}, 35 min).

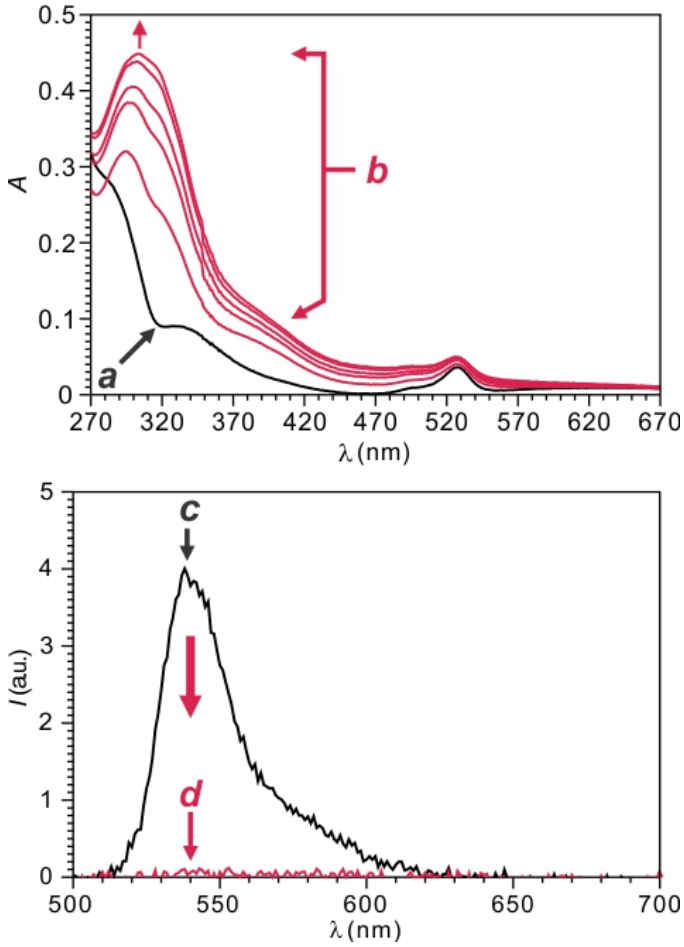

Figure 6.9 Absorption and emission (λ_{Ex} = 470 nm) spectra of **11**, spin coated on quartz and doped with **8** (80% w/w) and **10** (10% w/w), recorded before (***a*** and ***c***) and during (***b*** and ***d***) irradiation (350 nm, 4.3 mW cm^{-2}, 25 min).

6.2.2. Fluorescence patterning

The effective suppression of the dopant emission with the photoinduced transformation of its polymer matrix is also evident from fluorescence images (***a*** and ***b*** in Figure 6.10) recorded before and after illumination of a film of **5** doped with **10**. Specifically, laser irradiation (405 nm, 0.1 mW, 60 s) within a square at the center of the imaging field switches fluorescence off completely exclusively in the illuminated area. Such relatively mild illumination conditions have instead no influence on the fluorescence intensity of **10**, if this species is entrapped within the control polymer. In fact, images (Figure 6.11) of a

film of **11**, containing **10**, remain unchanged even after prolonged illumination, demonstrating that the BODIPY chromophore does not bleach at this laser power. Furthermore, the very same protocol for optical writing and reading can be extended to fluorophores other than **10**. Indeed, similar microscaled fluorescent patterns can be imprinted on films of **5** doped with rhodamine fluorophores (**13** in Figure 6.12) in place of **10**, under otherwise identical experimental conditions.

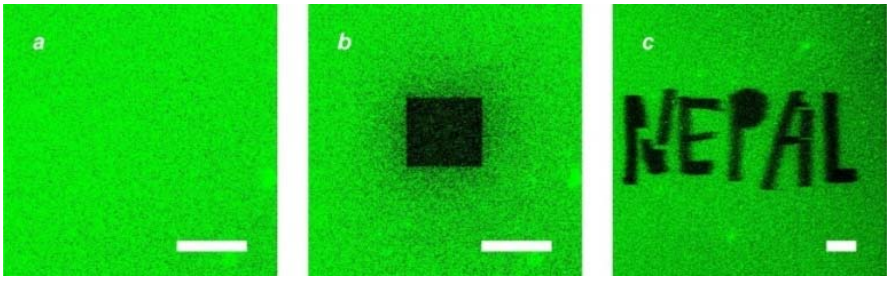

Figure 6.10 Confocal laser-scanning fluorescence images (λ_{Ex} = 514 nm, λ_{Em} = 525–600 nm, scale bar = 100 μm) of **5**, spin coated on glass and doped with **10** (10% w/w), recorded before (***a***) and after illumination (405 nm, 0.1 mW, ***b*** for 60 s and ***c*** for 20 s) of defined areas within the imaging field.

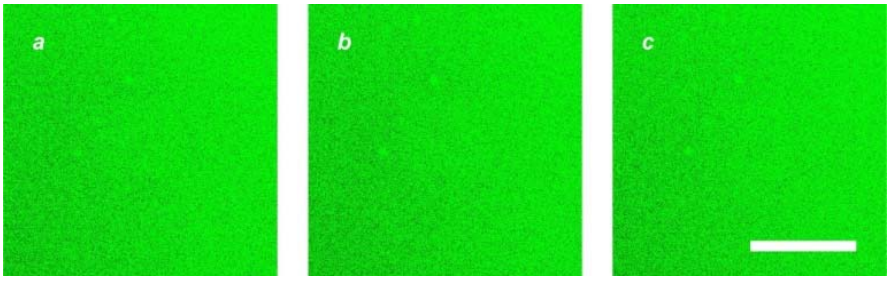

Figure 6.11 Confocal laser-scanning fluorescence images (λ_{Ex} = 514 nm, λ_{Em} = 525–600 nm, scale bar = 100 μm) of **11**, spin coated on glass and doped with **10** (10% w/w), recorded before (***a***) and either 60 (***b***) or 300 s (***c***) after illumination (405 nm, 0.1 mW) of defined areas within the imaging field.

The photochemical reaction responsible for fluorescence suppression results in the release of **7** from the polymer backbone. The diffusion of this species and of the fluorescent dopant within the polymer matrix can cause a gradual loss in the contrast of the imprinted patterns over prolonged periods of time. For example, a pattern of parallel lines can be imprinted

on a film of **5** doped with **10** (***a*** in Figure 6.13). After 120 s from patterning, the ratio between the average emission intensities measured in the bright and dark stripes is 5.5. After storing the substrate in the dark at ambient temperature, the pattern of parallel lines is still clearly visible (***b*** in Figure 6.13). However, the contrast decreases to 3.4, suggesting that **7** and/or **10** slowly redistribute across the polymer matrix under these experimental conditions.

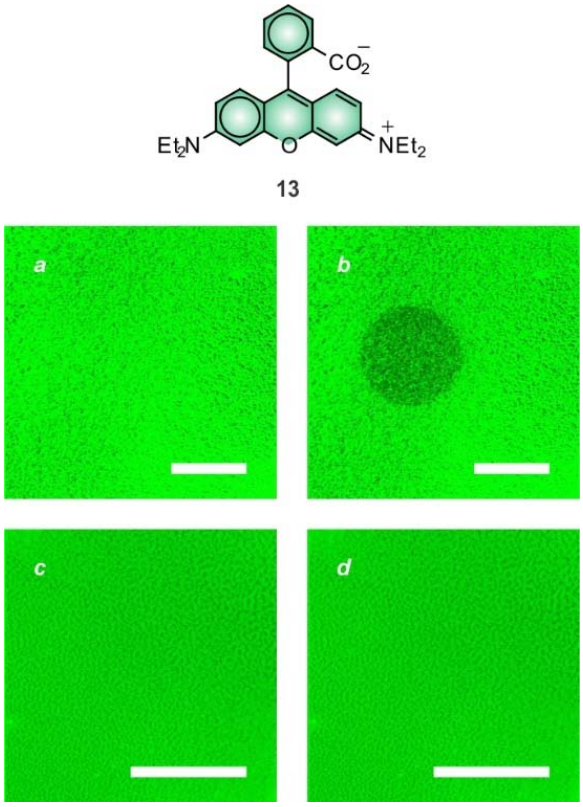

Figure 6.12 Confocal laser-scanning fluorescence images (λ_{Ex} = 514 nm, λ_{Em} = 520–650 nm, scale bar = 200 μm) of either **5** (***a*** and ***b***) or **11** (***c*** and ***d***), spin coated on glass and doped with **13** (10% w/w), recorded before (***a*** and ***c***) and 120 s (***b*** and ***d***) after illumination (405 nm, 0.1 mW) of defined areas within the imaging field.

The ability to turn fluorescence off within defined regions of the substrate, under optical control, offers the opportunity to imprint patterns with microscaled resolution. For example, text can be written across a film of **5**, doped with **10**, by scanning an illuminating

laser across the photoresponsive material and then it can be read by recording a fluorescence image of the substrate (***c*** in Figure 6.10). Alternatively, a microscaled mask can be deposited on the doped polymer film and then the entire substrate can be illuminated with an ultraviolet lamp. Under these conditions, fluorescence switches off exclusively in the exposed area and a copy of the mask is permanently imprinted in the film. For example, fluorescence images recorded with a copper grid over the film before ultraviolet exposure (Figure 6.14a) as well as after illumination and grid removal (Figure 6.14b) show that the final fluorescent pattern reproduces the shape of the original mask with optimal resolution.

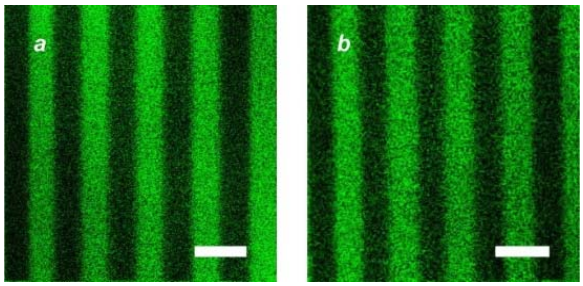

Figure 6.13 Confocal laser-scanning fluorescence images (λ_{Ex} = 514 nm, λ_{Em} = 525–600 nm, scale bar = 100 μm) of **5**, spin coated on glass and doped with **10** (10% w/w), recorded 120 s (***a***) and 24 hours (***b***) after illumination (405 nm, 0.1 mW) of defined areas within the imaging field.

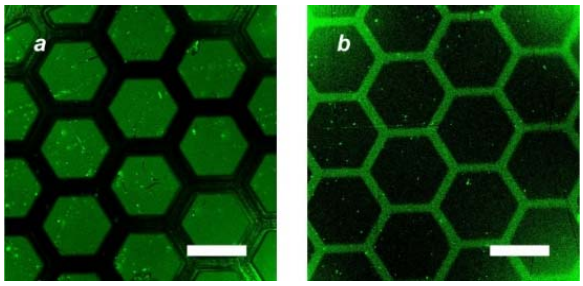

Figure 6.14 Confocal laser-scanning fluorescence images (λ_{Ex} = 514 nm, λ_{Em} = 525–600 nm, scale bar = 200 μm) of **5**, spin coated on glass and doped with **10** (10% w/w), recorded after covering the substrate with a microscaled grid (***a***), subsequent illumination (365 nm, 0.4 mW cm^{-2}) of the entire sample and removal of the grid (b).

6.3. Conclusions

Multiple photocleavable oxazines can be connected to a common macromolecular backbone relying on the ring-opening polymerization of appropriate monomers. The incorporation of these photoresponsive building blocks within the resulting macromolecular constructs has negligible influence of their photochemical and photophysical properties. Under mild illumination conditions, the many oxazine heterocycles cleave efficiently in organic solution as well as within spin-coated films. The latter materials can be doped with BODIPY fluorophores to ensure intense fluorescence, before the photoinduced cleavage of the oxazine rings. After their photochemical transformation, the resulting nitroso derivatives quench the fluorescence of the dopants, on the basis of photoinduced electron transfer, and turn emission permanently off in the illuminated areas. Therefore, patterned illumination of the sample either with a scanning laser or through a mask offers the opportunity to imprint optically patterns on the photoresponsive substrate that can be then read by acquiring a fluorescence image. Furthermore, the efficiency of the photochemical reaction of the photoresponsive matrix, entrapping the fluorescent dopant, permits the implementation of these operating principles for optical writing and reading with relatively low illumination intensities that are simply impossible to replicate with methods based exclusively on bleaching. Thus, the logic behind the design of these doped photoresponsive materials can evolve into a convenient strategy for the optical recording of information at the microscale.

6.4. Experimental section

6.4.1. Materials and methods

Chemicals were purchased from commercial sources and used as received with the exception of THF, which was distilled over Na and benzophenone. Compounds **1**, **2** and **10** were prepared following literature procedures.[23,270,299,323] ESIMS were recorded with a Bruker micrOTO-Q II spectrometer. NMR spectra were recorded with a Bruker Avance 400 spectrometer. GPC was performed with a Phenomenex Phenogel 5-μm MXM column (7.8 × 300 mm) operated with a Shimadzu Nexera X2 system in THF at a flow rate of 1.0 mL min^{-1}. Monodisperse polystyrene standard (2.7–2,000 kDa) were employed to determine M_n and PDI from the GPC traces, following a literature protocol.[324] Absorption spectra were recorded with a Varian Cary 100 Bio spectrometer. Measurements in solution were performed with quartz cells with a path length of 1.0 cm. Emission spectra were recorded with a Varian Cary Eclipse spectrometer. Measurements in solution were performed with aerated samples. Fluorescence quantum yields were measured against a fluorescein standard, according to an established procedure.[302] Photolyses were performed in aerated solutions with a Luzchem Research LZC-4V photoreactor (350 nm, 4.3 mW cm^{-2}), and the corresponding quantum yields were determined with a potassium ferrioxalate actinometer, according to an established procedure.[190] HPLC was performed with an Agilent Microsorb 100-5 BDS column (4.6 × 250 mm) operated with a Shimadzu Nexera X2 system in MeCN/H_2O (60:40, v/v) at a flow rate of 1.0 mL min^{-1} and detection wavelength of 250 nm. Fluorescence images were recorded with a Leica SP5 confocal laser-scanning microscope. Samples were irradiated through a microscaled Cu grid with a Mineralight UVGL-25 lamp (365 nm, 0.4 mW cm^{-2}).

3: A solution of **1** (500 mg, 2.1 mmol) and **2** (582 mg, 2.5 mmol) in MeCN was heated under reflux and Ar for 24 hours. After cooling down to ambient temperature, the solvent was distilled off under reduced pressure. The residue was dissolved in CH_2Cl_2 (20 mL) and washed with aqueous $NaHCO_3$ (5% w/v, 15 mL) and H_2O (2 × 15 mL). The solvent of the organic phase was distilled off under reduced pressure and the residue was purified by column chromatography [SiO_2: CH_2Cl_2/hexane (2:3, v/v)] to afford **3** (400 mg, 49%) as a yellow solid. ESIMS: *m/z* = 389.1494 $[M + H]^+$ (*m/z* calcd. for $C_{23}H_{20}N_2O_4$ = 388.1423); ^1H NMR ($CDCl_3$): δ = 0.83 (3H, s), 1.54 (3H, s), 4.41 (1H, bs), 4.72 (1H, d, 19 Hz), 4.99 (1H, d, 19 Hz), 6.53–6.63 (2H, m), 6.71 (1H, s), 7.10–7.21 (2H, m), 7.34–7.44 (3H, m), 7.60–7.69 (3H, m).

4: DCC (418 mg, 2.0 mmol) was added to a solution of **3** (350 mg, 0.9 mmol), 5-norborene-2-carboxylic acid (280 mg, 2.0 mmol) and DMAP (24.7 mg, 0.2 mmol) in CH_2Cl_2 (25 mL) maintained at 0 °C under Ar. The mixture was allowed to warm up to ambient temperature over the course of 20 hours. The solvent was distilled off under reduced pressure and the residue was purified by column chromatography [SiO_2: CH_2Cl_2/hexanes (1:4, v/v)] to afford **4** (233 mg, 51%) as a white solid. ESIMS: *m/z* = 554.2811 $[M + 2Na]^+$ (*m/z* calcd. for $C_{33}H_{32}N_2O_3$ = 508.1998); ^1H NMR ($CDCl_3$): δ = 0.82 (3H, s), 1.24–1.28 (1H, m), 1.32–1.38 (1H, m), 1.46–1.52 (1H, m), 1.54 (3H, s), 1.58–1.63 (1H, m), 1.95–2.10 (1H, m), 2.94–3.0 (1H, m), 3.15–3.22 (1H, m), 3.34–3.48 (1H, m), 4.73 (1H, d, 20 Hz), 5.01 (1H, d, 20 Hz), 6.04–6.09 (1H, m), 6.15–6.28 (1H, m), 6.61–6.68 (1H, m), 6.75–6.91 (2H, m), 7.08–7.21 (2H, m), 7.32–7.44 (3H, m), 7.60–7.68 (3H, m); ^{13}C NMR ($CDCl_3$): δ = 39.7, 34.0, 42.6, 43.5, 46.0, 46.8, 49.7, 103.6, 116.8, 117.5, 128.6, 128.9, 132.2, 135.6, 138.8, 144.5, 144.8, 147.3, 154.6, 173.8, 175.3.

5: A solution of benzylidenebis(tricyclohexylphosphine)dichloro-ruthenium (4 mg, 0.005 mmol) in THF (4 mL) was added to a solution of **4** (60 mg, 0.12 mmol) in THF (2 mL) maintained under Ar at ambient temperature. After 23 hours, vinyl ethyl ether (1 mL, 10.5 mmol) was added and the mixture was stirred for a further 30 min. The solvent was distilled off under reduced pressure and the residue was dissolved in THF (0.5 mL). The addition of MeCN (5 mL) caused the precipitation of a white solid, which was filtered off after centrifugation to give **5** (20 mg). GPC: M_n = 16.3 kDa, PDI = 1.44; ^{1}H NMR ($CDCl_3$): δ = 0.79 (3H, bs), 1.27 (1H, bs), 1.71–2.32 (3H, m), 4.72 (1H, d, 20 Hz), 5.01 (1H, d, 20 Hz), 5.27–5.72 (2H, m), 6.49–6.90 (3H, m), 7.11 (1H, bs), 7.31–7.45 (3H, m), 7.53–7.69 (3H, m).

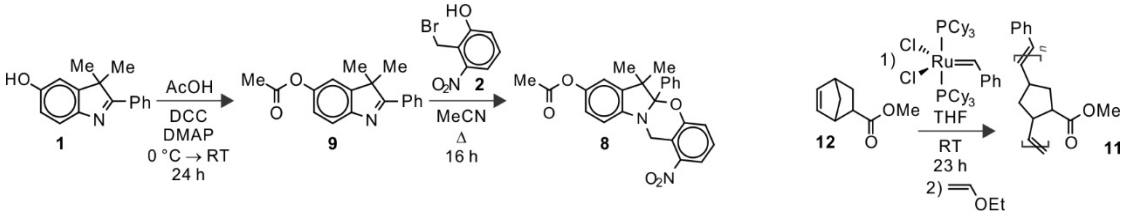

Figure 6.15 Synthesis of **8** and **11**.

8: A solution of **9** (80 mg, 0.29 mmol) and **2** (79.2 mg, 0.34 mmol) in MeCN was heated under reflux and Ar for 16 hours. After cooling down to ambient temperature, the solvent was distilled off under reduced pressure. The residue dissolved in CH_2Cl_2 (20 mL) and washed with aqueous $NaHCO_3$ (5% w/v, 15 mL) and H_2O (2 × 15 mL). The solvent of the organic phase was distilled off under reduced pressure and the residue was purified by column chromatography [SiO_2: EtOAc/hexane (1:5, v/v)] to afford **8** (64 mg, 52%) as a yellow solid. ESIMS: *m/z* = 431.1577 $[M + H]^+$ (*m/z* calcd. for $C_{25}H_{22}N_2O_5$ = 430.1529); ^{1}H NMR ($CDCl_3$): δ = 0.84 (3H, s), 1.55 (3H, s), 2.28 (3H, s), 4.75 (1H, d, 20 Hz), 5.02–5.06 (1H, d, 16 Hz), 6.68 (1H, d, 12 Hz), 6.84–6.91(2H, m), 7.13–7.23(2H, m), 7.34–7.45

(3H, m), 7.65 (3H, dd, 8Hz); ^{13}C NMR ($CDCl_3$): δ = 21.0, 27.3, 39.9, 49.7, 103.5, 116.1, 116.3, 116.9, 117.6, 128.1, 128.4, 128.9, 135.6, 138.8, 144.7, 144.8, 147.3, 154.7, 170.0.

9: DCC (95.3 mg, 0.46 mmol) was added to a solution of **1** (100 mg, 0.42 mmol), glacial acetic acid (28 mg, 0.46 mmol) and DMAP (10.2 mg, 0.08 mmol) in CH_2Cl_2 (25 mL) maintained at 0 °C under Ar. The mixture was allowed to warm up to ambient temperature over the course of 24 hours. The solvent was distilled off under reduced pressure and the residue was purified by column chromatography [SiO_2: EtOAc/hexane (1:4, v/v)] to afford **9** (90 mg, 77 %) as a white solid. ESIMS: *m/z* = 280.1347 $[M + H]^+$ (*m/z* calcd. for $C_{18}H_{17}NO_2$ = 279.1259); ^{1}H NMR ($CDCl_3$): δ = 1.69 (6H, s), 2.35 (3H, s), 7.06–7.11 (2H, m), 7.48–7.52 (3H, m), 7.68 (1H, d, 8 Hz), 8.11–8.16 (2H, m); ^{13}C NMR ($CDCl_3$): δ = 21.2, 24.8, 24.9, 54.0, 114.7, 114.8, 120.8, 121.0, 121.3, 128.1, 128.4, 128.6, 130., 133.1, 148.8, 149.0, 150.7, 169.7, 183.6.

11: A solution of benzylidenebis(tricyclohexylphosphine)dichloro-ruthenium (26.8 mg, 0.03 mmol) in THF (1 mL) was added to a solution of **12** (150 mg, 0.98 mmol) in THF (5 mL) maintained under Ar at ambient temperature. After 24 hours, vinyl ethyl ether (2 mL, 21 mmol) was added and the mixture was stirred for a further 30 min. The solvent was distilled off under reduced pressure and the residue was dissolved in THF (0.5 mL). The addition of MeCN (5 mL) caused the precipitation of a white solid, which was filtered off after centrifugation to give **11** (80 mg). GPC: M_n = 9.5 kDa, PDI = 1.61; ^{1}H NMR ($CDCl_3$): δ = 1.07–1.46 (1H, m), 1.62–2.13(3H, m), 2.33–3.22 (3H, m), 5.07–5.55 (2H, m).

6.4.2. Preparation of Polymer films

Solutions of either **5** or **11** (10 mg mL^{-1}) with and without **10**, **12** or **13** (0.1 mg mL^{-1}) in CH_2Cl_2 (0.2 mL) were deposited dropwise on either glass or quartz slides over 30 s, while

the substrates were spun at 1,100 rpm with a Chemat Technologies KW-4A spin coater. The coated slides were spun at the same speed for a further 60 s, stored under reduced pressure for 1 hour and then used for the spectroscopic and imaging experiments.

References and Notes

(1) Lakowicz, J. R. *Principles of Fluorescence Spectroscopy*; Springer: New York, 2006.

(2) Murphy, D. B. *Fundamentals of Light Microscopy and Electronic Imaging*; Wiley-Liss: New York, 2001.

(3) Terai, T.; Nagano, T. *Pflugers Arch., EJP*, **2013**, 465, 347.

(4) Escobedo, J. O.; Rusin, O.; Lim, S.; Strongin, R. M. *Curr. Opin. Chem. Biol.*, **2010**, 14, 64.

(5) Thompson, R. E.; Larson, D. R.; Webb, W. W. *Biophys. J.*, **2002**, 82, 2775.

(6) Lippincott-Schwartz, J.; Patterson, G. H. *Science*, **2003**, 300, 87.

(7) Shaner, N. C.; Patterson, G. H.; Davidson, M. W. *J. Cell Sci.*, **2007**, 120, 4247.

(8) Manley, S.; Gillette, J. M.; Lippincott-Schwartz, J. In *Methods in Enzymology, Vol 475: Single Molecule Tools, Pt B: Super-Resolution, Particle Tracking, Multiparameter, and Force Based Methods*; Walter, N. G., Ed., 2010.

(9) Lippincott-Schwartz, J. *Developmental Cell*, **2011**, 21, 5.

(10) Patterson, G. H. *J. Microsc.*, **2011**, 243, 1.

(11) Verkhusha, V. V.; Lukyanov, K. A. *Nat. Biotechnol.*, **2004**, 22, 289.

(12) Stepanenko, O. V.; Stepanenko, O. V.; Shcherbakova, D. M.; Kuznetsova, I. M.; Turoverov, K. K.; Verkhusha, V. V. *Biotechniques*, **2011**, 51, 313.

(13) Shcherbakova, D. M.; Subach, O. M.; Verkhusha, V. V. *Angewandte Chemie-International Edition*, **2012**, 51, 10724.

(14) Subach, F. V.; Verkhusha, V. V. *Chem. Rev.*, **2012**, 112, 4308.

(15) Wiedenmann, J.; Gayda, S.; Adam, V.; Oswald, F.; Nienhaus, K.; Bourgeois, D.; Nienhaus, G. U. *J. Biophotonics*, **2011**, 4, 377.

(16) Dedecker, P.; De Schryver, F. C.; Hofkens, J. *J. Am. Chem. Soc.*, **2013**, 135, 2387.

(17) Mitchison, T. J.; Sawin, K. E.; Theriot, J. A.; Gee, K.; Mallavarapu, A. *Methods Enzymol.*, **1998**, 291, 63.

(18) Wysocki, L. M.; Lavis, L. D. *Curr. Opin. Chem. Biol.*, **2011**, 15, 752.

(19) Li, W.-h.; Zheng, G. *Photochem. Photobiol. Sci.*, **2012**, 11, 460.

(20) Raymo, F. M. *ISRN Physical Chemistry*, **2012**, 2012, 15.

(21) Klan, P.; Solomek, T.; Bochet, C. G.; Blanc, A.; Givens, R.; Rubina, M.; Popik, V.; Kostikov, A.; Wirz, J. *Chem. Rev.*, **2013**, 113, 119.

(22) Kobayashi, T.; Komatsu, T.; Kamiya, M.; Campos, C.; Gonzalez-Gaitan, M.; Terai, T.; Hanaoka, K.; Nagano, T.; Urano, Y. *J. Am. Chem. Soc.*, **2012**, 134, 11153.

(23) Zhang, Y.; Swaminathan, S.; Tang, S.; Garcia-Amorós, J.; Boulina, M.; Captain, B.; Baker, J. D.; Raymo, F. M. *J. Am. Chem. Soc.*, **2015**, 137, 4709.

(24) Gagey, N.; Emond, M.; Neveu, P.; Benbrahim, C.; Goetz, B.; Aujard, I.; Baudin, J.-B.; Jullien, L. *Org. Lett.*, **2008**, 10, 2341.

(25) Gagey, N.; Neveu, P.; Jullien, L. *Angewandte Chemie-International Edition*, **2007**, 46, 2467.

(26) Orange, C.; Specht, A.; Puliti, D.; Sakr, E.; Furuta, T.; Winsor, B.; Goeldner, M. *Chem. Commun.*, **2008**, 1217.

(27) Zhao, Y. R.; Zheng, Q.; Dakin, K.; Xu, K.; Martinez, M. L.; Li, W. H. *J. Am. Chem. Soc.*, **2004**, 126, 4653.

(28) Zheng, G.; Cochella, L.; Liu, J.; Hobert, O.; Li, W.-h. *ACS Chem. Biol.*, **2011**, 6, 1332.

(29) Cusido, J.; Battal, M.; Deniz, E.; Yildiz, I.; Sortino, S.; Raymo, F. M. *Chem. Eur. J.*, **2012**, 18, 10399.

(30) Deniz, E.; Sortino, S.; Raymo, F. M. *J. Phys. Chem. Lett.*, **2010**, 1, 3506.

(31) Deniz, E.; Tomasulo, M.; Cusido, J.; Sortino, S.; Raymo, F. M. *Langmuir*, **2011**, 27, 11773.

(32) Deniz, E.; Tomasulo, M.; Cusido, J.; Yildiz, I.; Petriella, M.; Bossi, M. L.; Sortino, S.; Raymo, F. M. *J. Phys. Chem. C*, **2012**, 116, 6058.

(33) Deniz, E.; Kandoth, N.; Fraix, A.; Cardile, V.; Graziano, A. C. E.; Lo Furno, D.; Gref, R.; Raymo, F. M.; Sortino, S. *Chem. Eur. J.*, **2012**, 18, 15782.

(34) Swaminathan, S.; Petriella, M.; Deniz, E.; Cusido, J.; Baker, J. D.; Bossi, M. L.; Raymo, F. M. *J. Phys. Chem. A*, **2012**, 116, 9928.

(35) Duan, X.-Y.; Zhai, B.-C.; Song, Q.-H. *Photochem. Photobiol. Sci.*, **2012**, 11, 593.

(36) Jeong, Y. C.; Yang, S. I.; Ahn, K. H.; Kim, E. *Chem. Commun.*, **2005**, 2503.

(37) Jeong, Y.-C.; Yang, S. I.; Kim, E.; Ahn, K.-H. *Tetrahedron*, **2006**, 62, 5855.

(38) Uno, K.; Niikura, H.; Morimoto, M.; Ishibashi, Y.; Miyasaka, H.; Irie, M. *J. Am. Chem. Soc.*, **2011**, 133, 13558.

(39) Lord, S. J.; Conley, N. R.; Lee, H.-l. D.; Samuel, R.; Liu, N.; Twieg, R. J.; Moerner, W. E. *J. Am. Chem. Soc.*, **2008**, 130, 9204.

(40) Lord, S. J.; Conley, N. R.; Lee, H.-L. D.; Nishimura, S. Y.; Pomerantz, A. K.; Willets, K. A.; Lu, Z.; Wang, H.; Liu, N.; Samuel, R.et al. *Chemphyschem*, **2009**, 10, 55.

(41) Lee, H.-l. D.; Lord, S. J.; Iwanaga, S.; Zhan, K.; Xie, H.; Williams, J. C.; Wang, H.; Bowman, G. R.; Goley, E. D.; Shapiro, L.et al. *J. Am. Chem. Soc.*, **2010**, 132, 15099.

(42) Lord, S. J.; Lee, H.-l. D.; Samuel, R.; Weber, R.; Liu, N.; Conley, N. R.; Thompson, M. A.; Twieg, R. J.; Moerner, W. E. *J. Phys. Chem. B*, **2010**, 114, 14157.

(43) Krafft, G. A.; Sutton, W. R.; Cummings, R. T. *J. Am. Chem. Soc.*, **1988**, 110, 301.

(44) Mitchison, T. J. *J. Cell Biol.*, **1989**, 109, 637.

(45) Vincent, J. P.; Ofarrell, P. H. *Cell*, **1992**, 68, 923.

(46) Pellois, J. P.; Hahn, M. E.; Muir, T. W. *J. Am. Chem. Soc.*, **2004**, 126, 7170.

(47) Kobayashi, T.; Urano, Y.; Kamiya, M.; Ueno, T.; Kojima, H.; Nagano, T. *J. Am. Chem. Soc.*, **2007**, 129, 6696.

(48) Zheng, G.; Guo, Y.-M.; Li, W.-H. *J. Am. Chem. Soc.*, **2007**, 129, 10616.

(49) Maurel, D.; Banala, S.; Laroche, T.; Johnsson, K. *ACS Chem. Biol.*, **2010**, 5, 507.

(50) Yuan, L.; Lin, W.; Cao, Z.; Long, L.; Song, J. *Chem. Eur. J.*, **2011**, 17, 689.

(51) Ottl, J.; Gabriel, D.; Marriott, G. *Bioconjugate Chem.*, **1998**, 9, 143.

(52) Gee, K. R.; Weinberg, E. S.; Kozlowski, D. J. *Bioorg. Med. Chem. Lett.*, **2001**, 11, 2181.

(53) Foelling, J.; Belov, V.; Kunetsky, R.; Medda, R.; Schoenle, A.; Egner, A.; Eggeling, C.; Bossi, M.; Hell, S. W. *Angew. Chem. Int. Ed.*, **2007**, 46, 6266.

(54) Folling, J.; Belov, V.; Riedel, D.; Schoenle, A.; Egner, A.; Eggeling, C.; Bossi, M.; Hell, S. W. *Chemphyschem*, **2008**, 9, 321.

(55) Testa, I.; Schoenle, A.; Middendorff, C. V.; Geisler, C.; Medda, R.; Wurm, C. A.; Stiel, A. C.; Jakobs, S.; Bossi, M.; Eggeling, C.et al. *Opt. Express*, **2008**, 16, 21093.

(56) Belov, V. N.; Bossi, M. L.; Foelling, J.; Boyarskiy, V. P.; Hell, S. W. *Chem. Eur. J.*, **2009**, 15, 10762.

(57) Kolmakov, K.; Wurm, C.; Sednev, M. V.; Bossi, M. L.; Belov, V. N.; Hell, S. W. *Photochem. Photobiol. Sci.*, **2012**, 11, 522.

(58) Montenegro, H.; Di Paolo, M.; Capdevila, D.; Aramendia, P. F.; Bossi, M. L. *Photochem. Photobiol. Sci.*, **2012**, 11, 1081.

(59) Belov, V. N.; Wurm, C. A.; Boyarskiy, V. P.; Jakobs, S.; Hell, S. W. *Angew. Chem. Int. Ed.*, **2010**, 49, 3520.

(60) Wysocki, L. M.; Grimm, J. B.; Tkachuk, A. N.; Brown, T. A.; Betzig, E.; Lavis, L. D. *Angew. Chem. Int. Ed.*, **2011**, 50, 11206.

(61) Hu, D.; Tian, Z.; Wu, W.; Wan, W.; Li, A. D. Q. *J. Am. Chem. Soc.*, **2008**, 130, 15279.

(62) Tian, Z.; Li, A. D. Q.; Hu, D. *Chem. Commun.*, **2011**, 47, 1258.

(63) Aotake, T.; Tanimoto, H.; Hotta, H.; Kuzuhara, D.; Okujima, T.; Uno, H.; Yamada, H. *Chem. Commun.*, **2013**, 49, 3661.

(64) Aotake, T.; Yamashita, Y.; Okujima, T.; Shirasawa, N.; Jo, Y.; Fujimori, S.; Uno, H.; Ono, N.; Yamada, H. *Tetrahedron Lett.*, **2013**, 54, 1790.

(65) Peng, P.; Wang, C.; Shi, Z.; Johns, V. K.; Ma, L.; Oyer, J.; Copik, A.; Igarashi, R.; Liao, Y. *Org. Biomol. Chem.*, **2013**, 11, 6671.

(66) Thapaliya, E. R.; Captain, B.; Raymo, F. M. *J. Org. Chem.*, **2014**, 79, 3973.

(67) Thapaliya, E. R.; Swaminathan, S.; Captain, B.; Raymo, F. M. *J. Am. Chem. Soc.*, **2014**, 136, 13798.

(68) Dorion, G. H.; Wiebe, A. F. *Photochromism*; Focal Press: New York, 1970.

(69) Brown, G. H. *Photochromism*; Wiley: New York, 1971.

(70) Irie, M. *Chem. Rev.*, **2000**, 100, 1683.

(71) Favaro, G.; Irie, M. In *J. Photochem. Photobiol. C: Photochem. Rev.*, 2011.

(72) *Organic Photochromic and Thermochromic Compounds*; Crano, J. C.; Guglielmetti, R., Eds.; Plenum Press: New York, 1999.

(73) Kuz'min, M. G.; Koz'menko, M. V.; El'tsov, A. V., Ed.; Consultants Bureau: New York, 1990.

(74) Raymo, F. M.; Tomasulo, M. *Chem. Soc. Rev.*, **2005**, 34, 327.

(75) Yildiz, I.; Deniz, E.; Raymo, F. M. *Chem. Soc. Rev.*, **2009**, 38, 1859.

(76) Cusido, J.; Deniz, E.; Raymo, F. M. *Eur. J. Org. Chem.*, **2009**, 2009, 2031.

(77) Raymo, F. M.; Tomasulo, M. *The Journal of Physical Chemistry A*, **2005**, 109, 7343.

(78) Yun, C.; You, J.; Kim, J.; Huh, J.; Kim, E. *J. Photochem. Photobiol. C: Photochem. Rev.*, **2009**, 10, 111.

(79) Fukaminato, T. *J. Photochem. Photobiol. C: Photochem. Rev.*, **2011**, 12, 177.

(80) Halperin, A.; Tirrell, M.; Lodge, T. P. *Adv. Polym. Sci.*, **1992**, 100, 31.

(81) Lodge, T. P. *Macromol. Chem. Phys.*, **2003**, 204, 265.

(82) Moughton, A. O.; Hillmyer, M. A.; Lodge, T. P. *Macromolecules*, **2012**, 45, 2.

(83) Cameron, N. S.; Corbierre, M. K.; Eisenberg, A. *CAN J CHEM*, **1999**, 77, 1311.

(84) Webber, S. E. *J. Phys. Chem. B*, **1998**, 102, 2618.

(85) Riess, G. *Prog. Polym. Sci.*, **2003**, 28, 1107.

(86) Okhapkin, I. A.; Makhaeva, E. E.; Khokhlov, A. R. In *Conformation-Dependent Design of Sequences in Copolymers I*; Khokhlov, A. R., Ed., 2006.

(87) Kale, T. S.; Klaikherd, A.; Popere, B.; Thayumanavan, S. *Langmuir*, **2009**, 25, 9660.

(88) Owen, S. C.; Chan, D. P. Y.; Shoichet, M. S. *Nano Today*, **2012**, 7, 53.

(89) Garcia-Amorós, J.; Tang, S.; Zhang, Y.; Thapaliya, E. R.; Raymo, F. M. In *Light-Responsive Nanostructured Systems for Applications in Nanomedicine*; Sortino, S., Ed.; Springer International Publishing: Cham, 2016.

(90) Bader, H.; Ringsdorf, H.; Schmidt, B. *Angew. Makromol. Chem.*, **1984**, 123, 457.

(91) Kataoka, K.; Kwon, G. S.; Yokoyama, M.; Okano, T.; Sakurai, Y. *J. Controlled Release*, **1993**, 24, 119.

(92) Jones, M. C.; Leroux, J. C. *European Journal of Pharmaceutics and Biopharmaceutics*, **1999**, 48, 101.

(93) Torchilin, V. P. *J. Controlled Release*, **2001**, 73, 137.

(94) Adams, M. L.; Lavasanifar, A.; Kwon, G. S. *J. Pharm. Sci.*, **2003**, 92, 1343.

(95) Husseini, G. A.; Pitt, W. G. *Adv. Drug Deliv. Rev.*, **2008**, 60, 1137.

(96) Mondon, K.; Gurny, R.; Moeller, M. *Chimia*, **2008**, 62, 832.

(97) Park, J. H.; Lee, S.; Kim, J.-H.; Park, K.; Kim, K.; Kwon, I. C. *Prog. Polym. Sci.*, **2008**, 33, 113.

(98) Kim, S.; Shi, Y.; Kim, J. Y.; Park, K.; Cheng, J.-X. *Expert Opin. Drug Deliv.*, **2010**, 7, 49.

(99) Chacko, R. T.; Ventura, J.; Zhuang, J.; Thayumanavan, S. *Adv. Drug Deliv. Rev.*, **2012**, 64, 836.

(100) Lalatsa, A.; Schaetzlein, A. G.; Mazza, M.; Thi Bich Hang, L.; Uchegbu, I. F. *J. Controlled Release*, **2012**, 161, 523.

(101) Wang, Y.; Grayson, S. M. *Adv. Drug Deliv. Rev.*, **2012**, 64, 852.

(102) Lu, Y.; Park, K. *Int. J. Pharm.*, **2013**, 453, 198.

(103) Mura, S.; Nicolas, J.; Couvreur, P. *Nat. Mater.*, **2013**, 12, 991.

(104) Nicolas, J.; Mura, S.; Brambilla, D.; Mackiewicz, N.; Couvreur, P. *Chem. Soc. Rev.*, **2013**, 42, 1147.

(105) Tyler, J. Y.; Xu, X.-M.; Cheng, J.-X. *Nanoscale*, **2013**, 5, 8821.

(106) Wang, D.; Wang, X. *Prog. Polym. Sci.*, **2013**, 38, 271.

(107) Zhuang, J.; Gordon, M. R.; Ventura, J.; Li, L.; Thayumanavan, S. *Chem. Soc. Rev.*, **2013**, 42, 7421.

(108) Alakhova, D. Y.; Kabanov, A. V. *Mol. Pharm.*, **2014**, 11, 2566.

(109) Gu, L.; Faig, A.; Abdelhamid, D.; Uhrich, K. *Acc. Chem. Res.*, **2014**, 47, 2867.

(110) Makino, A. *Polym. J.*, **2014**, 46, 783.

(111) Swaminathan, S.; Fowley, C.; McCaughan, B.; Cusido, J.; Callan, J. F.; Raymo, F. M. *J. Am. Chem. Soc.*, **2014**, 136, 7907.

(112) Thapaliya, E. R.; Fowley, C.; Callan, B.; Tang, S.; Zhang, Y.; Callan, J. F.; Raymo, F. M. *Langmuir*, **2015**, 31, 9557.

(113) Tang, S.; Donaphon, B.; Levitus, M.; Raymo, F. M. *Langmuir*, **2016**, 32, 8676.

(114) Tang, S.; Zhang, Y.; Thapaliya, E. R.; Brown, A. S.; Wilson, J. N.; Raymo, F. M. *ACS Sensors*, **2017**, 2, 92.

(115) Lv, M.-Q.; Shi, Y.; Yang, W.-T.; Fu, Z.-F. *J. Appl. Polym. Sci.*, **2013**, 128, 332.

(116) Smeets, N. M. B. *Eur. Polym. J.*, **2013**, 49, 2528.

(117) Yildiz, I.; Impellizzeri, S.; Deniz, E.; McCaughan, B.; Callan, J. F.; Raymo, F. M. *J. Am. Chem. Soc.*, **2011**, 133, 871.

(118) van Oss, C. J. *Interfacial Forces in Aqueous Media (2nd. Ed.)*; CRC Press Taylor & Francis, Boca Raton (FL), 2006.

(119) Dukhin, S. S.; Kretzchmar, G.; Miller, B. *Dynamics of Adsorption at Liquid Interfaces*; Elsevier, Amsterdam, 1995.

(120) Hartley, G. S. *Trans. Faraday Soc.*, **1941**, 37, 130−133.

(121) Gray, G. W. *Handbook of Liquid Crystals*; Wiley-VCH: Weinheim, 1998.

(122) Figueiredo Neto, A. M.; Salinas, S. R. A. *The Physics of Lyotropic Liquid Crystals: Phase Transitions and Structural Properties*; Oxford University Press: Oxford, 2005.

(123) Garti, N.; Somasundaran, P.; R., M. *Self-Assembled Supramolecular Architectures: Lyotropic Liquid Crystals*; Wiley-VCH: Weinheim, 2012.

(124) Gelbart, W. M., Ben-Shaul, A. Roux, D. *Micelles, Membranes, Microemulsions, and Monolayers*; Springer-Verlag: New York, 1994.

(125) Hamley, I. W. *Introduction to Soft Matter: Synthetic and Biological Self-Assembling Materials*; WILEY-VCH: Chichester (UK), 2007.

(126) Forster, S.; Konrad, M. *J. Mater. Chem.*, **2003**, 13, 2671.

(127) Bucknall, D. G.; Anderson, H. L. *Science*, **2003**, 302, 1904.

(128) Zvelindovsky, A. V. *Nanostructured Soft Matter: Experiment, Theory, Simulation and Perspectives*; Springer: Dordrecht (NL), 2007.

(129) Torchilin, V.; Amiji, M. M. *Handbook of Materials for Nanomedicine*; Pan Stanford Publishing Pte. Ltd.: Singapore, 2010.

(130) Zhao, J.; Fung, B. M. *Langmuir*, **1993**, 9, 1228.

(131) Chakraborty, T.; Chakraborty, I.; Ghosh, S. *ARAB J CHEM*, **2011**, 4, 265.

(132) Al-Soufi, W.; Pineiro, L.; Novo, M. *J. Colloid Interface Sci.*, **2012**, 370, 102.

(133) Prazeres, T. J. V.; Beija, M.; Fernandes, F. V.; Marcelino, P. G. A.; Farinha, J. P. S.; Martinho, J. M. G. *Inorg. Chim. Acta*, **2012**, 381, 181.

(134) Topel, O.; Cakir, B. A.; Budama, L.; Hoda, N. *J. Mol. Liq.*, **2013**, 177, 40.

(135) Fendler, J. H. *Membrane Mimetic Chemistry*; Wiley-VCH: New York, 1982.

(136) Berthod, A.; Garcia-Alvarez-Coque, C., Ed.; Dekker: New York, 2000.

(137) Van Os, N. M., Haak, J. R., Rupert, L. A. M. *Physico-Chemical Properties of Selected Anionic, Cationic and Nonionic Surfactants*; Elsevier: Amsterdam, 1993.

(138) Armstrong, D. W. *Separation and Purification Methods*, **1985**, 14, 213.

(139) Kalyanasundaram, K.; Thomas, J. K. *J. Am. Chem. Soc.*, **1977**, 99, 2039.

(140) Ananthapadmanabhan, K. P.; Goddard, E. D.; Turro, N. J.; Kuo, P. L. *Langmuir*, **1985**, 1, 352.

(141) Aguiar, J.; Carpena, P.; Molina-Bolivar, J. A.; Ruiz, C. C. *J. Colloid Interface Sci.*, **2003**, 258, 116.

(142) Bhaisare, M. L.; Pandey, S.; Khan, M. S.; Talib, A.; Wu, H.-F. *Talanta*, **2015**, 132, 572.

(143) Berne, B. J.; Pecora, R. *Dynamic Light Scattering: with Applications to Chemistry, Biology, and Physics*; Courier Dover Publications: Mineola (NY), 2000.

(144) Jonasz, M.; Fournier, G. R. *Light Scattering by Particles in Water: Theoretical and Experimental Foundations*; Elsevier: San Diego (CA), 2007.

(145) Meurant, G. *Introduction to Dynamic Light Scattering by Macromolecules*; Academic Press, Inc.: London, 1990.

(146) Pecora, R. *Dynamic Light Scattering: Applications of Photon Correlation Spectroscopy*; Plenum Press: New York, 1985.

(147) Zetasizer Nano Series User Manual, Man0317, Issue 1.1, © Malvern Instruments Ltd., Malvern (UK), Feb. 2004.

(148) Zhang, Y.; Thapaliya, E. R.; Tang, S.; Baker, J. D.; Raymo, F. M. *RSC Advances*, **2016**, 6, 72756.

(149) Thapaliya, E. R.; Captain, B.; Raymo, F. M. *Asian J. Org. Chem.*, **2015**, 4, 233.

(150) Thapaliya, E. R.; Zhang, Y.; Raymo, F. M. *J. Mater. Chem. C*, **2017**, 5, 1179.

(151) Puliti, D.; Warther, D.; Orange, C.; Specht, A.; Goeldner, M. *Bioorg. Med. Chem.*, **2011**, 19, 1023.

(152) Raymo, F. M. *PCCP*, **2013**, 15, 14840.

(153) Adams, S. R.; Tsien, R. Y. *Annu. Rev. Physiol.*, **1993**, 55, 755.

(154) Politz, J. C. *Trends Cell Biol.*, **1999**, 9, 284.

(155) Dirks, R. W.; Molenaar, C.; Tanke, H. J. *Histochem. Cell Biol.*, **2001**, 115, 3.

(156) Xu, Y.; Melia, T. J.; Toomre, D. K. *Curr. Opin. Chem. Biol.*, **2011**, 15, 822.

(157) Ellis-Davies, G. C. R. *Nat. Methods*, **2007**, 4, 619.

(158) Hell, S. W. *Nat. Methods*, **2009**, 6, 24.

(159) Huang, B.; Bates, M.; Zhuang, X. In *Annu. Rev. Biochem*, 2009.

(160) Ha, T.; Tinnefeld, P. In *Annual Review of Physical Chemistry, Vol 63*; Johnson, M. A.;Martinez, T. J., Eds., 2012.

(161) Moerner, W. E. *J. Microsc.*, **2012**, 246, 213.

(162) van de Linde, S.; Heilemann, M.; Sauer, M. In *Annual Review of Physical Chemistry, Vol 63*; Johnson, M. A.;Martinez, T. J., Eds., 2012.

(163) Raymo, F. M. *J. Phys. Chem. Lett.*, **2012**, 3, 2379.

(164) Zweig, A.; Huffman, K. R.; Gallivan, J. B.; Orloff, M. K.; Halverso.F. *J. Am. Chem. Soc.*, **1974**, 96, 1449.

(165) Baro, J.; Dudek, D.; Luther, K.; Troe, J. *Z. Phys. Chem. Neue Folge*, **1984**, 140, 167.

(166) Zweig, A. *Pure Appl. Chem.*, **1973**, 33, 389.

(167) Strating, J. Z., B.; Wagenaar, A.; Udding, A. C. *Tetrahedron Lett.*, **1969**, 10, 125.

(168) Ihlemann, J. B., M.; Luther, K.; Troe, J. *Proc. SPIE*, **1991**, 1361, 1011.

(169) Mondal, R.; Shah, B. K.; Neckers, D. C. *J. Am. Chem. Soc.*, **2006**, 128, 9612.

(170) Mondal, R.; Adhikari, R. M.; Shah, B. K.; Neckers, D. C. *Org. Lett.*, **2007**, 9, 2505.

(171) Mondal, R.; Okhrimenko, A. N.; Shah, B. K.; Neckers, D. C. *J. Phys. Chem. B*, **2008**, 112, 11.

(172) Mondal, R.; Toenshoff, C.; Khon, D.; Neckers, D. C.; Bettinger, H. F. *J. Am. Chem. Soc.*, **2009**, 131, 14281.

(173) Zhao, Y.; Cai, X.; Danilov, E.; Li, G.; Neckers, D. C. *Photochem. Photobiol. Sci.*, **2009**, 8, 34.

(174) Bettinger, H. F.; Mondal, R.; Krasowska, M.; Neckers, D. C. *J. Org. Chem.*, **2013**, 78, 1851.

(175) Zhao, Y.; Mondal, R.; Neckers, D. C. *J. Org. Chem.*, **2008**, 73, 5506.

(176) Uno, H.; Yamashita, Y.; Kikuchi, M.; Watanabe, H.; Yamada, H.; Okujima, T.; Ogawa, T.; Ono, N. *Tetrahedron Lett.*, **2005**, 46, 1981.

(177) Yamada, H.; Yamashita, Y.; Kikuchi, M.; Watanabe, H.; Okujima, T.; Uno, H.; Ogawa, T.; Ohara, K.; Ono, N. *Chem. Eur. J.*, **2005**, 11, 6212.

(178) Yamada, H.; Kawamura, E.; Sakamoto, S.; Yamashita, Y.; Okujima, T.; Uno, H.; Ono, N. *Tetrahedron Lett.*, **2006**, 47, 7501.

(179) Masumoto, A.; Yamashita, Y.; Go, S.; Kikuchi, T.; Yamada, H.; Okujima, T.; Ono, N.; Uno, H. *Jpn. J. Appl. Phys*, **2009**, 48.

(180) Katsuta, S.; Yamada, H.; Okujima, T.; Uno, H. *Tetrahedron Lett.*, **2010**, 51, 1397.

(181) Yamada, H.; Kuzuhara, D.; Ohkubo, K.; Takahashi, T.; Okujima, T.; Uno, H.; Ono, N.; Fukuzumi, S. *J. Mater. Chem.*, **2010**, 20, 3011.

(182) Aotake, T.; Ikeda, S.; Kuzuhara, D.; Mori, S.; Okujima, T.; Uno, H.; Yamada, H. *Eur. J. Org. Chem.*, **2012**, 1723.

(183) Nozaki, H.; Kato, H.; Noyori, R. *Tetrahedron*, **1969**, 25, 1661.

(184) Atherton, J. C. C.; Jones, S. *Tetrahedron Lett.*, **2002**, 43, 9097.

(185) Adachi, Y.; Nakagawa, H.; Matsuo, K.; Suzuki, T.; Miyata, N. *Chem. Commun.*, **2008**, 5149.

(186) Matsuo, K.; Nakagawa, H.; Adachi, Y.; Kameda, E.; Tsumoto, H.; Suzuki, T.; Miyata, N. *Chem. Commun.*, **2010**, 46, 3788.

(187) Johns, V. K.; Shi, Z.; Dang, W.; McInnis, M. D.; Weng, Y.; Liao, Y. *J. Phys. Chem. A*, **2011**, 115, 8093.

(188) Rani, R.; Arya, S.; Kilaru, P.; Sondhi, S. M. *Green Chem. Lett. Rev.*, **2012**, 5, 545.

(189) Weber, E.; Finge, S.; Csoregh, I. *J. Org. Chem.*, **1991**, 56, 7281.

(190) Scaiano, J. C. *Handbook of Organic Photochemistry*; CRC Press: Florida, 1989.

(191) Turro, N. J.; Ramamurthy, V.; Scaiano, J. C. *Principles of Molecular Photochemistry: An Introduction*; University Science Books: Sausalito, 2009.

(192) Morris, J. V.; Mahaney, M. A.; Huber, J. R. *J. Phys. Chem.*, **1976**, 80, 969.

(193) Dawson, W. R.; Windsor, M. W. *J. Phys. Chem.*, **1968**, 72, 3251.

(194) Favaro, G.; di Nunzio, M. R.; Gentili, P. L.; Romani, A.; Becker, R. S. *J. Phys. Chem. A*, **2007**, 111, 5948.

(195) Zhou, X.; Piland, G. B.; Kurunthu, D.; Dillon, R. J.; Burdett, J. J.; Bardeen, C. J. *J. Lumin.*, **2012**, 132, 2997.

(196) Cai, H.; He, X. H.; Zheng, D. Y.; Qiu, J. A.; Li, Z. C.; Li, F. M. *J. Polym. Sci., Part A: Polym. Chem.*, **1996**, 34, 1245.

(197) Goichi, M.; Segawa, K.; Suzuki, S.; Toyota, S. *Synthesis-Stuttgart*, **2005**, 2116.

(198) Geiseler, O.; Mueller, M.; Podlech, J. *Tetrahedron*, **2013**, 69, 3683.

(199) Parr, R. G. Y., W. *Density-Functional Theory of Atoms and Molecules*; Oxford University Press: Oxford, 1989.

(200) Becke, A. D. *Phys. Rev. A* **1988**, 38, 3098.

(201) Lee, C. Y., W.; Parr, R. G. . *Phys. Rev. B* **1988**, 37, 785.

(202) Gaussian 09, Revision A.02, Frisch, M. J.; Trucks, G. W.; Schlegel, H. B.; Scuseria, G. E.; Robb, M. A.; Cheeseman, J. R.; Scalmani, G.; Barone, V.; Mennucci, B.; Petersson, G. A.; Nakatsuji, H.; Caricato, M.; Li, X.; Hratchian, H. P.; Izmaylov, A. F.; Bloino, J.; Zheng, G.; Sonnenberg, J. L.; Hada, M.; Ehara, M.; Toyota, K.; Fukuda, R.; Hasegawa, J.; Ishida, M.; Nakajima, T.; Honda, Y.; Kitao, O.; Nakai, H.; Vreven, T.; Montgomery, Jr., J. A.; Peralta, J. E.; Ogliaro, F.; Bearpark, M.; Heyd, J. J.; Brothers, E.; Kudin, K. N.; Staroverov, V. N.; Kobayashi, R.; Normand, J.; Raghavachari, K.; Rendell, A.; Burant, J. C.; Iyengar, S. S.; Tomasi, J.; Cossi, M.; Rega, N.; Millam, J. M.; Klene, M.; Knox, J. E.; Cross, J. B.; Bakken, V.; Adamo, C.; Jaramillo, J.; Gomperts, R.; Stratmann, R. E.; Yazyev, O.; Austin, A. J.; Cammi, R.; Pomelli, C.; Ochterski, J. W.; Martin, R. L.; Morokuma, K.; Zakrzewski, V. G.; Voth, G. A.; Salvador, P.; Dannenberg, J. J.; Dapprich, S.; Daniels, A. D.; Farkas, Ö.; Foresman, J. B.; Ortiz, J. V.; Cioslowski, J.; Fox, D. J. Gaussian, Inc., Wallingford CT, 2009.

(203) Tomasi, J. M., B.; Cammi, R. *Chem. Rev.*, **2005**, 105, 2999.

(204) Bissette, A. J.; Fletcher, S. P. *Angewandte Chemie-International Edition*, **2013**, 52, 12800.

(205) Von Kiedrowski, G. In *Bioorganic Chemistry Frontiers*; Dugas, H.;Schmidtchen, F. P., Eds.; Springer Berlin Heidelberg: Berlin, Heidelberg, 1993.

(206) Ruiz-Mirazo, K.; Briones, C.; de la Escosura, A. *Chem. Rev.*, **2014**, 114, 285.

(207) Hong, J. I.; Feng, Q.; Rotello, V.; Rebek, J. *Science*, **1992**, 255, 848.

(208) Kottani, R.; Majjigapu, J. R. R.; Kurchan, A.; Majjigapu, K.; Gustafson, T. P.; Kutateladze, A. G. *J. Am. Chem. Soc.*, **2006**, 128, 14794.

(209) Dadon, Z.; Samiappan, M.; Safranchik, E. Y.; Ashkenasy, G. *Chem. Eur. J.*, **2010**, 16, 12096.

(210) Samiappan, M.; Dadon, Z.; Ashkenasy, G. *Chem. Commun.*, **2011**, 47, 710.

(211) Dadon, Z.; Samiappan, M.; Wagner, N.; Ashkenasy, G. *Chem. Commun.*, **2012**, 48, 1419.

(212) Sella, E.; Lubelski, A.; Klafter, J.; Shabat, D. *J. Am. Chem. Soc.*, **2010**, 132, 3945.

(213) Vignoni, M.; Cabrerizo, F. M.; Lorente, C.; Claparols, C.; Oliveros, E.; Thomas, A. H. *Org. Biomol. Chem.*, **2010**, 8, 800.

(214) Dutta, S.; Mokhir, A. *Chem. Commun.*, **2011**, 47, 1243.

(215) Gustafson, T. P.; Metzel, G. A.; Kutateladze, A. G. *Org. Biomol. Chem.*, **2011**, 9, 4752.

(216) Gustafson, T. P.; Metzel, G. A.; Kutateladze, A. G. *Photochem. Photobiol. Sci.*, **2012**, 11, 564.

(217) Thomas, S. W.; Joly, G. D.; Swager, T. M. *Chem. Rev.*, **2007**, 107, 1339.

(218) Hyndman, H. L.; Monroe, B. M.; Hammond, G. S. *J. Am. Chem. Soc.*, **1969**, 91, 2852.

(219) Saltiel, J.; Townsend, D. E.; Sykes, A. *J. Am. Chem. Soc.*, **1973**, 95, 5968.

(220) Saltiel, J.; Zhang, Y. X.; Sears, D. F. *J. Am. Chem. Soc.*, **1997**, 119, 11202.

(221) Saltiel, J.; Wang, S. J.; Ko, D. H.; Gormin, D. A. *J. Phys. Chem. A*, **1998**, 102, 5383.

(222) Saltiel, J.; Crowder, J. M.; Wang, S. J. *J. Am. Chem. Soc.*, **1999**, 121, 895.

(223) Saltiel, J.; Dmitrenko, O.; Reischl, W.; Bach, R. D. *J. Phys. Chem. A*, **2001**, 105, 3934.

(224) Lechtken, P.; Yekta, A.; Turro, N. J. *J. Am. Chem. Soc.*, **1973**, 95, 3027.

(225) Turro, N. J.; Schore, N. E.; Steinmet.Hc; Yekta, A. *J. Am. Chem. Soc.*, **1974**, 96, 1936.

(226) Turro, N. J.; Waddell, W. H. *Tetrahedron Lett.*, **1975**, 2069.

(227) Lechtken, P.; Yekta, A.; Shore, N. E.; Steinmetzer, H. C.; Waddell, W. H.; Turro, N. J. *Z. Phys. Chem. Frankfurt*, **1976**, 101, 79.

(228) Turro, N. J.; Ramamurthy, V.; Katz, T. J. *New J. Chem.*, **1977**, 1, 363.

(229) Okamoto, H.; Arai, T.; Sakuragi, H.; Tokumaru, K.; Kawanishi, Y. *Bull. Chem. Soc. Jpn.*, **1991**, 64, 216.

(230) Karatsu, T.; Hiresaki, T.; Arai, T.; Sakuragi, H.; Tokumaru, K.; Wirz, J. *Bull. Chem. Soc. Jpn.*, **1991**, 64, 3355.

(231) Lednev, I. K.; Alfimov, M. V.; Kuriyama, Y.; Arai, T.; Sakuragi, H.; Tokumaru, K. *J. Photochem. Photobiol., A*, **1992**, 63, 201.

(232) Arai, T.; Furuya, Y.; Furuuchi, H.; Tokumaru, K. *Chem. Phys. Lett.*, **1993**, 212, 597.

(233) Karatsu, T.; Tsuchiya, M.; Arai, T.; Sakuragi, H.; Tokumaru, K. *Bull. Chem. Soc. Jpn.*, **1994**, 67, 3030.

(234) Tokumaru, K.; Arai, T. *Bull. Chem. Soc. Jpn.*, **1995**, 68, 1065.

(235) Merkel, P. B.; Roh, Y.; Dinnocenzo, J. P.; Robello, D. R.; Farid, S. *J. Phys. Chem. A*, **2007**, 111, 1188.

(236) Ferrar, L.; Mis, M.; Dinnocenzo, J. P.; Farid, S.; Merkel, P. B.; Robello, D. R. *J. Org. Chem.*, **2008**, 73, 5683.

(237) Kuzmanich, G.; Natarajan, A.; Chin, K. K.; Veerman, M.; Mortko, C. J.; Garcia-Garibay, M. A. *J. Am. Chem. Soc.*, **2008**, 130, 1140.

(238) Kuzmanich, G.; Gard, M. N.; Garcia-Garibay, M. A. *J. Am. Chem. Soc.*, **2009**, 131, 11606.

(239) Nielsen, A.; Kuzmanich, G.; Garcia-Garibay, M. A. *J. Phys. Chem. A*, **2014**, 118, 1858.

(240) Alvarez-Puebla, R.; Liz-Marzan, L. M.; Javier Garcia de Abajo, F. *J. Phys. Chem. Lett.*, **2010**, 1, 2428.

(241) Scaiano, J. C.; Stamplecoskie, K. *J. Phys. Chem. Lett.*, **2013**, 4, 1177.

(242) Nabika, H.; Takase, M.; Nagasawa, F.; Murakoshi, K. *J. Phys. Chem. Lett.*, **2010**, 1, 2470.

(243) Strating, J.; Zwanenbu.B; Wagenaar, A.; Udding, A. C. *Tetrahedron Lett.*, **1969**, 125.

(244) Suzuki, M.; Aotake, T.; Yamaguchi, Y.; Noguchi, N.; Nakano, H.; Nakayama, K.-i.; Yamada, H. *J. Photochem. Photobiol. C: Photochem. Rev.*, **2014**, 18, 50.

(245) Tönshoff, C.; Bettinger, H. F. *Angew. Chem. Int. Ed.*, **2010**, 49, 4125.

(246) Wright, M. W.; Welker, M. E. *J. Org. Chem.*, **1996**, 61, 133.

(247) Lakowicz, J. R.; Shen, Y. B.; D'Auria, S.; Malicka, J.; Fang, J. Y.; Gryczynski, Z.; Gryczynski, I. *Anal. Biochem.*, **2002**, 301, 261.

(248) Hu, J.; Liu, S. *Macromolecules*, **2010**, 43, 8315.

(249) Apex2 Version 2.2-0 and SAINT+ Version 7.46A; Bruker Analytical X-ray System, Inc.

Madison, Wisconsin, USA, 2007.

(250) Connors, K. A. *Chemical Kinetics*; Wiley: New York, 1990.

(251) Sharma, A.; Schulman, S. G. *Introduction to Fluorescence Spectroscopy*; Wiley: New York, 1999.

(252) Swaminathan, S.; Garcia-Amoros, J.; Fraix, A.; Kandoth, N.; Sortino, S.; Raymo, F. M. *Chem. Soc. Rev.*, **2014**, 43, 4167.

(253) Hu, Y.; Kramer, M. C.; Boudreaux, C. J.; McCormick, C. L. *Macromolecules*, **1995**, 28, 7100.

(254) Chen, H.; Kim, S.; He, W.; Wang, H.; Low, P. S.; Park, K.; Cheng, J.-X. *Langmuir*, **2008**, 24, 5213.

(255) Chen, H.; Kim, S.; Li, L.; Wang, S.; Park, K.; Cheng, J.-X. *Proc. Natl. Acad. Sci. U.S.A.*, **2008**, 105, 6596.

(256) Njikang, G. N.; Gauthier, M.; Li, J. *Polymer*, **2008**, 49, 5474.

(257) Jiwpanich, S.; Ryu, J.-H.; Bickerton, S.; Thayumanavan, S. *J. Am. Chem. Soc.*, **2010**, 132, 10683.

(258) Ryu, J.-H.; Chacko, R. T.; Jiwpanich, S.; Bickerton, S.; Babu, R. P.; Thayumanavan, S. *J. Am. Chem. Soc.*, **2010**, 132, 17227.

(259) Chen, K.-J.; Chiu, Y.-L.; Chen, Y.-M.; Ho, Y.-C.; Sung, H.-W. *Biomaterials*, **2011**, 32, 2586.

(260) Lu, J.; Owen, S. C.; Shoichet, M. S. *Macromolecules*, **2011**, 44, 6002.

(261) Hu, P.; Tirelli, N. *React. Funct. Polym.*, **2011**, 71, 303.

(262) McDonald, T. O.; Martin, P.; Patterson, J. P.; Smith, D.; Giardiello, M.; Marcello, M.; See, V.; O'Reilly, R. K.; Owen, A.; Rannard, S. *Adv. Funct. Mater.*, **2012**, 22, 2469.

(263) Li, Y.; Budamagunta, M. S.; Luo, J.; Xiao, W.; Voss, J. C.; Lam, K. S. *Acs Nano*, **2012**, 6, 9485.

(264) Li, Y.; Xiao, W.; Xiao, K.; Berti, L.; Luo, J.; Tseng, H. P.; Fung, G.; Lam, K. S. *Angewandte Chemie-International Edition*, **2012**, 51, 2864.

(265) Bickerton, S.; Jiwpanich, S.; Thayumanavan, S. *Mol. Pharm.*, **2012**, 9, 3569.

(266) Javali, N. M.; Raj, A.; Saraf, P.; Li, X.; Jasti, B. *Pharm. Res.*, **2012**, 29, 3347.

(267) Klymchenko, A. S.; Roger, E.; Anton, N.; Anton, H.; Shulov, I.; Vermot, J.; Mely, Y.; Vandamme, T. F. *Rsc Advances*, **2012**, 2, 11876.

(268) Lee, S.-Y.; Tyler, J. Y.; Kim, S.; Park, K.; Cheng, J.-X. *Mol. Pharm.*, **2013**, 10, 3497.

(269) Nakatsuji, S.; Matsuda, K.; Uesugi, Y.; Nakashima, K.; Akiyama, S.; Fabian, W. *Journal of the Chemical Society-Perkin Transactions 1*, **1992**, 755.

(270) Gabe, Y.; Urano, Y.; Kikuchi, K.; Kojima, H.; Nagano, T. *J. Am. Chem. Soc.*, **2004**, 126, 3357.

(271) Grazon, C.; Rieger, J.; Meallet-Renault, R.; Clavier, G.; Charleux, B. *Macromol. Rapid Commun.*, **2011**, 32, 699.

(272) Peng, H.-Q.; Xu, J.-F.; Chen, Y.-Z.; Wu, L.-Z.; Tung, C.-H.; Yang, Q.-Z. *Chem. Commun.*, **2014**, 50, 1334.

(273) García-Moreno, I.; Zhang, D.; Costela, Á.; Martín, V.; Sastre, R.; Xiao, Y. *J. Appl. Phys.*, **2010**, 107, 073105.

(274) Sandler, S. R.; Karo, W.; Bonesteel, J.-A.; Pearce, E. M. *Polymer Synthesis and Characterization:Dilute solution viscosity of polymers*; Academic Press: San Diego, 1998.

(275) In *Advanced Optical Flow Cytometry: Methods and Disease Diagnoses*; Tuchin, V. V., Ed.; Wiley-VCH: Weinheim, 2011.

(276) Pawley, J. B. (Ed.) *Handbook of Biological Confocal Microscopy*; Springer: New York, 2006.

(277) Johnson, I.; I.; Spence, M. T. Z. (Eds.) *Molecular Probes Handbook: A Guide to Fluorescent Probes and Labeling Technologies*; Grand Island, 2011.

(278) Schaafsma, B. E.; Mieog, J. S. D.; Hutteman, M.; van der Vorst, J. R.; Kuppen, P. J. K.; Löwik, C. W. G. M.; Frangioni, J. V.; van de Velde, C. J. H.; Vahrmeijer, A. L. *J Surg Oncol*, **2011**, 104, 323.

(279) Yan, J.; Estévez, M. C.; Smith, J. E.; Wang, K.; He, X.; Wang, L.; Tan, W. *Nano Today*, **2007**, 2, 44.

(280) Gonçalves, M. S. T. *Chem. Rev.*, **2009**, 109, 190.

(281) Kim, J.; Piao, Y.; Hyeon, T. *Chem. Soc. Rev.*, **2009**, 38, 372.

(282) Sinkeldam, R. W.; Greco, N. J.; Tor, Y. *Chem. Rev.*, **2010**, 110, 2579.

(283) Louie, A. *Chem. Rev.*, **2010**, 110, 3146.

(284) Bonacchi, S.; Genovese, D.; Juris, R.; Montalti, M.; Prodi, L.; Rampazzo, E.; Zaccheroni, N. *Angew. Chem. Int. Ed.*, **2011**, 50, 4056.

(285) Chinen, A. B.; Guan, C. M.; Ferrer, J. R.; Barnaby, S. N.; Merkel, T. J.; Mirkin, C. A. *Chem. Rev.*, **2015**, 115, 10530.

(286) Elsabahy, M.; Heo, G. S.; Lim, S.-M.; Sun, G.; Wooley, K. L. *Chem. Rev.*, **2015**, 115, 10967.

(287) Jiang, S.; Gnanasammandhan, M. K.; Zhang, Y. *J R Soc Interface*, **2010**, 7, 3.

(288) He, X.; Wang, K.; Cheng, Z. *Wiley Interdiscip Rev Nanomed Nanobiotechnol*, **2010**, 2, 349.

(289) Altınoğlu, E. İ.; Adair, J. H. *Wiley Interdiscip Rev Nanomed Nanobiotechnol*, **2010**, 2, 461.

(290) Luo, S.; Zhang, E.; Su, Y.; Cheng, T.; Shi, C. *Biomaterials*, **2011**, 32, 7127.

(291) Yi, X.; Wang, F.; Qin, W.; Yang, X.; Yuan, J. *Int J Nanomedicine*, **2014**, 9, 1347.

(292) Jin, Y.; Ye, F.; Zeigler, M.; Wu, C.; Chiu, D. T. *ACS Nano*, **2011**, 5, 1468.

(293) Wagh, A.; Qian, S. Y.; Law, B. *Bioconjugate Chem.*, **2012**, 23, 981.

(294) Grazon, C.; Rieger, J.; Méallet-Renault, R.; Charleux, B.; Clavier, G. *Macromolecules*, **2013**, 46, 5167.

(295) Petriella, M.; Deniz, E.; Swaminathan, S.; Roberti, M. J.; Raymo, F. M.; Bossi, M. L. *Photochem. Photobiol.*, **2013**, 89, 1391.

(296) Swaminathan, S.; Fowley, C.; Thapaliya, E. R.; McCaughan, B.; Tang, S.; Fraix, A.; Captain, B.; Sortino, S.; Callan, J. F.; Raymo, F. M. *Nanoscale*, **2015**, 7, 14071.

(297) Balter, M.; Li, S.; Morimoto, M.; Tang, S.; Hernando, J.; Guirado, G.; Irie, M.; Raymo, F. M.; Andreasson, J. *Chemical Science*, **2016**, 7, 5867.

(298) Ragab, S. S.; Thapaliya, E. R.; Zhang, Y.; Tang, S.; McMahan, J. B.; Syed, S.; Captain, B.; Raymo, F. M. *RSC Advances*, **2016**, 6, 32441.

(299) Zhang, Y.; Tang, S.; Sansalone, L.; Baker, J. D.; Raymo, F. M. *Chemistry – A European Journal*, **2016**, 22, 15027.

(300) Johnson, I. *The Molecular Probes Handbook: A Guide to Fluorescent Probes and Labeling Technologies, 11th Edition*; Life Technologies Corporation, 2010.

(301) Tomasulo, M.; Deniz, E.; Alvarado, R. J.; Raymo, F. M. *J. Phys. Chem. C*, **2008**, 112, 8038.

(302) Würth, C.; Grabolle, M.; Pauli, J.; Spieles, M.; Resch-Genger, U. *Nat. Protocols*, **2013**, 8, 1535.

(303) Edwards, S. L.; Charlie, N. K.; Milfort, M. C.; Brown, B. S.; Gravlin, C. N.; Knecht, J. E.; Miller, K. G. *PLoS Biology*, **2008**, 6, 1715.

(304) Mello, C. C.; Kramer, J. M.; Stinchcomb, D.; Ambros, V. *The EMBO Journal*, **1991**, 10, 3959.

(305) Collins, K. M.; Koelle, M. R. *The Journal of neuroscience : the official journal of the Society for Neuroscience*, **2013**, 33, 761.

(306) Ishikawa-Ankerhold, H. C.; Ankerhold, R.; Drummen, G. P. C. *Molecules*, **2012**, 17, 4047.

(307) Kocher, C.; Montali, A.; Smith, P.; Weder, C. *Adv. Funct. Mater.*, **2001**, 11, 31.

(308) Ohshita, J.; Uemura, T.; Kim, D.-H.; Kunai, A.; Kunugi, Y.; Kakimoto, M. *Macromolecules*, **2005**, 38, 730.

(309) Lee, J. K.; Kim, H.-J.; Kim, T. H.; Lee, C.-H.; Park, W. H.; Kim, J.; Lee, T. S. *Macromolecules*, **2005**, 38, 9427.

(310) Kwak, G.; Fujiki, M.; Sakaguchi, T.; Masuda, T. *Macromolecules*, **2006**, 39, 319.

(311) Gao, L.; Lu, N.; Hao, J.; Hu, W.; Shi, G.; Wang, Y.; Chi, L. *Langmuir*, **2009**, 25, 3894.

(312) Belfield, K. D.; Schafer, K. J. *Chem. Mater.*, **2002**, 14, 3656.

(313) Pistolis, G.; Boyatzis, S.; Chatzichristidi, M.; Argitis, P. *Chem. Mater.*, **2002**, 14, 790.

(314) Vasilopoulou, M.; Georgiadou, D.; Pistolis, G.; Argitis, P. *Adv. Funct. Mater.*, **2007**, 17, 3477.

(315) Lam, J. W. Y.; Tang, B. Z. *Acc. Chem. Res.*, **2005**, 38, 745.

(316) Park, S.; Kim, S.; Seo, J.; Park, S. Y. *Macromolecules*, **2005**, 38, 4557.

(317) Tomasulo, M.; Raymo, F. M. *J. Mater. Chem.*, **2005**, 15, 4354.

(318) Deniz, E.; Tomasulo, M.; DeFazio, R. A.; Watson, B. D.; Raymo, F. M. *PCCP*, **2010**, 12, 11630.

(319) Garcia-Amoros, J.; Swaminathan, S.; Zhang, Y.; Nonell, S.; Raymo, F. M. *PCCP*, **2015**, 17, 11140.

(320) Zhang, Y.; Garcia-Amoros, J.; Captain, B.; Raymo, F. M. *J. Mater. Chem. C*, **2016**, 4, 2744.

(321) Chae, K. H.; Kim, Y. H. *Adv. Funct. Mater.*, **2007**, 17, 3470.

(322) McCormick, A. M.; Maddipatla, M. V. S. N.; Shi, S.; Chamsaz, E. A.; Yokoyama, H.; Joy, A.; Leipzig, N. D. *ACS Appl. Mater. Interfaces*, **2014**, 6, 19655.

(323) Pennakalathil, J.; Kim, T.-H.; Kim, K.; Woo, K.; Park, J.-K.; Hong, J.-D. *Langmuir*, **2010**, 26, 11349.

(324) Sandler, S. R.; Karo, W.; J. Bonesteel, W.; Pearce, E. M. *Polymer Synthesis and Characterization: A laboratory Manual*; Academic Press, San Diego, 1998.